Max-Planck-Institut
für Meteorologie

MAX-PLANCK-GESELLSCHAFT

International Max Planck Research School
on Earth System Modelling

Analysis of the Surface Layer and the Entrainment Zone of a Convective Boundary Layer using Direct Numerical Simulation

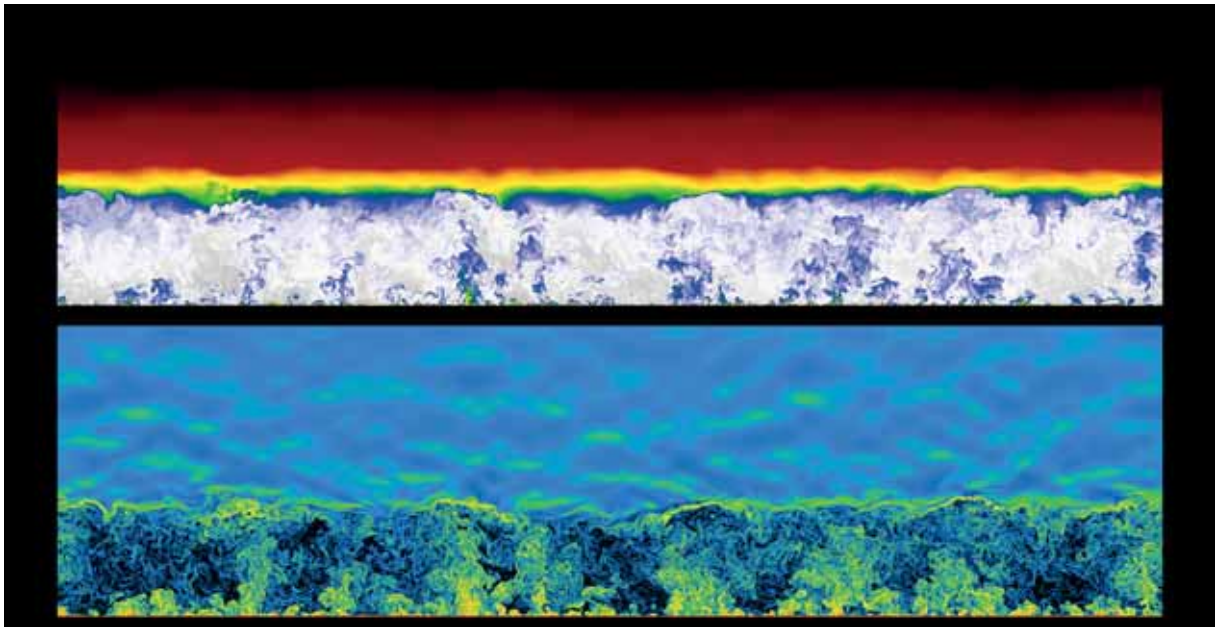

Jade Rachele S. Garcia

Hamburg 2014

Berichte zur Erdsystemforschung
Reports on Earth System Science

159
2014

Hinweis

Die Berichte zur Erdsystemforschung werden vom Max-Planck-Institut für Meteorologie in Hamburg in unregelmäßiger Abfolge herausgegeben.

Sie enthalten wissenschaftliche und technische Beiträge, inklusive Dissertationen.

Die Beiträge geben nicht notwendigerweise die Auffassung des Instituts wieder.

Die "Berichte zur Erdsystemforschung" führen die vorherigen Reihen "Reports" und "Examensarbeiten" weiter.

Notice

The Reports on Earth System Science are published by the Max Planck Institute for Meteorology in Hamburg. They appear in irregular intervals.

They contain scientific and technical contributions, including Ph. D. theses.

The Reports do not necessarily reflect the opinion of the Institute.

The "Reports on Earth System Science" continue the former "Reports" and "Examensarbeiten" of the Max Planck Institute.

Anschrift / Address

Max-Planck-Institut für Meteorologie
Bundesstrasse 53
20146 Hamburg
Deutschland

Tel./Phone: +49 (0)40 4 11 73 - 0
Fax: +49 (0)40 4 11 73 - 298

name.surname@mpimet.mpg.de
www.mpimet.mpg.de

Layout

Bettina Diallo and Norbert P. Noreiks
Communication

Copyright

Max-Planck-Institut
für Meteorologie

MAX-PLANCK-GESELLSCHAFT

International Max Planck Research School
on Earth System Modelling

Analysis of the Surface Layer and the Entrainment Zone of a Convective Boundary Layer using Direct Numerical Simulation

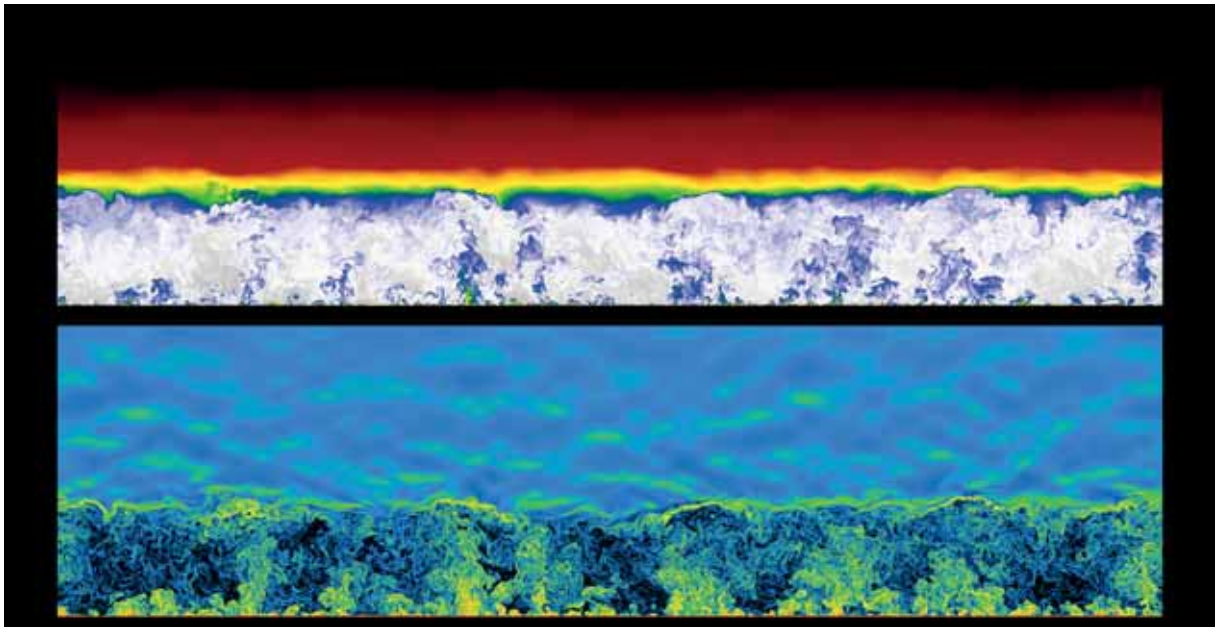

Jade Rachele S. Garcia

Hamburg 2014

Berichte zur Erdsystemforschung
Reports on Earth System Science

159
2014

Jade Rachele S. Garcia
von den Philippinen

Max-Planck-Institut für Meteorologie
Bundesstrasse 53
20146 Hamburg

Als Dissertation angenommen
vom Fachbereich Geowissenschaften der Universität Hamburg

auf Grund der Gutachten von
Dr. Juan Pedro Mellado
und
Prof. Dr. Bjorn Stevens

Hamburg, den 27. Juni 2014
Professor Dr. Christian Betzler
Leiter des Departments Geowissenschaften

ISSN 1614-1199

Summary

Small-scale turbulence in the surface layer and the entrainment zone (EZ) of a convective boundary layer (CBL) significantly affect the fluxes between the surface and the free troposphere. Due to limitations in the resolution of large scale models and even large-eddy simulations, small-scale turbulence is mostly unresolved and therefore need to be modeled. Current models are still significantly inaccurate due to the lack of understanding of these small-scale processes. To gain some understanding of them, we use direct numerical simulation, which resolves turbulence accurately. We address some open questions concerning turbulence in the surface layer and the entrainment zone.

Regarding the surface layer, we ask:

- Do statistics at the surface layer for flows in pure free convection obey classical similarity scaling?
- Does stratification, and therefore the outer scale, affect the surface layer statistics? If so, how?

Regarding the entrainment zone, we ask:

- Does stratification impose a characteristic length scale different from the CBL thickness?
- Does the EZ vertical structure affect the functional relationship between the mean entrainment rate $E = (1/w_*)dz_i/dt$ and a convective Richardson number?

A consequence of this study is the establishment of the usefulness of direct numerical simulation as a tool in atmospheric boundary layer turbulence research.

Contents

1 Introduction

1.1 The atmospheric boundary layer

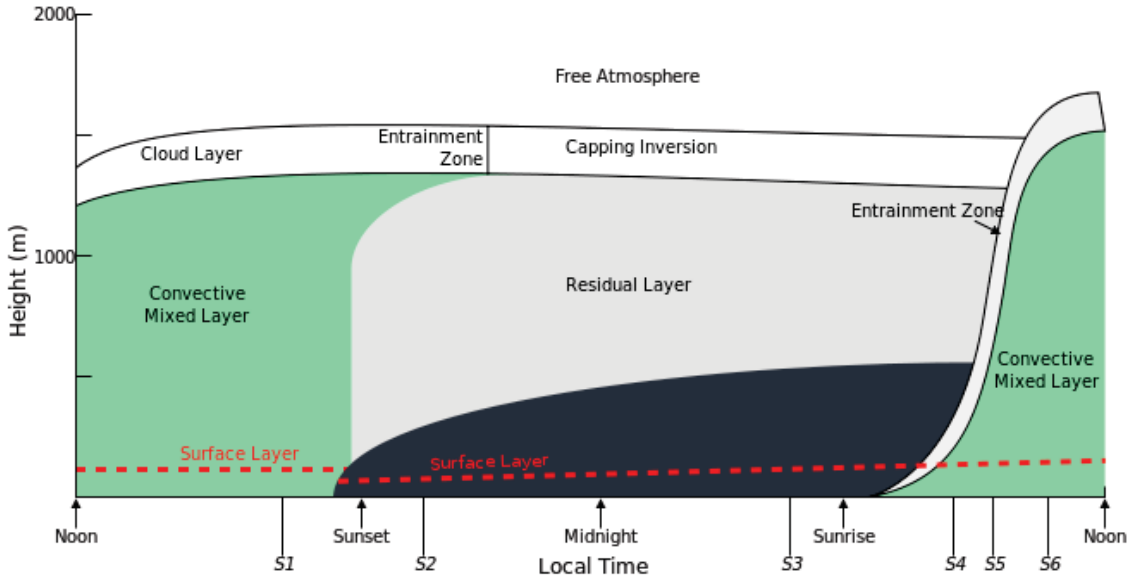

Figure 1.1: Sketch of the diurnal cycle of the atmospheric boundary layer over land featuring the daytime convective boundary layer and the nocturnal stable boundary layer. Source: Wikipedia Images

The atmospheric boundary layer (ABL) is the region of the lower troposphere (around a few kilometers) that is in direct contact with the Earth's surface. Because of this direct contact, flows in the ABL are characterized by turbulence, which is induced by convective motions due to surface heating by solar radiation, and by shear effects due to the drag felt by the wind as the wind velocity is bound to be zero at the surface. The type of turbulence forcing in the ABL depends on the diurnal cycle, particularly over land: convective motions that destabilize the ABL may dominantly drive turbulence during daytime while mean shear effects mainly drive turbulence during nighttime as the surface radiatively cools and stabilizes the ABL (see Fig. 1.1 for a sketch).

Above the atmospheric boundary layer is the rest of the troposphere, called the

free troposphere, which is relatively nonturbulent and usually stably stratified. Turbulence promotes the advancement of the ABL into the free troposphere through entrainment of air from the free troposphere into the turbulent boundary layer. The ABL's advancement is, however, hampered by stable buoyancy forces within the overlying free troposphere. Due to this interaction, a stable capping layer forms in between the turbulent layer and the relatively nonturbulent free troposphere.

Consequently, the pollutants that we emit into the atmosphere are transported by the turbulent motions but are usually trapped within the ABL because of the capping effect of the overlying stable region. Aside from pollutants, other quantities such as air constituents (water vapor, oxygen, aerosols, greenhouse gases), momentum (friction or drag), and energy are transported from the surface into the free troposphere, which consequently affect air quality, atmospheric chemistry, and boundary layer clouds (that are crucial for the global climate problem!).

Within the big picture of the Earth as a system, the atmospheric boundary layer acts as the thin buffer layer that couples the Earth's surface and the rest of the troposphere and regulates the fluxes of different quantities between these two regions. An adequate representation of the ABL is therefore crucial in general circulation models (GCMs), numerical weather prediction models, and pollution dispersion studies. Properly representing the ABL then requires an understanding of the atmospheric boundary layer and the processes affecting its growth.

The convective boundary layer

The dynamics and the structure of the convective daytime– and the stable nocturnal boundary layer are quite different and both deserve to be studied comprehensively. In this study, we only focus on the daytime boundary layer or the convective boundary layer (CBL), particularly when the mean wind is relatively weak (usually during fair weather days), and refer to Stull (1988) for a description of the nighttime boundary layer.

The convective boundary layer is usually depicted as being composed of different regions, which are sketched in Fig. 1.2:

- the unstable surface layer, which is typically 100-meters thick or 10%-20% of the CBL thickness, wherein properties vary rapidly with distance from the surface, and the vertical profiles of fluxes and shear stress are approximately

constant

- the well-mixed layer, where the convective mixing due to rising buoyant thermals and accompanying downdrafts cause conserved quantities (such as potential temperature and humidity) to be relatively constant with respect to altitude
- the entrainment zone, the relatively thin boundary between the CBL and the free troposphere, a region of increased stability that caps the CBL

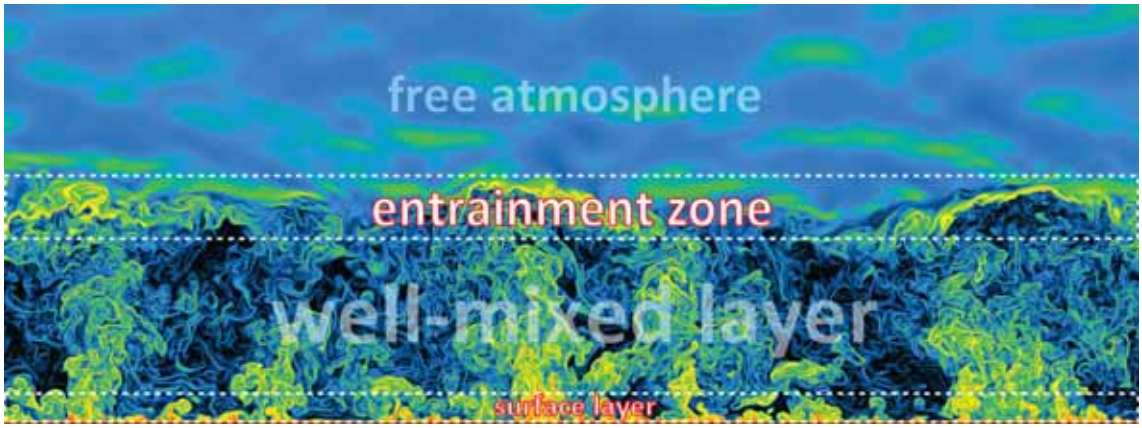

Figure 1.2: Visualization of the convective boundary layer featuring the different regions.

As depicted in Fig. 1.2, the elements of convective motions are in the form of rising buoyant plumes attached to the surface and rising thermals that are already detached from the surface. The turbulent thermals tend to overshoot their level of neutral buoyancy due to inertia and consequently penetrate into the stable region. This overshooting is called penetrative convection (see Deardorff et al., 1969). The thermals are then deflected by the opposing stable buoyancy force. As the thermals are deflected, they tend to displace down wisps or sheets of more buoyant air from the free troposphere into the mixed layer, wherein the nonturbulent fluid parcels are entrained and mixed rapidly by the turbulent motions (see Chapter 5). Accordingly, CBL growth is regulated by the interaction between turbulence and stable stratification that occurs at the entrainment zone.

1.2 Review of related literature

Due to the importance of understanding the properties of the CBL, extensive research has been done on it within the past five decades, involving laboratory exper-

iments, field observations, and numerical simulations.

Earlier experiments regarding thermal convection in air (Deardorff and Willis, 1967) and penetrative convection in a water tank (Deardorff et al., 1969) have paved the way for the pioneering works of Deardorff and Willis (Willis and Deardorff, 1974; Deardorff, 1970; Deardorff et al., 1980; Deardorff and Willis, 1985) wherein a convective boundary layer is mimicked in a water tank to investigate the vertical structure of the CBL.

Findings in the laboratory regarding the vertical structure of the CBL were further confirmed by Kansas and Minnesota field experiments (see Kaimal and Wyngaard, 1990, for an overview). These field campaigns justified the use of the boundary-layer depth as the scaling length of the mixed layer (Kaimal et al., 1976) and reaffirmed the findings of Willis and Deardorff (1974) that the convective scalings proposed by (Deardorff, 1970) indeed characterized the variances of quantities within the mixed layer. The Minnesota data (Kaimal et al., 1976) also showed evidence of entrainment of free troposphere air into the mixed layer.

Numerical simulations, in particular the large-eddy simulations (LES) pioneered by Deardorff (1972), were considerably successful in simulating a CBL with comparable vertical structure, owing to the fact that the CBL is dominated by large eddies within the well-mixed layer (Mason, 1994). Schmidt and Schumann (1989) further studied the coherent structure of the CBL, which was made feasible by the availability of entire velocity and temperature fields for certain points of time, a clear advantage of numerical simulations over the other two aforementioned approaches.

Altogether, these studies have successfully established the general vertical structure and the behavior of relevant low-order statistics of the potential temperature and velocity fields within the well-mixed layer (Stull, 1988; Garratt, 1992; Zilitinkevich, 1991). In particular, the simplest canonical case, the dry, shear-free CBL growing into a linearly stratified free troposphere, is considered to be a solved problem in the sense that the growth rate of the CBL and the mean buoyancy behave proportional to the encroachment scales (Carson, 1973) (see Chapter 3, section 3.2), and the root-mean-square (r.m.s.) of fluctuations of buoyancy and velocity at the mixed layer behave proportional to the convective scales (Deardorff, 1970) (see Chapter 3, section 3.3). The robust vertical structure of the low-order statistics have motivated the development of bulk layer frameworks, like the zero-order and first-order models, which have been observed to work satisfactorily, at least for the simplest case of a dry, shear-free CBL (Zilitinkevich, 1991; Fedorovich et al., 2004b). Thus knowledge

of the mixed layer in general is quite complete and models related to this simplest case are well developed. However, some details of the small-scale processes at the surface layer and the entrainment zone still remain obscure.

1.3 Open questions

Regarding the surface layer, there is still uncertainty in the flux-gradient relations in the limit of free convection (Beljaars, 1994; Grachev et al., 2000; Wilson, 2001) and uncertainty on how the outer scales affect the surface layer (Businger, 1973; Panofsky et al., 1977; McNaughton, 2004; Mellado, 2012) [addressed in Chapter 4].

Questions on the surface layer:

- Do statistics at the surface layer for flows in pure free convection obey classical similarity scaling?
- Does stratification, and therefore the outer scale, affect the surface layer statistics? If so, how?

Regarding the entrainment zone, the lack of understanding on how stratification affects the characteristic length scale of turbulence in the entrainment zone reflects on the large sensitivity of local properties to the particular length scale used for subgrid-scale parameterization (Deardorff, 1980b; Stevens et al., 2000a; Sullivan and Patton, 2011), while lack of understanding on the effect of the entrainment zone's vertical structure on the entrainment-rate parameters reflects on inconsistency and disagreement in the entrainment-rate parameterizations that have been proposed (Tennekes and Driedonks, 1981; Fedorovich et al., 2004b) [addressed in Chapter 5].

Questions on the entrainment zone:

- Does stratification impose a characteristic length scale different from the CBL thickness?
- Does the EZ vertical structure affect the functional relationship between

the mean entrainment rate $E = (1/w_*)dz_i/dt$ and a convective Richardson number?

One may argue that for the simple case of a dry, shear-free CBL with a constant surface buoyancy flux, the details of the surface layer and the entrainment zone are unimportant as long as the model used sufficiently describes the mean buoyancy flux at the surface, which constitutes the energy input into the system. Indeed, large-eddy simulations give an accurate representation of the bulk properties and large-scale dynamics of the system, even if the surface layer is not accurately represented (Fedorovich et al., 2004b; Sullivan and Patton, 2011), while a zero-order bulk model predicts the entrainment rate well for this simple case, even if the zero-order bulk model represents the entrainment zone as infinitesimally thin (Driedonks, 1982; Fedorovich and Mironov, 1995; Fedorovich et al., 2004b). However, when other processes or complexities are added to the system – for instance, horizontal wind, heterogeneity in the surface properties, and clouds – the details of the surface layer model and the vertical structure of the entrainment zone become relevant.

Attempts to clarify these uncertainties have therefore been performed using the same methods that established our knowledge of the mixed layer. However inherent infirmities in these approaches render these studies inconclusive. For example, field observations would ideally be useful for a deeper understanding of the surface layer and the entrainment zone and for the development of more realistic ABL models since they represent reality. However, atmospheric observations are simply not suitable for addressing the question of whether free convection scaling in the surface layer applies in the limit of free convection because of the lack of control on such environments and the unavoidable presence of wind, no matter how weak. For studying the entrainment zone, the currently achievable resolution and accuracy in remote sensing techniques such as lidar and radar systems enable the measurement of profiles of turbulent variables within the lower troposphere (Hogan et al., 2009) and the visual identification of the entrainment zone and different entrainment mechanisms (Träumner et al., 2011). However, a more fundamental understanding of how these mechanisms are affected by flow parameters is difficult to derive from atmospheric observations not only because measurements of entrainment events and entrainment zone thickness are difficult to obtain within the needed accuracy (Wulfmeyer et al., 2010) but also because these measurements include the effect of different complex processes, such as shear, that further complicate the entrainment mecha-

nism (Grabon et al., 2009). Due to these complexities, there is always significant scatter in the data, particularly in attempts to find a functional relation between the entrainment rate and a Richardson number, and between the entrainment zone thickness and a Richardson number (Träumner et al., 2011).

Controlled counterparts of the CBL in the laboratory have therefore been developed to study free convection and the canonical flow of turbulent mixing across a stratified density interface. Studies on free convection were usually set up as Rayleigh-Benárd convection. However, many of these studies do not focus on questions regarding the scalings of surface layer profiles. Besides, data in the surface layer are quite limited due to the difficulty of obtaining accurate measurements inside the relatively thin region, which require simultaneous access to several quantities at several positions. Adding stratification to the flow even increases the difficulty in achieving a thick enough surface layer in the lab since stratification makes a large scale separation between the inner and outer scales more difficult to achieve. As for the entrainment zone, laboratory studies addressed the entrainment zone length scale question by using parcel theory to predict the penetration depth of thermals (Zeman and Tennekes, 1977; Deardorff, 1979; Hopfinger, 1987) and the entrainment-rate parameterization question by finding power laws with respect to a Richardson number [Rouse and Dodu (1955); Linden (1973); Deardorff (1979); Tennekes and Driedonks (1981); Turner (1986), see Fernando (1991) for a review of early papers]. However, a consensus regarding both questions still has not been reached. Part of the difficulty in analyzing the details of the surface layer and the entrainment zone is due to the high accuracy needed in data sampling, which then requires great ingenuity and care. Laboratory experiments are also often criticized regarding their scalability to the atmospheric flows because of the relatively low Reynolds numbers that are achievable and because of the particular turbulent forcing used (e.g. oscillating grid, imposed density difference by using salt) for mimicking atmospheric turbulence. In tank experiments, possible side-effects, such as secondary circulations, may also be induced by the tank's boundaries. Moreover, the use of water instead of air in tank experiments may lead to Prandtl number effects being significant (Jonker and Jimnez, 2014), while in wind tunnels, stratifying the air is difficult.

Due to aforementioned difficulties in field observation and laboratory experiments, most of the studies that addressed the aforementioned issues were based on data from large-eddy simulations. However, as explained by Sullivan et al. (1998) and Fedorovich et al. (2004b), LES were at that time not highly resolved and are still unavoidably tainted by uncertainty due to subgrid-scale (SGS) models. This uncer-

tainty manifests itself as sensitivity of statistics at the surface layer and the entrainment zone to parameterizations. The sensitivity of statistics is even compounded when complexity is added to the problem, a clear example of which is the CBL with mean wind. The addition of shear has been observed to increase the contribution of the small scales to the turbulence kinetic energy, consequently, SGS fluxes in LES increase at the entrainment zone (Pino et al., 2003). Although there is finally consensus that mean shear increases the entrainment flux (Pino and Vil-Guerau De Arellano, 2008), how much it increases is still a bone of contention (Fedorovich et al., 2004a) and a strong indication of the result's sensitivity to SGS models. Sensitivity of entrainment to the SGS model can be further observed in LES intercomparison studies for different cases: clear ABL (Driedonks, 1982), smoke-cloud, (Bretherton et al., 1999; Stevens et al., 1999), stratocumulus-topped boundary layers (Stevens, 2002; Stevens et al., 2005; Wood, 2012), and CBLs with heterogeneous surface (Huang et al., 2007).

In this respect, resolving more of the small scales should be able to address the above-mentioned issue since the Navier-Stokes equations is theoretically the limit of the filtered equations as the filter size goes to zero (Stevens and Lenschow, 2001). To find out whether LES converges with grid refinement, Sullivan and Patton (2011) varies the grid mesh from 32^3 to 1024^3. Their result shows that for a 512^3 grid and up, the vertical profiles of low-order statistics are already converging in the well-mixed region when the ratio $z_i/(C_s\Delta f) > 310$, where z_i is the CBL thickness, C_s is the Smagorinsky constant and Δf is the filter size. This should be unsurprising since the well-mixed region is dominated by the large scales, therefore SGS models should play a relatively smaller role. In contrast, the results in Sullivan and Patton (2011) clearly show lack of convergence for some statistics at the surface layer and at the entrainment zone (like the temperature variance) where the effective Reynolds number is much smaller than that of the mixed layer. In these regions, the SGS model represents turbulence poorly, as confirmed by their attribution of non-convergence of the temperature variance to the use of a prescribed SGS closure based on an eddy viscosity and a turbulent Prandtl number. They claim that having a fuller set of prognostic equations for subgrid-scale temperature variance (e.g. Wyngaard (2004); Hatlee and Wyngaard (2007)) can potentially improve convergence.

Clearly the price for being able to theoretically consider large Reynolds numbers is the uncertainty introduced by the subgrid-scale model. We say here theoretically because it is also unclear whether LES results are indeed characteristic of high Reynolds number flows due to unavoidable low Reynolds number effects inherent in

limited grid resolution and the associated numerical artifacts, like numerical diffusion. The lack of convergence at the surface layer and the entrainment zone could be an indication of low Reynolds number effects since the effect of grid refinement is to increase the effective Reynolds number by resolving more of the small-scale eddies. Moreover, the obscured extent at which SGS models are able to represent small-scale turbulence is, of course, detrimental to the physical understanding of the dynamics of the flow at the surface layer and the entrainment zone. Although one can put efforts on improving the SGS model, this effort is not much less than that required to solve the Navier-Stokes equations directly.

1.4 Our approach: Direct numerical simulations

Based on the considerations presented in the previous section, we propose to use direct numerical simulations (discussed in Chapter 2 section 2.3) as an alternative approach for investigating the surface layer and the entrainment zone of the CBL, since DNS resolves turbulence down to the smallest dissipative scales, and is therefore free from uncertainty introduced by turbulence models. The approach itself is not new, since direct numerical simulations of the atmospheric boundary layer have already been performed within the past two decades (Coleman et al., 1994; Coleman, 1999). However, the use of DNS in the field of atmospheric boundary layer research is usually received with skepticism since resolving down to the dissipative scale means that the achievable Reynolds numbers are restricted to low/moderate values due to limited computing power, and that simulating turbulent flows with atmospheric Reynolds numbers of $O(10^8)$ is virtually impossible nowadays. Further taking into account the high computational cost, DNS as a general purpose tool in simulating atmospheric boundary layer flows seems to be out of the question.

The implicit assumption backing such skepticism is that for DNS to be useful in atmospheric turbulence research, DNS should be executed at atmospheric Reynolds numbers. However, as emphasized by Moin and Mahesh (1998), there are two questions that are not very often raised: "How high a Reynolds number is high enough?" and "What are the objectives of the computations?".

The first question is worth asking because of Reynolds number similarity: the principle, based on observation, that statistics related to the large scales become independent of the Reynolds number once this is large enough (Tennekes and Lumley, 1972; Dimotakis, 2000; Monin and Yaglom, 2007) [see Chapter 2 section 2.2 for an

expounded discussion]. The early DNS of ABL flows, such as that of Coleman et al. (1994); Coleman (1999), was motivated and justified by Reynolds number similarity. Quoting from Coleman (1999), "the issue of relevance of a numerical study of the PBL does not hinge on the finescales (which after all are not present in LES either), but on faithfully representing the physics of the scales that *are* resolved and in doing so such that they are characteristic of high Re atmospheric turbulence." We justify our approach with the same argument. The key difference of our study is that current technology makes this justification more plausible.

Regarding the second question, the particular objective of the computation is to have a full characterization of the simplest canonical CBL (dry, shear-free, constant surface buoyancy flux, linearly stratified free troposphere) (see Chapter 2 for the problem description) such that the surface layer and the entrainment zone can be studied in detail. The simplest case can be very useful as a reference and a limiting case to compare with for understanding the more complex CBL. But such a characterization needs to be free from uncertainties caused by turbulence models. For such a goal, using DNS indeed makes the most sense.

In general, the objective of using DNS is neither to totally replace LES, nor to become the general-purpose tool for studying atmospheric turbulence due to high computational costs. For studies interested in statistics associated to the large-scale turbulence, LES works well enough for a fraction of the computational cost that DNS would require. Therefore, instead of replacing LES, the objective is to use DNS to complement the other approaches summarized in the previous section, and complete the modeling/simulation hierarchy DNS $\rightarrow$ LES $\rightarrow$ GCM: small-scale study of the CBL could evaluate LES results that are usually used to evaluate bulk models and GCM boundary layer schemes.

2 Formulation and Methodology

2.1 Problem description

2.1.1 The equations of motion

The equations of fluid motion, in their general form, basically describe the transport of mass, momentum, and energy of a flowing fluid:

$$\begin{aligned} \frac{\partial \rho}{\partial t} + \nabla\cdot(\rho\mathbf{v}) &= 0 \\ \frac{\partial (\rho\mathbf{v})}{\partial t} + \nabla\cdot(\rho\mathbf{v}\otimes\mathbf{v}) &= \nabla\cdot(-p_m\boldsymbol{\delta}+\boldsymbol{\tau}) + \rho\mathbf{f} \\ \frac{\partial [\rho E]}{\partial t} + \nabla\cdot[\rho E\,\mathbf{v}] &= \nabla\cdot[(-p_m\boldsymbol{\delta}+\boldsymbol{\tau})\cdot\mathbf{v}] + \rho\mathbf{f}\cdot\mathbf{v} - \nabla\cdot\mathbf{q} \end{aligned} \tag{2.1}$$

where ρ is the density, $\mathbf{v}$ is the velocity vector with components (v_1, v_2, w) along the directions Ox_1, Ox_2 and Oz, respectively, E is the total energy (kinetic energy plus internal energy), $-p_m\boldsymbol{\delta}$ and $\boldsymbol{\tau}$ are, respectively, the isotropic and deviatoric part of the stress tensor $-p_m\boldsymbol{\delta}+\boldsymbol{\tau}$, where $\boldsymbol{\delta} = [\delta_{ij}]$ is the unitary tensor; $\mathbf{f}$ is a force per unit mass and $\mathbf{q}$ the heat flux vector. The first equation, called the continuity equation, describes how mass is conserved, meaning in a closed system, it cannot be created nor destroyed, thus there are no sources or sinks. The second equation, the Navier-Stokes equation, is Newton's second law applied to fluid motion, which describes how the change in momentum is balanced by the net force acting on the fluid. The third equation is the conservation of total energy, meaning, in a closed system the total energy can neither be created nor destroyed, but can change form.

The equations of motion need to be complemented by the equations of state and the constitutive equations (a model for $\boldsymbol{\tau}$ and $\mathbf{q}$) in order to form a closed system. The resulting closed system of equations, when combined with well-formulated boundary conditions, has been successful in adequately describing fluid motion, even that of turbulent flows, as long as the fluid being studied can be considered as a continuum.

We particularize the general equations of motion to the case of the dry convective

boundary layer. The energy equation is usually written in the form of an evolution equation for thermal energy or enthalpy. Since we are dealing with the dry CBL case, enthalpy is then linearly related to the buoyancy and the third equation is therefore written as a transport equation for the buoyancy $b = g(\rho_0 - \rho)/\rho$, where ρ_0 is the reference density. The following approximations are also made (see Garratt, 1992, for more details)

- the fluid (air) behaves approximately as a Newtonian fluid (viscous stresses are proportional to the strain rate)
- air behaves approximately as an ideal gas (local thermodynamical equilibrium is assumed, thus the equation of state is taken as the ideal gas law)
- the flow is approximately incompressible even though air is a compressible fluid (see Nieuwstadt and Dop, 1984), therefore density changes resulting from pressure changes are negligible
- density changes resulting from temperature changes are important only as they directly affect buoyancy

The last two approximations combined are the Boussinesq approximation. Altogether, these approximations simplify the equations of motion to the following:

$$\begin{aligned} \nabla\cdot\mathbf{v} &= 0 \\ \frac{\partial \mathbf{v}}{\partial t} + \nabla\cdot(\mathbf{v}\otimes\mathbf{v}) &= -\nabla p + \nu\nabla^2\mathbf{v} + b\mathbf{k} \\ \frac{\partial b}{\partial t} + \nabla\cdot(\mathbf{v}b) &= \kappa\nabla^2 b \end{aligned} \tag{2.2}$$

where p is a modified pressure divided by the constant reference density, b is the buoyancy (e.g. which is related to the virtual potential temperature θ_v by a linear relation, $b = g(\theta_v - \theta_{v,0})/\theta_{v,0}$, $\theta_{v,0}$ being the reference value). The parameter ν is the kinematic viscosity, κ is the molecular diffusivity and $\mathbf{k}$ is the unit vector along Oz.

.

2.1.2 Defining properties of turbulent flows

Flows in the atmospheric boundary layer are characterized by turbulence. Although there is no consensus over a strict definition of turbulence (Tsinober, 2009), some established properties of turbulent flows are usually enumerated (Tennekes and Lumley, 1972; Tsinober, 2009):

- Characterized by large Reynolds number - inertia dominates diffusion at the large energy-containing scales
- Contain many degrees of freedom (wide range of scales in space and in time) that are strongly and nonlinearly interacting
- Unpredictable in detail due to chaotic behavior, in spite of the equations of motion's being deterministic, thus a statistical description of the flow is suitable
- Highly dissipative, continuously losing mechanical energy into heat, which means turbulent forcing is required to sustain turbulence, else it decays
- Rotational, therefore characterized by large vorticity fluctuations
- Highly diffusive, therefore transports and mixes quantities more efficiently than molecular diffusion

Due to all of these properties combined, turbulence and an understanding of the equations governing it have remained elusive from the point of view of rigorous mathematical analysis of the Navier-Stokes equations[1]. Tackling the turbulence issue through experiments, both laboratory and numerical, is also difficult due to the complexity of the flow and the difficulty in reproducing the highly turbulent flows found in nature.

2.1.3 The closure problem

Attempts to reduce complexity are usually in the form of some decomposition. Popular decompositions are: mean flow - fluctuating part (introducing Reynolds averaging, as used in Reynolds-averaged Navier Stokes or RANS), resolved - unresolved

[1]One of the Millennium problems is to prove existence and uniqueness of a solution to the Navier-Stokes equations.

(introducing filtering, as used in LES). Such decompositions are known to suffer from the curse of closure, meaning the averaged/filtered equations contain new unknowns and there are more unknowns than equations. Equations derived from the Navier-Stokes equations for these new unknowns further contain other higher-order unknowns, meaning an infinite number of statistical equations are needed to describe turbulence statistically.

To close the problem, one has to come up with a way to relate these extra unknowns to the other known variables of the flow in a manner that represent the dynamic effects of the discarded part of the flow (for the above-mentioned decompositions, this corresponds to the fluctuations from the mean or the scales that were filtered out). These relations are called closure models. Quoting the colorful phrasing of (Tsinober, 2013), a menagerie of closure models employ "dimensional analysis, variety of scaling arguments, symmetries, invariant properties and various assumptions, many of which are of unknown validity and obscured physical and mathematical justification (if any) along with using non-trivial 'surgeries' with removal of large fractions of the flow field". In the following, we present two tools that we use to make the study of turbulent flows slightly more tractable.

2.2 Dimensional analysis and Similarity

A standard tool in fluid dynamics, dimensional analysis is a framework wherein the crucial variables that characterize a system are identified and then organized into a smaller number of dimensionless groups. The reduction of variables and proper choice of groups lead to new classes of similarity – the apparent resemblance in certain qualities of different properties or in the behavior of different phenomena that may differ in the value of the individual variables but have the same values for the proper dimensionless groups. A particular form of similarity that is quite intuitive is geometric similarity, for example two triangles of different sizes are similar if the corresponding sides have lengths in the same ratio.

The concept of similarity is widely exploited in the study of fluid flows since similarity support the use of smaller scale laboratory experiments for studying real-life flows of interest. For two flows to be similar, three types of similarity need to be fulfilled: geometric similarity (same shape, different size), kinematic similarity (ratio of velocities of particles are the same for both flows), and dynamic similarity (ratio of all forces are the same for both flows) (Kline, 1986).

2.2.1 Characteristic scales and dimensionless groups of the CBL

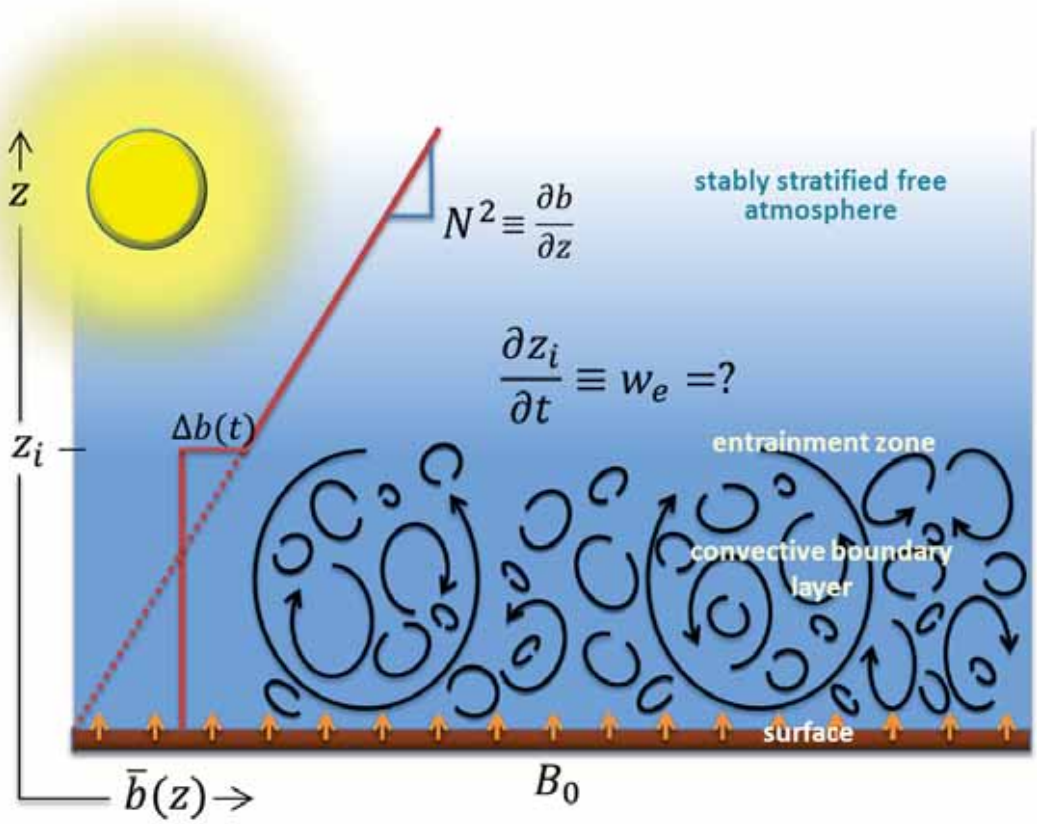

Figure 2.1: Sketch of a canonical CBL with constant and homogeneous buoyancy flux B_0 at the surface, growing against a stably stratified fluid with constant buoyancy frequency $N^2 > 0$.

We apply dimensional analysis to the convective boundary layer sketched in Fig. 2.1 and governed by equations (2.2). We focus on the fully developed turbulent regime that is established after the initial transient, when the initial conditions have been sufficiently forgotten (Tennekes and Lumley, 1972; Monin and Yaglom, 2007) and the parameter space $\{\nu, \kappa, B_0, N\}$ defines the system completely. The absence of an externally imposed characteristic length scale and characteristic velocity is typical of atmospheric buoyancy-driven flows, so we instead use B_0 and N [following Zilitinkevich (1991) and Fedorovich et al. (2004b)] from the above set of parameters to nondimensionalize the problem. The other two parameters are related to molecular effects, which are negligible in the highly turbulent CBL. We construct a reference

time scale N^{-1}, and a reference length scale

$$L_0 = (B_0/N^3)^{1/2} \, . \tag{2.3}$$

The resulting reference velocity scale $(L_0 B_0)^{1/3}$ can be interpreted as the velocity scale associated to a length scale L_0 inside the inertial sub-range that follows from inertial-range Kolmogorov scaling (Pope, 2000), since in the CBL the viscous dissipation rate is observed to be approximately an order-of-one fraction of the surface buoyancy flux B_0.

The resulting length scale L_0 has two physical interpretations. First, the length scale L_0 can be interpreted as an Ozmidov scale $(\varepsilon/N^3)^{1/2}$, which is a measure of the smallest eddy size affected by a background stratification N^2 in a turbulent field characterized by a viscous dissipation rate ε (see, e.g., Ozmidov, 1965; Smyth and Moum, 2000). In the CBL, the direct influence of N^2 concentrates in the entrainment zone. Therefore, this reference Ozmidov scale L_0 can be interpreted as an estimate for an integral length scale of turbulence inside the entrainment zone, or a region therein. A second interpretation of the length scale L_0, namely, as the minimum CBL thickness, is discussed in Appendix A.

The simplest CBL problem only has two basic quantities (length and time) and four parameters $\{\nu, \kappa, B_0, N\}$. A systematic way of reducing the number of dimensional variables to a smaller number of dimensionless groups was introduced by Edgar Buckingham in 1914, which is named Buckingham Pi theorem (Buckingham, 1914). According to this theorem, the system should then depend on only two dimensionless parameters[2]. We choose them to be a reference buoyancy Reynolds number

$$\mathrm{Re}_0 = \frac{B_0}{\nu N^2} = \frac{L_0 (L_0 B_0)^{1/3}}{\nu} \, , \tag{2.4}$$

and a Prandtl number $\mathrm{Pr} = \nu/\kappa$. This work investigates the role of Re_0 only, thus we fix $\mathrm{Pr} = 1$, a value representative of atmospheric conditions. This approach reduces the amount of work needed to obtain full information about this particular CBL case, because instead of investigating separately the effects of changing the surface buoyancy flux B_0 and the stratification N^2 (and in principle, κ, though in the atmosphere, κ is given), we only need to investigate the variations with Re_0.

[2] "If an equation in n variables is dimensionally homogeneous with respect to m fundamental dimensions it can be expressed as a relation between n-m independent dimensionless groups." (Buckingham, 1914)

The reference buoyancy Reynolds number Re_0, is often used in the study of the interaction between turbulence and stable stratification (see, e.g., Hebert and de Bruyn Kops, 2006; Chung and Matheou, 2012). Re_0 is constructed using L_0 as a length scale and $(L_0 B_0)^{1/3}$ as a velocity scale. Hence, according to the interpretation of L_0 as the local integral length scale of turbulence inside the entrainment zone, Re_0 represents a Reynolds number of the turbulence inside the entrainment zone. The results that support the interpretations presented here are further discussed in Chapter 5 section 5.1.

2.2.2 Nondimensionalized independent variables

Since the system is statistically homogeneous inside the horizontal planes, the statistics depend only on the vertical distance from the surface z and time t. A naive way to nondimensionalize these variables is $\{z/L_0, tN\}$. However, an inspectional form of dimensional analysis can reveal a higher degree of similarity than a naive dimensional analysis. We therefore propose to substitute $\{z/L_0, tN\}$, without loss of generality, with the equivalent set of independent variables $\{z/z_{\mathrm{enc}}, z_{\mathrm{enc}}/L_0\}$, where

$$z_{\mathrm{enc}}(t) = \left[\frac{2B_0}{N^2}(1+\mathrm{Re}_0^{-1})(t-t_0)\right]^{1/2}, \tag{2.5}$$

is the encroachment height (Lilly, 1968; Carson and Smith, 1975) (see also Chapter 3 section 3.2). The virtual time origin t_0 quantifies the dependence on the initial condition $\langle b\rangle\,(z,0)$ and is defined such that

$$(1+\mathrm{Re}_0^{-1})B_0\,(t-t_0) = \int_0^{z_\infty} \left[\langle b\rangle\,(z,t) - b_{\mathrm{bg}}(z)\right]\,\mathrm{d}z \tag{2.6}$$

for any given time t, where

$$b_{\mathrm{bg}}(z) = N^2 z \tag{2.7}$$

is the reference background buoyancy profile, and z_∞ is located far enough into the nonturbulent stably stratified region. Angle brackets denote horizontal averaging hereinafter.

Since z_{enc} is commensurate with the CBL height for the case of a CBL growing into a linearly stratified atmosphere (see Chapter 3 section 3.1), the independent variable z/z_{enc} (or equivalent normalized height) is often employed to study the self-similar

behavior of the CBL as it grows in time. In contrast, the use of

$$z_{\mathrm{enc}}/L_0 = [2(1 + \mathrm{Re}_0^{-1})(t - t_0)N]^{1/2} \tag{2.8}$$

instead of tN to measure the state of development of the CBL is less common. The reason to use z_{enc}/L_0 in this work is twofold. First, according to the interpretation of L_0 introduced before and further discussed in Chapter 5 section 5.1, z_{enc}/L_0 is a measure of the ratio between the integral length scale of the CBL and that of the entrainment zone and is therefore one relevant measure of scale separation in the CBL. Second, z_{enc}/L_0 retains the effect of both N and B_0 simultaneously such that we can study both the weak stratification regime – relatively thick EZ – and the strong stratification regime – relatively thin EZ – in a single simulation as z_{enc}/L_0 grows in time. According to the results presented in the following section, the distinction between the weak and strong stratification regimes occurs at $z_{\mathrm{enc}}/L_0 \simeq 10$.

For comparison with the atmospheric CBL, we use the estimates $L_0 \simeq 20 - 200$ m [derived from typical values $N \simeq 0.6 - 1.8 \times 10^{-2}$ s^{-1} and $B_0 \simeq 0.3 - 1.0 \times 10^{-2}$ m^2 s^{-3} (Fedorovich et al., 2004b; Träumner et al., 2011)], $z_{\mathrm{enc}} \simeq 1000$ m, and $\nu = 1.5 \times 10^{-5}$ m^2 s^{-1} to obtain $z_{\mathrm{enc}}/L_0 \simeq 5 - 50$ and $\mathrm{Re}_0 \simeq 6 \times 10^5 - 2 \times 10^7$. Our simulations reach up to $z_{\mathrm{enc}}/L_0 \simeq 26$ (see Table 2.1), which is representative of atmospheric conditions, and covers the different stratification regimes considered in Fedorovich et al. (2004b), whose weakest and strongest stratification cases correspond to values $z_{\mathrm{enc}}/L_0 \simeq 7.3$ and $z_{\mathrm{enc}}/L_0 \simeq 23.5$, respectively.

2.2.3 Reynolds number similarity

To have a flow that is dynamically similar to that of atmospheric boundary layer flows, Re_0 needs to be matched. For laboratory and numerical experiments of atmospheric flows, dynamical similarity is a statement of an ideal due to the difficulty in matching the Reynolds number of the atmosphere. In our simulations, the Reynolds numbers $\mathrm{Re}_0 = 42$ and $\mathrm{Re}_0 = 117$ are still orders of magnitude smaller than atmospheric values (see Table 2.1). However, basic turbulence research is also interested in the asymptotic behavior of the system and of certain statistics when the Reynolds number is increased.

In particular, we are interested in observing how certain statistics become insensitive of the increase in Reynolds number. For example, numerical simulations with

moderate Reynolds numbers (e.g. Spalart et al., 1991; Coleman et al., 1994) show that first- and second order statistics are sufficiently accurate even with moderate values of the Reynolds number. These statistics are said to exhibit Reynolds number similarity: the principle, based on observation, that statistics related to the large scales become independent of the Reynolds number once this is large enough (Tennekes and Lumley, 1972; Dimotakis, 2000; Monin and Yaglom, 2007). This happens because the separation between the large energy-containing scales and the small dissipative scales is wide enough so that the large scales barely feel the effects of viscous dissipation and further increasing the Reynolds number simply increases this scale separation. However, properties that strongly depend on the smaller scales (like intermittency and higher-order statistics) might need larger scale separation for the findings to be scalable to higher Reynolds numbers (Dimotakis, 2000). One is therefore more cautious in transferring information to and making statements about the full scale analog of the flow for these statistics.

In this study, we show in Chapter 3 that despite the moderate Reynolds numbers $\mathrm{Re}_0 \simeq 100$ achieved in our DNS, mixed layer statistics follow the expected scalings based on the encroachment and the convective scales, thus reproducing the behavior previously reported from atmospheric measurements and LES. Such qualitative agreement indicates Reynolds number similarity, and we confirm it quantitatively in two different ways.

First, we note that the increase of the CBL thickness z_{enc} entails an increase in the scale separation between z_{enc} and the reference Kolmogorov scale $\eta_0 = (\nu^3/B_0)^{1/4}$ according to

$$\frac{z_{\mathrm{enc}}}{\eta_0} = \mathrm{Re}_*^{3/4} \,, \tag{2.9}$$

where the convective Reynolds number is defined as

$$\mathrm{Re}_* = \frac{z_{\mathrm{enc}} w_*}{\nu} = \left(\frac{z_{\mathrm{enc}}}{L_0}\right)^{4/3} \mathrm{Re}_0, \tag{2.10}$$

and the velocity w_* is the convective velocity (Deardorff, 1970)

$$w_* = (B_0 z_{\mathrm{enc}})^{1/3}. \tag{2.11}$$

The convective Reynolds number is associated to the large-scale convective motions and characterizes the turbulence inside the mixed layer. Since the advancement in time is equivalent to the increase in $z_{\mathrm{enc}}(t)$ (see Eq. 2.5), temporal evolution of

quantities can be equivalently thought of as their evolution as $\mathrm{Re}_*(t)$ increases. As a corollary, a quasi-steady or self-similar behavior of any statistic as the CBL grows can be interpreted as independence from the convective Reynolds number. The observations in this study that the large-scale statistics start to show a relatively small dependence on the Reynolds number as we approach values $\mathrm{Re}_* \simeq 10^4$ is in accord with the behavior reported in other turbulent flows (Dimotakis, 2000).

Second, we compare the simulations Re040 and Re100 (see Table 2.1), whose viscosities are roughly a factor of three different from each other. In this way, we can ascertain if temporal variations in certain statistics are due to low Reynolds number effects in our DNS or, on the contrary, represent a true dependence on the CBL state (measured in terms of the normalized time tN or the normalized height z_{enc}/L_0) and are therefore applicable to the atmosphere. By comparing both cases, we show throughout this study that Reynolds number effects on the results that we discuss are small (at most 15%) for the statistics we are interested in. This is particularly important for the detailed discussion of the entrainment zone in Chapter 5.

Interpreting the moderate Reynolds number of our simulations

Since Re_0 is composed of $\{B_0, N, \nu\}$, the moderate Reynolds number implies that if we choose to match the values of these parameters with those typical of the atmosphere, one of the parameters can never be matched. For the highest value of Re_0 that we achieve (117) (see Table 2.1), if we first impose a particular B_0 of typical atmospheric values (1.0×10^{-2} m^2 s^{-3}) and kinematic viscosity ν of the air (1.5×10^{-5} m^2 s^{-1}), then N (in units of s^{-1}) will be, 2.4 s^{-1}, two orders of magnitude larger than that of typical atmospheric conditions ($0.6 - 1.8 \times 10^{-2}$ s^{-1}). The corresponding buoyancy gradient is actually very strong, which makes sense since we need to fit the three layers (mixed layer, entrainment zone, free troposphere) in our small domain. In particular, these values of B_0 and N yield $L_0 = 2.7 \times 10^{-2}$m, and since we reach $z_{\mathrm{enc}}/L_0 = 18$ for this case, the height of the CBL is roughly half a meter. This interpretation can be used to define a laboratory experiment like that of Deardorff (1980a) (see Fig. 2.2). Second, if we instead choose to impose atmospheric values for N and ν, then B_0 has to be very weak ($0.63 - 5.7 \times 10^{-7}$ m^2 s^{-3}), the corresponding L_0 then ranges from $0.31 - 0.54$ m. This interpretation also yields a small CBL of $5.6 - 9.7$ m when $z_{\mathrm{enc}}/L_0 = 18$. Last, if we instead take atmospheric values for B_0 and N, then we attain a value for the kinematic viscosity $\nu = 0.17 - 1.6$ m^2 s^{-1}, a viscosity larger than that of molasses. One can imagine an

atmosphere of the realistic size but is filled with very viscous fluid instead of air.

2.3 Direct numerical simulation

To avoid the closure problem, we use direct numerical simulation, an approach whose main principle is to numerically solve the equations of fluid motion that are neither averaged nor filtered. The range of scales of the flow that are explicitly resolved include the large energy-containing scales (imposed by whatever is forcing the turbulence in the flow or by the flow boundaries) down to the small dissipative scales that are of the order of the Kolmogorov length scale, defined as

$$\eta = (\nu^3/\varepsilon)^{1/4} \tag{2.12}$$

where ν is the kinematic viscosity and ε is the rate of viscous dissipation of kinetic energy. Since the dissipation spectra peaks at around 24η (see, e.g., Pope, 2000), it is more than enough to resolve the Kolmogorov length to ensure the inclusion of the dissipative action of viscous forces; depending on the numerical scheme adopted, even just down to around $3-10\eta$ is sufficient (Moin and Mahesh, 1998). The crucial point is to resolve down to the dissipative scales because if not enough of them are resolved, the build up of energy due to lack of dissipation could lead to blow up of the numerical solution. In some circumstances, the numerical model wrongly remedies this problem by introducing spurious and nonphysical numerical dissipation. Thus, the differentiating principle of DNS is that it represent viscous dissipation physically and not through a turbulence model that tries to mimic the dissipative action of the small scales.

2.3.1 Advantages of DNS

As already mentioned in the introduction, the main advantage of DNS is that it allows for simulations that are independent of the grid resolution for a given Reynolds number, independent of the numerical algorithm, and free from the uncertainty of turbulence models. This advantage allows for transparent comparisons between different studies and confident quantification of the asymptotic behavior of statistics with respect to the Reynolds number.

Although the absence of subgrid-scale models for turbulence in DNS is indeed the

main advantage of DNS over LES, it is possible that one would think that DNS is then an LES with a simple SGS closure. At the regions where the large-scale dominates the statistics and the scale separation between the large scale and the smallest resolved scale is large enough, there is indeed not much difference between DNS and LES when only large scale statistics are of interest. But viewing DNS as such is an over-simplification that sometimes does not work: in strongly anisotropic regions, like the near-wall region and in strongly stratified regions, like the entrainment zone, the correspondence between LES and DNS can become more difficult, at least for the moderate values of effective Reynolds numbers that LES usually considers (see, e.g., Stevens et al., 2000b). Here the effects of SGS fluxes are significant yet obscured and most of the time nonphysical. Near solid boundaries, the energy transfer may be from the SGS to the resolved scales, while LES prediction of the entrainment zone thickness, especially at large values of N, could not be as reliable due to poor performance of SGS models in the strongly stratified regions (Sorbjan, 1996; Fedorovich et al., 2004b). Furthermore, Deardorff (see Fox and Deardorff, 1972) found that the commonly-used Smagorinsky model smears out the mean buoyancy gradient that forms in penetrative convection. In the same spirit as the simplistic view on DNS, LES can be considered as a theoretically high Reynolds number flow with a dubious way of turbulent mixing. To improve the representation of unresolved scales, Deardorff (1973) proposed a more complex SGS model that involves transport equations for the SGS stresses, in particular ten additional transport equations. Although the Deardorff SGS model, and even more complex SGS models (Kleissl et al., 2006) may lead to improved results, the additional work needed to develop and evaluate these more complex models undermines the practicality of doing an LES.

Indeed, there is a limit to the practicality and validity of LES. We always need to ask whether we are saving enough points and can get away with a simple SGS to address the questions we want to investigate. Towards the investigation of regions where LES is questionable and would require more points and more complex SGS models, one should ask whether it is worth pushing through using LES or instead do a clean DNS. The choice is between accurately solving the Navier-Stokes equations, which have been practically proven in time to be a very good model for fluid flows during the last 150 years or solving filtered equations with different closure models, all of which have been proven to be wrong (although sometimes practical) during the last 50 years.

2.3.2 Limitations of DNS

The well-known limitation of DNS is its restriction to moderate Reynolds number due to limitations in computing power and computer memory. Unlike laboratory experiments wherein parameters such as the dynamic viscosity can be tweaked to crank up the Reynolds number, the only way to increase the Reynolds number in a simulation is to have more grid points, which requires more computing power and memory. The size of the simulation, consequently the number of grid points, is dictated by the two extremes of the range of scales: first, the domain has to be large enough such that the largest turbulent scale of the flow is contained within the computational domain and that statistical convergence is good enough; second, the grid spacing must be sufficiently small to resolve the dissipative scales. In between these two limits, there should be a wide enough range of intermediate scales such that there is enough scale separation between the large energy-containing scales and the small dissipative scales. In terms of the energy- and dissipation spectra, they should not overlap for Reynolds number similarity to be observed in the large-scale statistics (see, e.g., Pope, 2000).

For the CBL, the largest length scale is typically characterized by the CBL thickness, which is of order 10^3 meters, while the Kolmogorov length scale is of the order 10^{-3} meters (see, e.g., Orlanski, 1975). The ratio of these two scales (cubed) yields an estimate for the total number of grid points needed to resolve the entire range of scales[3], therefore at least $O(10^{18})$.

As of 2013, the highest number of degrees of freedom achieved for a DNS is of the order 10^{11} (Lee et al., 2013), while our largest simulation is of the order 10^{10}. The gap between achieved and atmospheric Reynolds numbers is already daunting and we have not even mentioned the number of iterations needed for such a simulation. However, this should not undermine the use of DNS since observation of Reynolds number similarity in statistics of increasing order in state-of-the-art DNS of turbulent flows (Jimenez, 2013) and development of more powerful supercomputers that would allow an increase in achievable Reynolds numbers, encourage further use and development of DNS as a clean research tool in atmospheric turbulence.

[3]Although for the CBL, and ABL in general, the vertical direction usually requires fewer grid points due to smaller extent of vertical scales compared to the horizontal. Also, the number of grid points needed to resolve the Kolmogorov scale depends on the employed numerical scheme.

2.3.3 Numerics

As discussed in Rogallo and Moin (1984) and Moin and Mahesh (1998), there are four main issues that require careful consideration for numerically solving the Navier-Stokes equations. These are

- discretization of spatial derivatives
- time-stepping algorithm
- initial and boundary conditions
- computer implementation and organization

In each category there are different options available. We do not discuss these issues in detail and simply refer the reader to the aforementioned references. We instead discuss briefly our choice for each category and our justification for these choices.

Discretization of spatial derivatives

Discretization of equations (2.2) in space is performed using sixth-order spectral-like compact finite-differences on a structured Cartesian grid. Finite differences are chosen over spectral methods even though the latter yields higher accuracy for the same number of grid points, because standard spectral methods do not easily allow the use of non-uniform grids, which we employ for grid refinement and stretching at the vertical direction. Sixth-order-accurate scheme is chosen over a second-order finite difference scheme since care and accuracy are needed for resolving down to Kolmogorov scale and the accuracy required to do such would require more grid points if second-order finite differences were used.

In our simulation of the CBL, we take care of resolving the near-wall region where the diffusive layer is located. Experiments on the neutrally-stratified $N^2 = 0$ case (so-called 'heated plate' case) (see Mellado, 2012) have established that the required resolution using the finite difference scheme we chose is $\Delta z/\eta \simeq 1.2$ or less, where Δz is the vertical grid spacing. We resolve the Kolmogorov scales such that further grid refinement does not affect the statistics because the results are already converged (see Appendix B). Since the Kolmogorov scales in the mixed layer are larger than those in the surface layer, we employ grid stretching at the vertical to spare grid points in that direction.

Time-stepping algorithm

Due to the wide range of interacting time scales, turbulent flows are considered stiff systems (Moin and Mahesh, 1998). This means that time discretization schemes easily become numerically unstable unless the time step used for numerical integration is taken to be extremely small. Advancement in time for the numerical integration may be done either explicitly (next time step is solved from a few terms of the previous time steps) or implicitly (a coupled system of equations is solved).

We use an explicit, low-storage, fourth-order accurate, Runge-Kutta scheme to discretize time. Explicit schemes are much easier to implement and have a much lower cost per step. Since we use an explicit method, a Poisson equation for pressure is solved at every time step to implement the incompressibility constraint. In our DNS, the discrete solenoidal constraint is satisfied to machine accuracy using a Fourier decomposition along the periodic horizontal planes x_1Ox_2 and a factorization of the resulting set of equations along the vertical coordinate (Mellado and Ansorge, 2012).

Initial and boundary conditions

Initial velocity field generally has to satisfy the continuity equation. In the CBL case, we begin with a fluid at rest, therefore $\mathbf{v} = \mathbf{0}$. The buoyancy field is imposed as

$$b(\mathbf{x}, 0) = b_i \left[1 - \mathrm{erf}\left(\frac{\sqrt{\pi}}{2} \frac{z}{\delta_i} \right) \right] + b_{\mathrm{bg}}(z) \ , \tag{2.13}$$

where $b_{\mathrm{bg}}(z)$ is the background buoyancy profile, Eq. (2.7), N being the Brunt-Väisälä frequency. The fields $b_i(x_1, x_2)$ and $\delta_i(x_1, x_2)$ are the surface buoyancy and the gradient thickness, respectively, so that the local vertical buoyancy flux at the surface corresponding to this initial condition is $-\kappa \partial b/\partial z = \kappa(b_i/\delta_i - N^2)$. A random fluctuating buoyancy field is superimposed on a prescribed mean buoyancy profile to hasten the transition to turbulence. Following Mellado (2012), we impose an initial broadband perturbation $\zeta(x_1, x_2)$ such that $b_i(x_1, x_2) = b_s(1 + \zeta)$ and $\delta_i(x_1, x_2) = \delta_s(1 + \zeta)$, where ζ has a Gaussian power spectral density, centered at a given spatial frequency $1/\lambda$ and with a standard deviation equal to $1/(6\lambda)$. The standard deviation is chosen such that spatial frequencies below $1/(2\lambda)$ have practically no energy. The phase of ζ is random. The constant surface buoyancy flux $B_0 = \kappa(b_s/\delta_s - N^2)$ is imposed by choosing appropriate values for b_s and δ_s.

No-penetration, no-slip boundary condition is used at the bottom plate and no-penetration, free-slip boundary conditions at the top. Neumann boundary conditions are used for the buoyancy at the top and the bottom to maintain fixed constant

fluxes. In addition, the velocity and buoyancy fields are relaxed towards zero and the background buoyancy profile $b_{\mathrm{bg}}(z)$, respectively, inside a sponge layer occupying the upper region of the computational domain. Preliminary simulations (not shown) have been used to adjust the height of the top boundary so that it is far enough from the turbulent region to avoid any significant interaction. Since the CBL is assumed to be statistically horizontally homogeneous, periodicity is used at the side boundaries.

Computer implementation and organization

The DNS code is written in Fortran90 and uses hybrid parallelization: MPI using domain decomposition in the two horizontal directions (pencils), and using OpenMP to further parallelize within each node the loops where the linear systems are solved and where the different terms are added to the right-hand-side of the transport equations. The size of the domain decomposition in each of the two horizontal directions can be tuned to get the best scaling.

Computations are done on Forschungscentrum Juelich's JUQUEEN, an IBM BlueGene/Q system based on the IBM POWER architecture hosting 458,752 compute cores. The system is especially designed for computationally intensive, highly scalable applications which can run in parallel on a very high number of compute cores.

2.3.4 Simulation specifics

Simulation	Grid	Re_0	Re_q	Re_*	z_{enc}/L_0	z_{enc}/η	δ/L_0
Re100	$5120 \times 5120 \times 840$	117	2860	5480	18	490	1.3
Re040	$2560 \times 2560 \times 704$	42	1600	3160	26	320	1.6

Table 2.1: Simulation properties. Columns 4-8 provide data at the final time of the simulations. The convective Reynolds number Re_* is defined by Eq. (2.10) and the turbulent Reynolds number $\mathrm{Re}_q = e^2/(\varepsilon\nu)$, where e is the turbulence kinetic energy and ε its viscous dissipation rate, is the maximum value within the CBL. The Kolmogorov scale $\eta = (\nu^3/\varepsilon)^{1/4}$ is the minimum value within the CBL. The length scale δ is defined by Eq. (5.2).

The two simulations considered in the study are summarized in Table 2.1. The size of the computational grid is $5120 \times 5120 \times 840$ for the reference case denoted as Re100. Stretching is used in the vertical direction to increase the resolution near the surface and to move the top boundary farther up, so that the domain size is

$215L_0 \times 215L_0 \times 56.6L_0$, where L_0 is the reference length scale defined in Eq. (2.3). The simulation is terminated when the boundary layer thickness is about $18L_0$. At the final time, the aspect ratio of the horizontal domain size and the CBL height is around 12:1. The second simulation Re040 in Table 2.1 with a reference Reynolds number Re_0, defined in Eq. (2.4), roughly a third of that of Re100 has been used to study the effect of Re_0 and to achieve a deeper CBL, up to $26L_0$. The horizontal size of the computational domain in Re040 is the same as in Re100.

For reference, the value $\mathrm{Re}_* \simeq 2500$ from the simulation Re040 closely matches the value from the experiment of Deardorff et al. (1980) on a 1.14 m $\times$ 1.22 m-wide water tank. However, those tank experiments have quite a low Re_0, about 10; they achieve a comparable Re_* because z_{enc}/L_0 is larger, about 50. To reach a Reynolds number Re_* similar to that of simulation Re100, the CBL of the tank experiment would have to grow from 0.27 m to 0.46 m, and to obtain a similar aspect ratio of the horizontal dimension to the CBL height as in the simulations, the tank would need to be 6 m $\times$ 6 m wide.

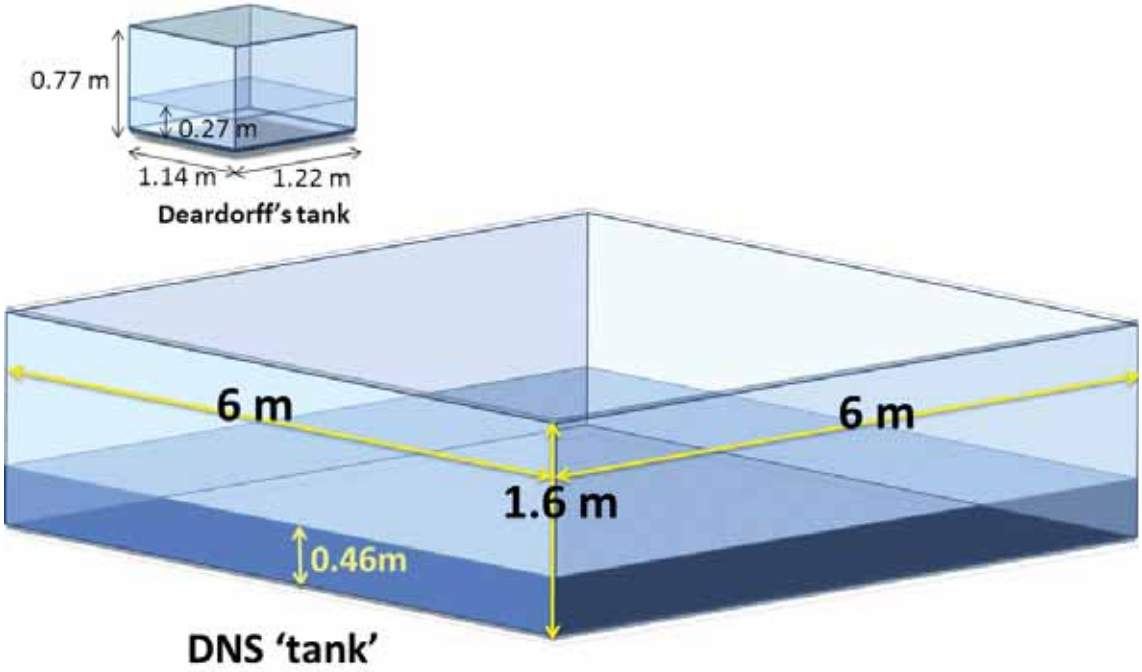

Figure 2.2: Size comparison between the Deardorff (1980a) water tank and the water-tank equivalent of the Re100 DNS simulation.

3 Mixed layer statistics

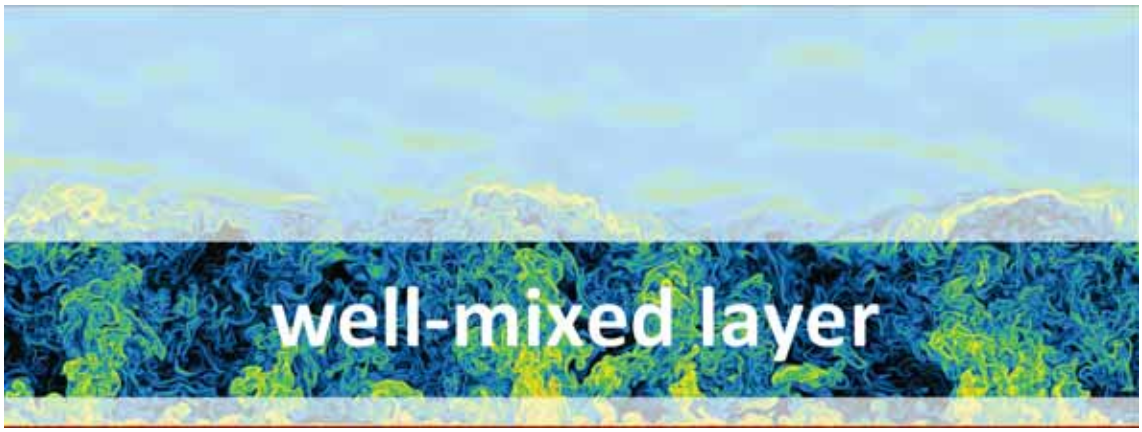

The main goal of this chapter is to show that the scale separation between the large energy-containing scales, characterized by the CBL thickness, and the small dissipative scales, characterized by the Kolmogorov length, is large enough for statistics related to the large-scales to be comparable to those from large-eddy simulations and field observations. These well-known statistics are:

- Convective boundary layer thickness
- Vertical profiles of mean and variance of buoyancy and velocity
- Vertical profiles of higher-order moments of the vertical velocity
- Turbulence kinetic energy budget profiles

We further show that the interval of CBL heights beyond $z_{\rm enc}/L_0 \simeq 10$ that we consider in this study corresponds to the equilibrium entrainment regime (Fedorovich et al., 2004b).

3.1 The convective boundary layer thickness

We consider the following definitions of the height of the CBL top, $z_{i,\xi}$, as introduced before in the literature (see, e.g., Garratt, 1992; Sullivan et al., 1998):

1. The zero-crossing height $z_{i,0}$, where the total buoyancy flux

$$B = \langle b'w' \rangle - \kappa \frac{\partial \langle b \rangle}{\partial z} \tag{3.1}$$

becomes negative. An apostrophe indicates turbulent fluctuation (deviation from the horizontal plane average).

2. The integral-based height

$$z_{i,i}(t) = 2.5 \frac{1}{B_0} \int_0^{z_\infty} \langle b'w' \rangle \, \mathrm{d}z, \tag{3.2}$$

where the integral extends far enough into the nonturbulent stably-stratified region. The factor 2.5 comes from assuming a linearly decreasing buoyancy flux profile that has a minimum buoyancy flux value of $-0.2B_0$ (see Deardorff, 1970).

3. The flux-based height $z_{i,f}$, where the total buoyancy flux B is minimum.

4. The variance-based height $z_{i,v}$, where the buoyancy variance $\langle b'b' \rangle$ is maximum away from the near-wall region.

5. The gradient-based height $z_{i,g}$, where the mean buoyancy gradient is maximum away from the near-wall region.

We compare these heights, normalized with the encroachment height z_{enc} (Eq. 2.5), in Fig. 3.1. When the thickness of the CBL becomes an order of magnitude larger than L_0, all of the normalized heights become statistically steady in time, within the statistical convergence that we can achieve. Table 3.1 summarizes the values of the corresponding constant

$$C_{\mathrm{enc},\xi} = z_{i,\xi}/z_{\mathrm{enc}} \, . \tag{3.3}$$

This steadiness implies that z_{enc} already gives the correct evolution in time of the growth of the dry CBL into a linearly stratified fluid (Driedonks, 1982). The mean entrainment rate

$$w_{\mathrm{e},\xi} = \frac{\mathrm{d}z_{i,\xi}}{\mathrm{d}t} \tag{3.4}$$

can then be approximated as

$$w_{\mathrm{e},\xi} \simeq C_{\mathrm{enc},\xi} \frac{\mathrm{d}z_{\mathrm{enc}}}{\mathrm{d}t} = C_{\mathrm{enc},\xi} N L_0 (z_{\mathrm{enc}}/L_0)^{-1} \tag{3.5}$$

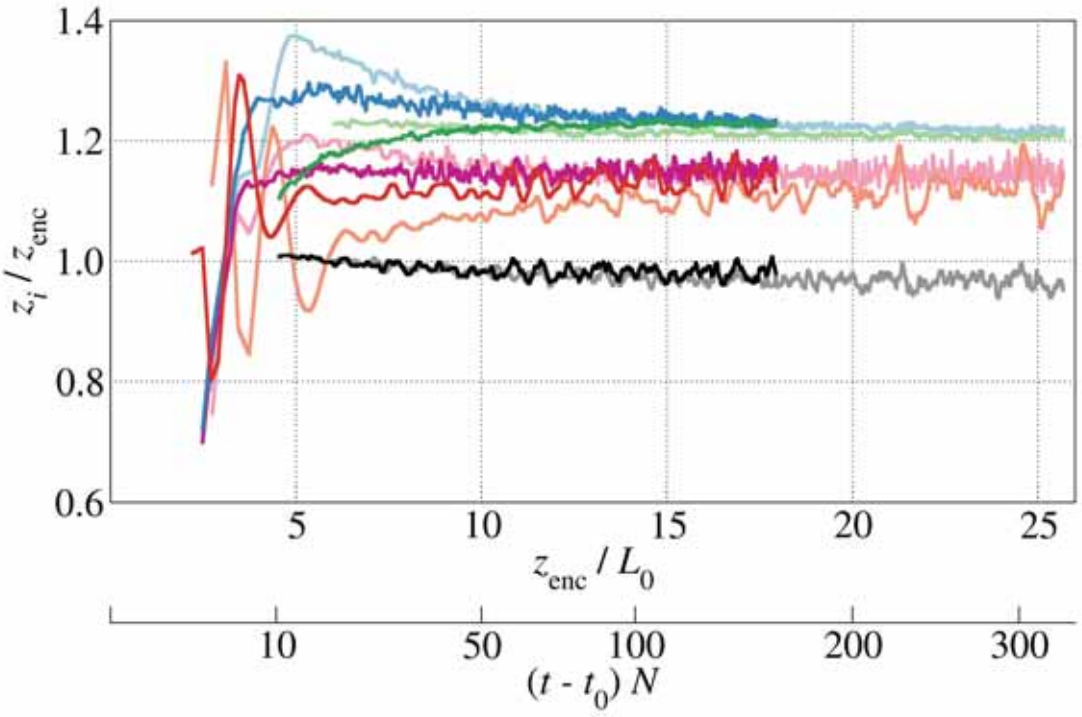

Figure 3.1: Temporal evolution of the normalized CBL-top heights, defined in section 3.1: zero-crossing of buoyancy flux $z_{i,0}$ (black); integral-based $z_{i,i}$ (red); flux-based $z_{i,f}$ (magenta); variance-based $z_{i,v}$ (green); gradient-based $z_{i,g}$ (blue). The corresponding mean values beyond $z_{\mathrm{enc}}/L_0 \simeq 10$ are summarized in Table 3.1. Light colors correspond to Re040, dark colors to Re100.

for $z_{\mathrm{enc}}/L_0 \geq 10$. Hence, the range of values of $C_{\mathrm{enc},\xi}$ gives a variability of $\simeq 25\%$ in w_{e} depending on the height $z_{i,\xi}$ that is used to define the CBL top. In particular, the mean entrainment rate differs by roughly 10% between the common CBL-top height definitions $z_{i,f}$ and $z_{i,g}$. We will denote $\mathrm{d}z_{\mathrm{enc}}/\mathrm{d}t$ as w_{e}.

	Heights	$z_{i,0}$	$z_{i,i}$	$z_{i,f}$	$z_{i,v}$	$z_{i,g}$
Re040	Mean	0.97	1.11	1.15	1.21	1.23
	$\sigma(\%)$	1.0	2.1	1.1	0.36	0.83
Re100	Mean	0.98	1.13	1.15	1.23	1.24
	$\sigma(\%)$	1.0	1.6	0.9	0.29	0.54

Table 3.1: Normalized CBL-top height constants $C_{\mathrm{enc},\xi}$, Eq. (3.3), calculated for all the different height definitions $\{z_{i,\xi} : \xi = 0, i, f, v, g\}$ introduced in section 3.1 and shown in Fig. 3.1, using the data for $z_{\mathrm{enc}}/L_0 \geq 10$.

We emphasize that, according to Fig. 3.1 and Table 3.1, the Reynolds number dependence of the entrainment rate w_e after the initial transient, beyond $z_{enc}/L_0 \simeq 5-10$, is already negligibly small for the Reynolds numbers achieved in these simulations, only about 2% and comparable to the statistical convergence. The analysis done on the surface layer (Chapter 4) and on the entrainment zone (Chapter 5) focuses on this fully developed regime that begins when the initial conditions have been sufficiently forgotten.

The different CBL-top heights are ordered according to

$$z_{i,0} \leq z_{enc} < z_{i,i} \leq z_{i,f} < z_{i,v} \leq z_{i,g} \ , \tag{3.6}$$

in agreement with previous results (Sullivan et al., 1998; Fedorovich et al., 2004b). Approximately, there are only three distinct heights since we observe that $z_{i,0} \simeq z_{enc}$, $z_{i,i} \simeq z_{i,f}$, and $z_{i,v} \simeq z_{i,g}$. These three heights are depicted as three white bars in Fig. 3.2, which visualizes a vertical cross-section of the CBL using the magnitude of the buoyancy gradient. The entrainment zone, whose location is roughly indicated by these three heights, is dominated by both sharp gradients at the crests of the undulations, or domes, and the entrained fluid regions between those domes, or troughs. The smallest of the three heights, the zero-crossing height of the buoyancy flux, was used in the original study of Deardorff et al. (1980), and is said to characterize the top of the well-mixed layer, which is supported by the visualization in Fig. 3.2 (see also Fig. 5.3d). The largest of those heights, $z_{i,g}$, seems to mark the mean vertical extent reached by the penetrating thermals. We will discuss in Chapter 5 the details of this entrainment region that develops between $z_{i,0}$ and $z_{i,g}$.

3.2 The encroachment scales

One of the early attempts to characterize the CBL height was the encroachment height (Lilly, 1968; Carson and Smith, 1975) that is derived by considering only the thermodynamics and neglecting turbulent entrainment (see Stull, 1988). This approximation is equivalent to the 'minimum entrainment' condition (Ball, 1960; Lilly, 1968), where the buoyancy flux at the mixed layer–free troposphere boundary is set to zero. The corresponding piecewise linear mean buoyancy profile is defined as

$$\langle b \rangle_{enc}(z,t) = \max\{b_{bg}(z), b_{bg}(z_{enc}(t))\}. \tag{3.7}$$

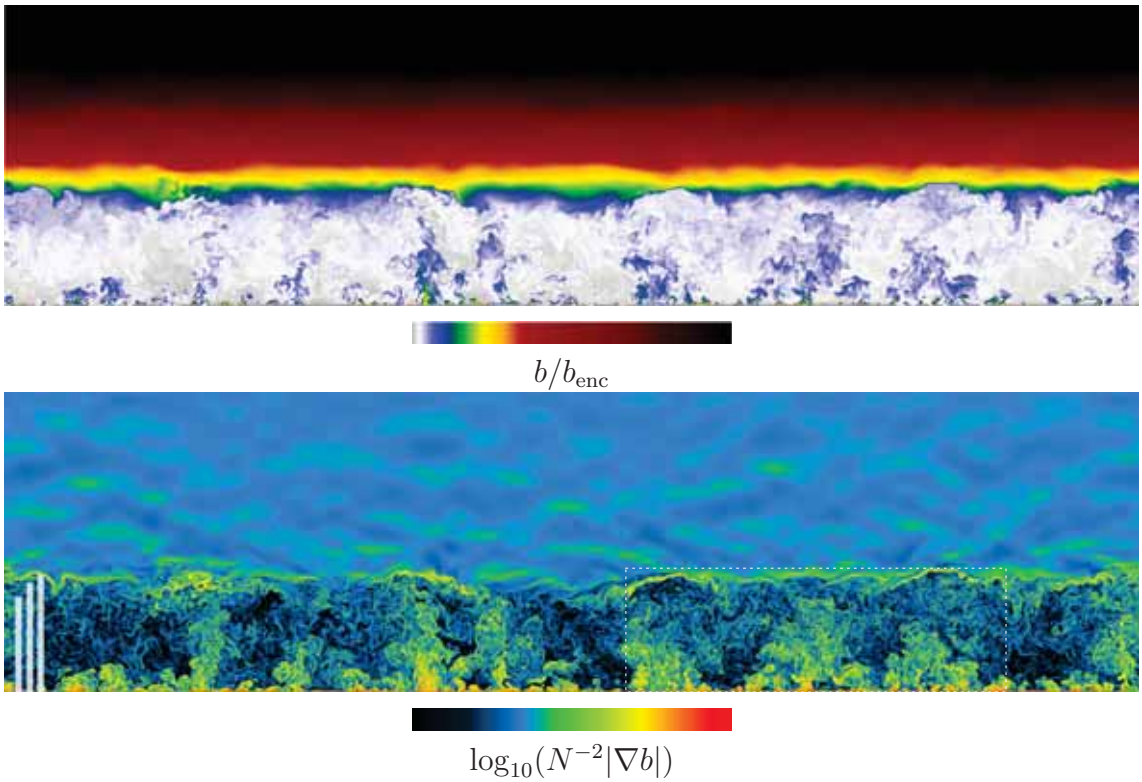

Figure 3.2: Vertical cross-section of the CBL showing the normalized buoyancy b/b_{enc} (top) and the logarithms of the magnitude of the buoyancy gradient $N^{-2}|\nabla b|$ (bottom) for case Re100 at the final time $z_{\mathrm{enc}}/L_0 = 18$. For buoyancy: gray $b < b_{\mathrm{enc}}$, white $b = b_{\mathrm{enc}}$, blue $b = 1.1b_{\mathrm{enc}}$, green $b = 1.2b_{\mathrm{enc}}$, yellow $b = 1.3b_{\mathrm{enc}}$, orange $b = 1.4b_{\mathrm{enc}}$, red $b = 1.5b_{\mathrm{enc}}$, dark red $b = 2.0b_{\mathrm{enc}}$, and black $b = 2.5b_{\mathrm{enc}}$. For buoyancy gradient: colors black, blue, yellow and red correspond, respectively, to values varying between 10^{-1} and 10^{2} in intervals of 10. The top of the three white vertical bars indicates the location of the different CBL height definitions, from left to right: the encroachment height z_{enc}, the flux-based height $z_{i,f}$, and the gradient-based height $z_{i,g}$.

In a bulk model sense, the encroachment buoyancy profile is the crudest approximation to that of the CBL since the expression above only represents a well-mixed layer with buoyancy $b_{\mathrm{bg}}(z_{\mathrm{enc}}(t))$ and an overlying stably stratified layer. The height $z_{\mathrm{enc}}(t)$ is the only unknown and is obtained with the constraint (2.6), wherein $\langle b \rangle = \langle b \rangle_{\mathrm{enc}}$. This yields the well-known expression in Eq (2.5).

The encroachment approximation to the CBL growth introduces a reference length z_{enc} for the CBL analysis, as discussed in section 2.2, and a reference buoyancy

$$b_{\mathrm{enc}} = b_{\mathrm{bg}}(z_{\mathrm{enc}}) = N^2 z_{\mathrm{enc}} \ . \tag{3.8}$$

The corresponding time scale is $\sqrt{z_{\mathrm{enc}}/b_{\mathrm{enc}}} = N^{-1}$. We refer to these scales as the

encroachment scales.

When normalized with the encroachment scales, the profiles of buoyancy-related quantities in Fig. 3.3a,b show self-similarity within the mixed layer, from $z_{\mathrm{enc}}/L_0 \simeq 10$ onward. In particular, we observe that b_{enc} represents very accurately the magnitude of the mixed layer buoyancy. However, since mixing is not instantaneous, the positive buoyancy flux at the surface and the entrainment of more buoyant air at the entrainment zone lead to slightly higher mean buoyancy at those regions and a minimum near the middle of the mixed layer. This minimum mean buoyancy $\langle b \rangle_{\mathrm{min}}$ is observed to very slightly deviate from b_{enc}; Figure 3.4a shows in more detail the tendency of the mixed layer mean buoyancy towards proportionality with the encroachment scale and the slight deviation from this scaling, measured as $\langle b \rangle_{\mathrm{min}} / b_{\mathrm{enc}}$, which is already less than 2% for $z_{\mathrm{enc}}/L_0 \simeq 10$. We observe the same increasing behavior for both Re040 and Re100, meaning the deviation does not seem to be a low Reynolds number effect. Since the effect of entrainment is not retained in the encroachment model of the CBL, the close behavior of the minimum buoyancy with the encroachment buoyancy could be an indication that the heating due to entrainment is mainly concentrated at the upper regions of the mixed layer and does not penetrate significantly down to the surface.

3.3 The convective scales

For a given boundary layer height z_i, the Deardorff convective scales (Deardorff, 1970)

$$w_* = (B_0 z_i)^{1/3} \tag{3.9}$$

$$b_* = (z_i / B_0^2)^{-1/3} \tag{3.10}$$

have been well-established as the characteristic scales of the turbulent fluctuations of buoyancy and the velocity. In this study, $z_i = z_{\mathrm{enc}}$ unless indicated otherwise. Using z_{enc} promotes transparency in comparing with other data sets since z_{enc} is analytically derivable and does not suffer from the statistical uncertainty of other height definitions. The use of other height definitions can easily be taken into account using the constants found in Table 3.1.

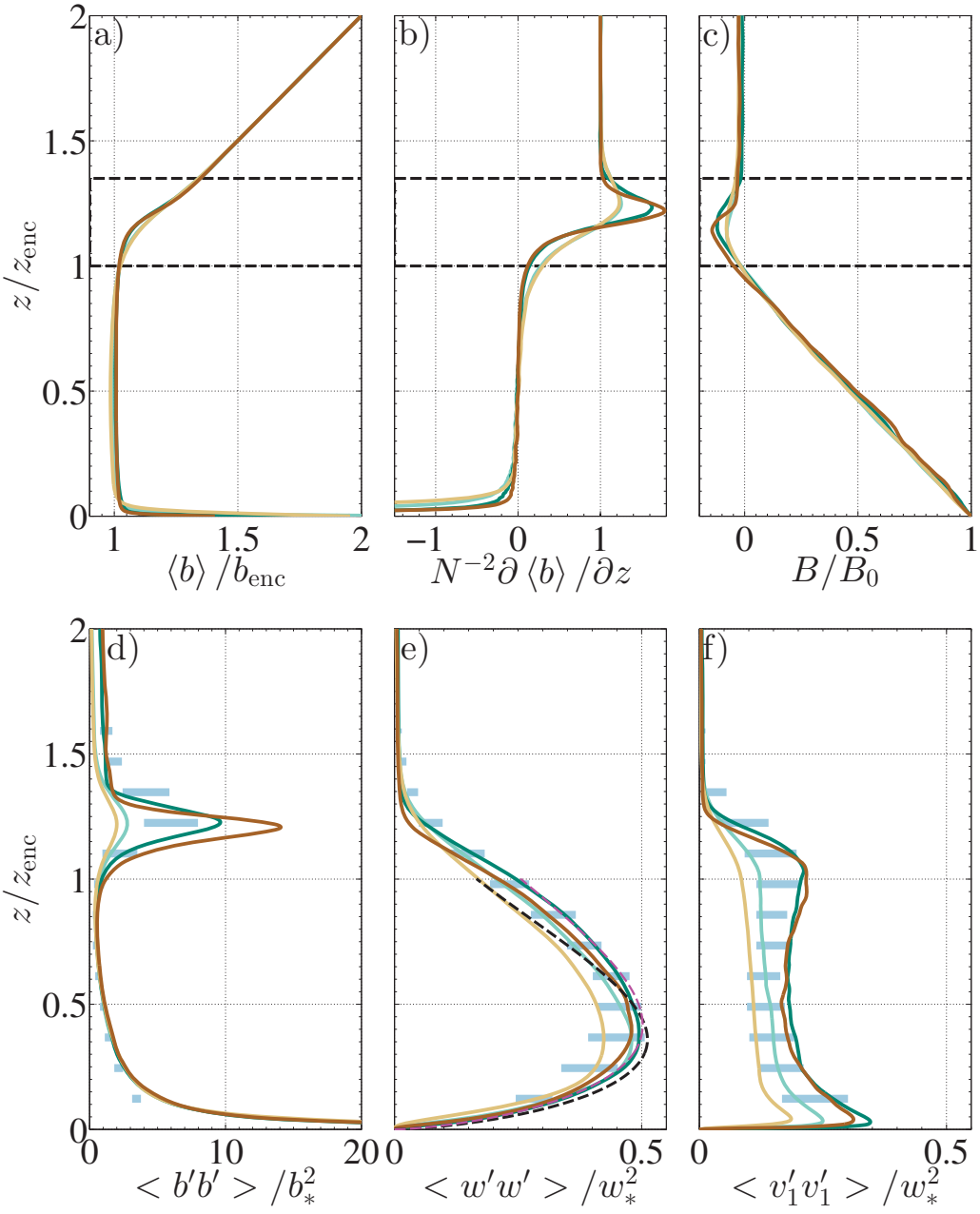

Figure 3.3: First row from left to right: normalized vertical profiles of the mean buoyancy $\langle b\rangle$, the mean buoyancy gradient $\partial\langle b\rangle/\partial z$ and the total mean buoyancy flux $B = \langle b'w'\rangle - \kappa\partial\langle b\rangle/\partial z$. Second row from left to right: normalized vertical profiles of the variance of the buoyancy and the vertical and horizontal velocities. The vertical profile of the vertical velocity variance suggested in Lenschow et al. (1980) using the coefficients used there (dashed black line) and using the coefficients according to a best fit to the data (dashed magenta line) are included in panel e. Blue bars indicate the spread of LES data values at approximately $z_{\mathrm{enc}}/L_0 = 12$ from Fedorovich et al. (2004a). Blue indicates Re100 and brown indicates Re040. Light to dark colors indicate snapshots at $z_{\mathrm{enc}}/L_0 \simeq \{10, 18\}$, respectively, for Re100. For Re040 case, snapshots at $z_{\mathrm{enc}}/L_0 \simeq \{10, 26\}$ are included.

Figure 3.3d-f shows that the normalized vertical profile of the variance of the buoyancy fluctuations $\langle b'b' \rangle / b_*^2$, and those of both the vertical $\langle w'w' \rangle / w_*^2$ and the horizontal $\langle v_1'v_1' \rangle / w_*^2$ velocity components, exhibit the expected shapes of these profiles (Deardorff et al., 1980; Stull, 1988; Schmidt and Schumann, 1989; Moeng and Sullivan, 1994) and that within the mixed layer, the profiles at different times tend to collapse on top of each other within the achieved statistical convergence.

The spread of values for the turbulent fluctuations from the LES intercomparison of Fedorovich et al. (2004a), taken at approximately $z_{\text{enc}}/L_0 = 12$, is included in Fig. 3.3d-f. DNS data are comparable to those from LES at the well-mixed region since subgrid-scale contribution should be small because the large convective scale dominates there. Therefore LES and DNS results have to agree qualitatively. However, we note that the LES spread is comparable to the growth from $z_{\text{enc}}/L_0 = 10$ to $z_{\text{enc}}/L_0 = 26$ of the DNS data, and the variation of DNS data between the Re040 and Re100 cases at $z_{\text{enc}}/L_0 \simeq 10$. DNS data at the end of the simulation, when the Reynolds number is highest, is at the upper limit of the spread of LES values. It is possible that the spread among instantaneous values from different LES for the same time interval could be larger since the LES runs could also further vary in time, although such information is usually lost because LES results are typically averaged within certain time intervals.

We also compare the DNS vertical velocity variance profile to the vertical profile suggested in Lenschow et al. (1980)

$$\langle w'w' \rangle / w_{*,f}^2 = (k_1) \left(z/z_{i,f}\right)^{2/3} \left(1 - k_2 z/z_{i,f}\right)^2 , \tag{3.11}$$

where $k_1 = 1.8$ and $k_2 = 0.8$ are the coefficients used in Lenschow et al. (1980). The profile using these coefficients is renormalized such that $z_i = z_{\text{enc}}$ and $w_* = w_{\text{enc}}$ (see Fig. 3.3e). DNS data matches the shape, the maximum value and its location quite well. A best fit to the Re100 data at final time for $0 \leq z \leq z_{\text{enc}}$ yields the coefficients $k_1 = 1.6$ and $k_2 = 0.69$. Since the expression (3.11) is a fit to atmospheric observations (Kaimal et al., 1976), the relatively good agreement implies that despite the moderate Reynolds number of our DNS, Reynolds number independence is already achieved for the vertical velocity fluctuations within the mixed layer.

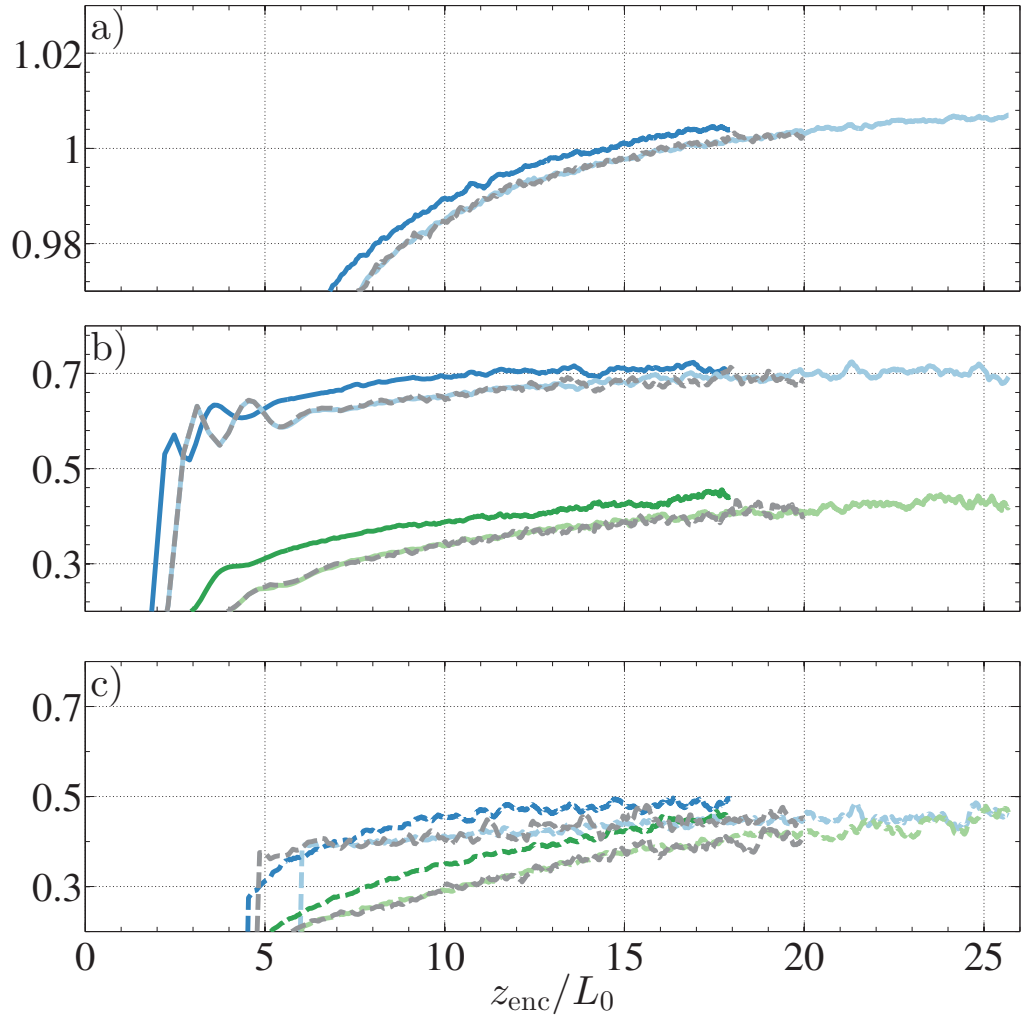

Figure 3.4: a) Temporal evolution of $\langle b \rangle_{\mathrm{min}} / b_{\mathrm{enc}}$. b) Temporal evolution of the normalized r.m.s. of vertical (blue) and horizontal (green) velocity fluctuations taken at the height of maximum w_{rms}. Average values calculated beyond $z_{\mathrm{enc}}/L_0 \simeq 10$ are summarized in Table 3.2. c) Temporal evolution of the normalized r.m.s. of vertical (blue) and horizontal (green) velocity fluctuations taken at $z/z_{\mathrm{enc}} = 1$. Light colors correspond to Re040, dark colors to Re100. Dashed lines correspond to Re040.R1, simulation with a domain size that is half as large in each horizontal direction (Table B.1 in Appendix B).

Figure 3.4b and Fig. 3.4c (measured at z/z_{enc}) show in more detail the tendency of the mixed layer velocity statistics towards proportionality with the convective scales, which extends up to the top of the mixed layer $z/z_{\mathrm{enc}} \simeq 1$. The deviation of the vertical velocity fluctuation from scaling with the convective velocity is more significant at early times, but for the case Re100, the scaling with w_* is already

observed at $z_{\rm enc}/L_0 \simeq 12$. In contrast, the deviation of the horizontal velocity fluctuation is most visible, since the scaling with w_* is observed relatively later, roughly at $z_{\rm enc}/L_0 > 16$ for Re040 and $z_{\rm enc}/L_0 > 14$ for Re100. This slower development towards being proportional to w_* is not a domain size effect, as shown in Fig. 3.4b by the collapse of the curves from the Re040 case and the Re040.R1 case with the same Re_0 but with a horizontal domain that is half as large in each horizontal direction (see Table B.1 in Appendix B).

Whereas the encroachment and convective scales are appropriate characteristic scales within the mixed layer, they are clearly inappropriate scales within the entrainment zone for both the mean and the variance of buoyancy, respectively, since the normalized mean buoyancy gradient and the normalized buoyancy variance are increasing in time (Fig. 3.3b,d). This behavior occurs for both Re040 and Re100 and has also been observed in LES data (Sorbjan, 2007), which indicates a temporal evolution of the entrainment zone different from that of the mixed layer, rather than a low Reynolds number effect. We provide in Chapter 5 more appropriate scalings for these statistics inside the EZ.

Simulation	$w_{\rm rms}/w_*$	$v_{1,\rm rms}/w_*$	$b_{\rm rms}/b_*$
Re100	0.71	0.42	1.25
Re040	0.69	0.31	1.26

Table 3.2: Time-averaged values (beyond $z_{\rm enc}/L_0 \simeq 10$) of the root-mean-square (r.m.s.) of the turbulent fluctuations taken at the height of maximum $w_{\rm rms}/w_*$.

3.4 Higher-order moments

As the order of the statistical moments increase, both statistical convergence and Reynolds number independence become poorer. To check the quality of our statistics and possible Reynolds number dependence, we show in Figure 3.5a,c the vertical velocity skewness defined as

$$S_w = \frac{\langle w'w'w' \rangle}{\langle w'w' \rangle^{3/2}}. \tag{3.12}$$

Since the mean is taken over horizontally homogeneous planes, the vertical velocity skewness serves as an indicator of the structure of convective elements in the CBL;

its positive value within the entire CBL means that the probability density function (pdf) of vertical velocity has more 'extreme' positive values, which physically means that the rising thermals (or updrafts) are faster and narrower than the surrounding downdrafts (Moeng and Rotunno, 1990). This statistic is of interest in dispersion studies (see Lenschow et al., 2011, and references therein) and is of importance to the vertical transport of turbulence kinetic energy, which we show in the next section.

Regarding Reynolds number similarity, we see that for an earlier time, the skewness at $z/z_{\text{enc}} \simeq 0.8$ and farther into the entrainment zone is larger than for later times (Fig. 3.5a) and values at the surface layer are smaller than those during later times (Fig. 3.5c). We interpret this as a Reynolds number effect since advancement in time is equivalent to an increase in the convective Reynolds number (see Chapter 2 section 2.2.3). A similar behavior is observed in Sullivan and Patton (2011) for the same quantity but instead of varying the Reynolds number, the grid resolution is refined; Coarse resolution LES overpredicts S_w near and at the entrainment zone and underpredicts S_w at the surface layer. In contrast, S_w at final times of Re100 and Re040 cases are very similar in terms of magnitude within the mixed layer even up to the entrainment zone, an indication that Reynolds number independence has been achieved for this statistic within the mixed layer. The slight vertical offset may still be some low Reynolds number effect, since the Reynolds number at the entrainment zone [see Chapter 5 Eq. (5.10)] is smaller than the convective Reynolds number Re_* and may also be due to a dependence on the independent variable z_{enc}/L_0. These observations further support the interpretation that low resolution LES have low Reynolds number effects and that grid refinement, instead of the addition of a subgrid-scale model, increases the scale separation between the large and the small scales by adding more small scales.

Figure 3.5b,d also shows the flatness or kurtosis of the vertical velocity, defined as

$$K_w = \frac{\langle w'w'w'w' \rangle}{\langle w'w' \rangle^2} \,, \tag{3.13}$$

which is a measure of the tails of the pdf. Large values of K_w are indicators of non-Gaussianity and intermittency, which agrees with the pronounced peak at the entrainment zone where penetrating domes with pockets of turbulence and relatively nonturbulent background fluid coexist (see Fig. 5.3 in Chapter 5). Similar to the skewness, low Reynolds number effects are observed between earlier and later times of Re100 but the good collapse between final times of Re100 and Re040 seem to

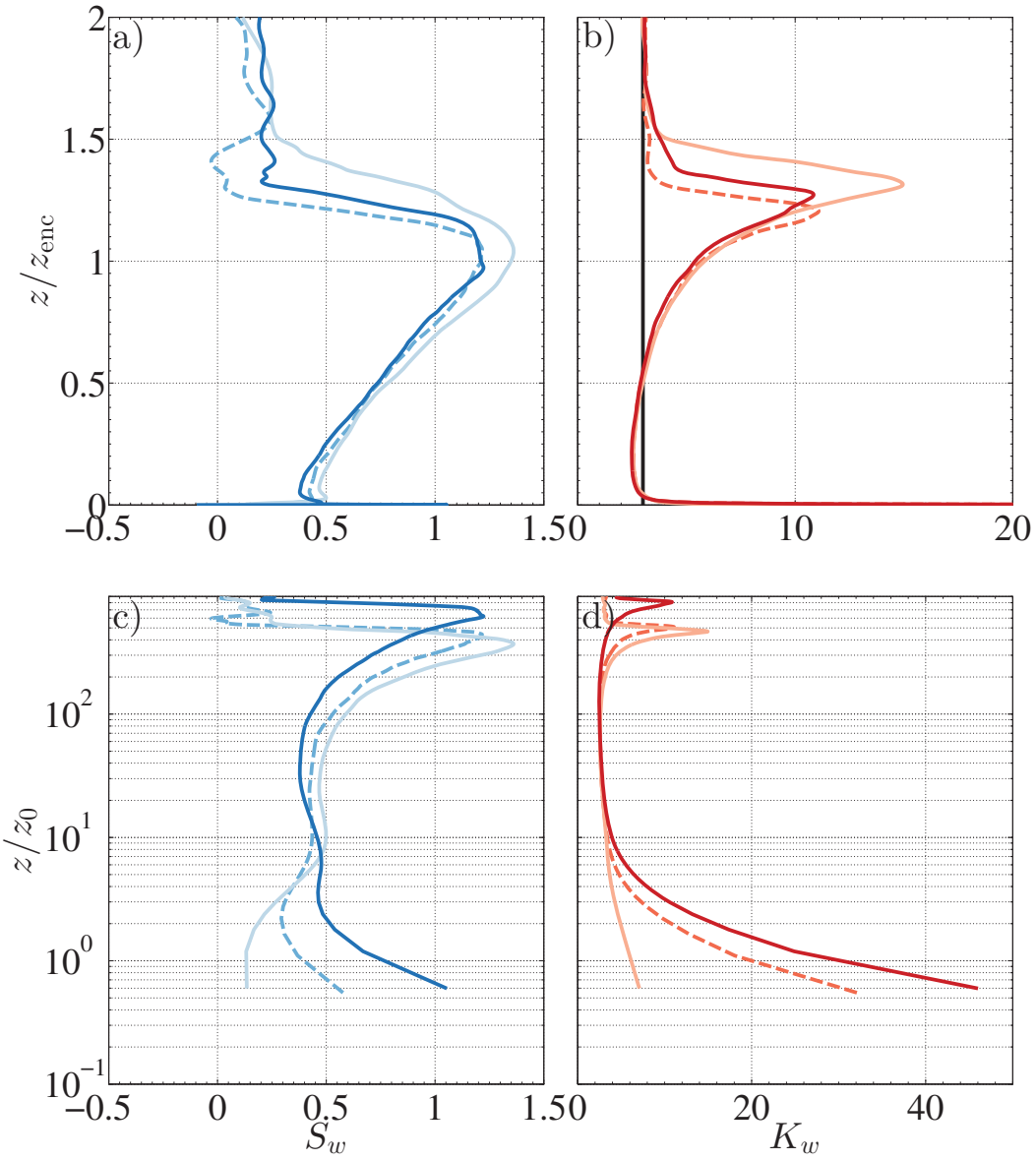

Figure 3.5: a) Vertical profile of the vertical velocity skewness S_w defined in Eq. (3.12) b) Vertical profile of the vertical velocity flatness K_w defined in Eq. (3.13), solid black line corresponds to the flatness value $K_w = 3$ corresponding to a Gaussian profile c) Semi-logarithmic plot of the vertical profile of the vertical velocity skewness S_w against the height in wall units z/z_0, where $z_0 = (\kappa^3/B_0)^{1/4}$ d) Semi-logarithmic plot of the vertical velocity flatness K_w against the height in wall units z/z_0; Solid lines in light to dark colors correspond to Re100 case at $z_{enc}/L_0 = \{10, 18\}$, respectively. Dashed line corresponds to Re040 case at final time $z_{enc}/L_0 = 26$.

indicate Reynolds number independence within the well-mixed layer.

3.5 Turbulence kinetic energy budget

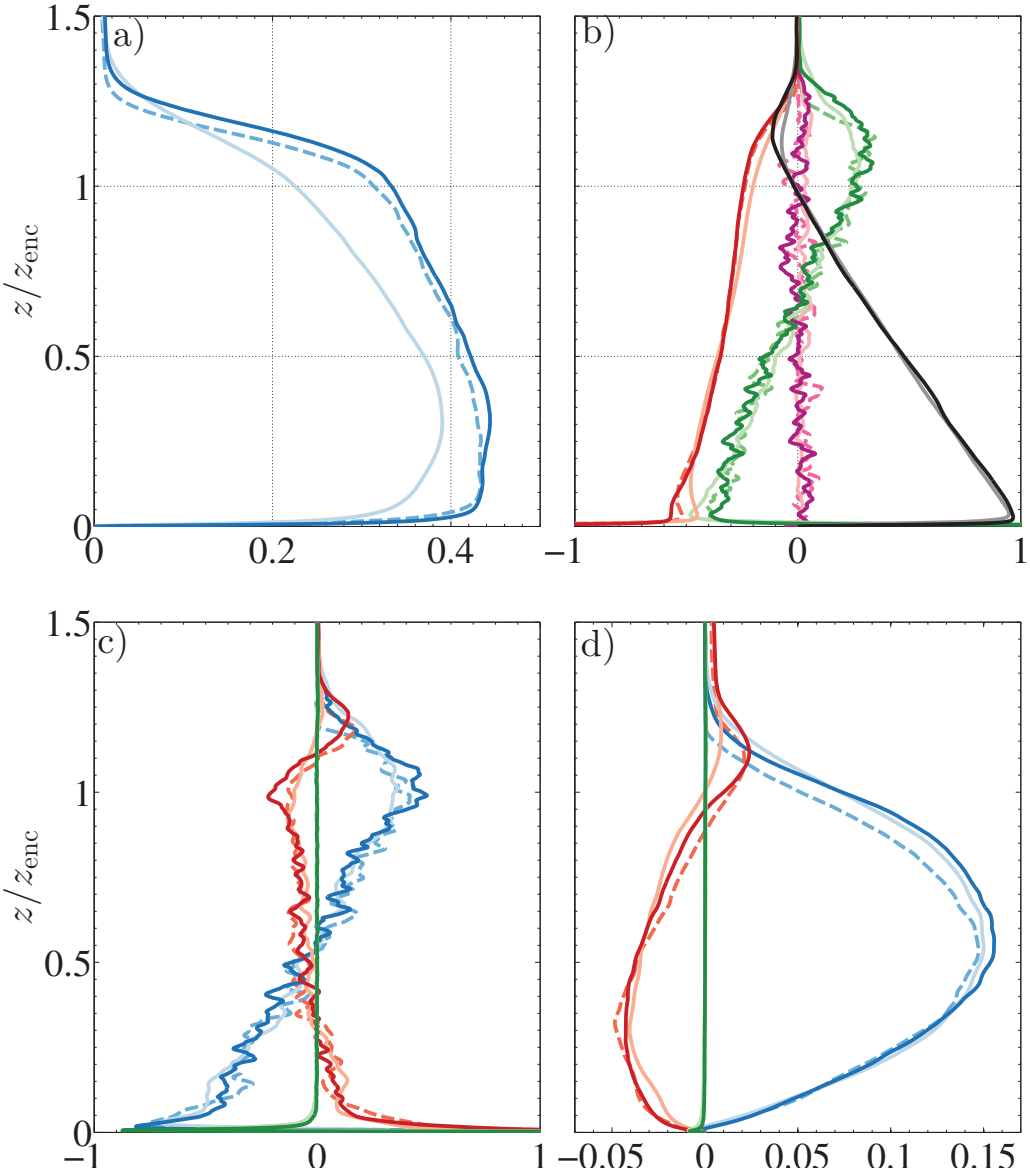

Figure 3.6: a) Vertical profile of turbulence kinetic energy e normalized with w_*^2. b) Vertical profile of TKE budget terms normalized with B_0: $\partial e/\partial t$ (magenta), $\langle b'w' \rangle$ (black), $-\varepsilon$ (red), and $-\partial T/\partial z$ (green). c) Vertical profile of the components of the transport term $-\partial T/\partial z$ defined in Eq. (3.16) (normalized with B_0) : transport due to velocity fluctuations T_u (blue), transport due to pressure fluctuations T_p (red), and molecular transport T_ν (green). d) Vertical profile of the components of the turbulent flux of kinetic energy T (normalized with $B_0 z_{\mathrm{enc}}$) corresponding to the flux due to velocity fluctuations (blue), flux due to pressure fluctuations (red), and flux due to molecular diffusion (green). Solid lines in light to dark colors correspond to Re100 case at $z_{\mathrm{enc}}/L_0 = \{10, 18\}$, respectively. Dashed line corresponds to Re040 case at final time $z_{\mathrm{enc}}/L_0 = 26$.

Turbulence kinetic energy (TKE), defined as

$$e = \langle v_1' v_1' + v_2' v_2' + w'w' \rangle /2 \, , \tag{3.14}$$

is an important quantity for the CBL because it serves as a measure for turbulence intensity and a starting point for many closure attempts. The TKE vertical profile, shown in Fig. 3.6a, is almost constant at the bottom half of the mixed layer but decreases near the entrainment zone due to the less pronounced peak of horizontal velocity fluctuations.

The time evolution of TKE is governed by the TKE budget equation

$$\frac{\partial e}{\partial t} = \langle b'w' \rangle - \varepsilon - \frac{\partial T}{\partial z} \, , \tag{3.15}$$

where $T = \langle w' v_i' v_i' + w'w'w' \rangle /2 + \langle p'w' \rangle - \langle u_i' \tau_{iz}' \rangle$ is the turbulent flux of kinetic energy in the vertical direction ($-\partial T/\partial z$ is referred to as transport term), and $\varepsilon = \left\langle u_{i,j}' \tau_{ij}' \right\rangle$ is the mean viscous dissipation rate (referred to as dissipation term), with the viscous stress tensor being $\tau_{ij} = \nu(u_{i,j} + u_{j,i})$ (the symbol $u_{i,j}$ denotes partial derivative in the direction j for the velocity component u_i).

The behavior of the terms of TKE budget equation is of interest for the development of one-dimensional TKE prognostic models and TKE closure schemes that are used in mesoscale or single-column boundary-layer models. Better parameterizations of the TKE terms is one of the main endeavors in boundary layer modeling since the accuracy of the parameterizations affects the success of higher-order boundary layer schemes. We therefore evaluate the terms of the budget equation using our DNS data, which is free from any kind of turbulence models. We then briefly discuss the behavior of the budget terms and present a few observations that could be interesting for TKE parameterizations, which can be further looked into as a future extension of this study.

Evaluation of the TKE budget terms

Figure 3.6b shows how each of the terms in Eq. (3.15) behave as a function of height. We see that the first term on the right-hand side, the buoyancy flux, is a production term at the mixed layer but becomes a destruction term at the entrainment zone, transforming TKE into potential energy by raising the height of the interface between the mixed layer and the stable free troposphere. As discussed by Winters et al.

(1995), not all of this potential energy is available for transforming back to kinetic energy (reversible) because some of the potential energy is converted to background potential energy by mixing (irreversible). The second term on the right-hand side is viscous dissipation rate of TKE, an irreversible sink that transforms TKE into heat. This heat's magnitude is negligible when the magnitude of the velocity fluctuations is small compared to the speed of sound (Batchelor, 1967) and is therefore not retained in the Boussinesq approximation. The last term on the right-hand side, the transport term, neither creates nor destroys TKE within the whole CBL (since it reduces to zero when integrated, as shown in the next section) and simply transports TKE vertically. For the dry, shear-free case, the transport term is the sole TKE production term within the entrainment zone.

Similar to the variance profiles, the TKE-budget profiles clearly exhibit self-similar behavior at the mixed layer when scaled with $w_*^3/z_{\text{enc}} = B_0$ and z_{enc}, and exhibit the typical structure found in the CBL (Stull, 1988). Reynolds number similarity is also observed, since the profiles of Re040 and Re100 cases at final times agree quite well. Particularly for the profile of viscous dissipation rate, its self-similar behavior within the mixed layer is an indication of the inviscid scaling of viscous dissipation rate. Near the surface, the viscous dissipation rate is still changing because the near-wall region does not necessarily scale with the mixed layer scales (see Chapter 4). As the scale separation between the CBL thickness and the near-wall region thickness increases, the extent of the near-wall region becomes negligible when normalized by the CBL thickness and the region where self-similar behavior is observed extends further down.

On parameterizations of some TKE budget terms

With DNS data at hand, we can study in detail some budget terms that are of particular interest in modeling, such as the TKE transport term. To guide such model development, we breakdown the transport term into its components.

The turbulent transport term has three components:

$$\mathrm{T}_u = -\frac{1}{2}\frac{\partial \left\langle w' v_i' v_i' + w' w' w' \right\rangle}{\partial z},\ \mathrm{T}_p = -\frac{\partial \left\langle p' w' \right\rangle}{\partial z},\ \mathrm{T}_\nu = \frac{\partial \left\langle u_i' \tau_{iz}' \right\rangle}{\partial z}, \tag{3.16}$$

respectively, the transport due to velocity fluctuations, the transport due to pressure fluctuations and transport due to molecular diffusion that is negligible except near

the wall (the diffusive layer) [see Fig. 3.6c]. The first component, T_u, which can be further divided into horizontal and vertical contributions, is the main contributor, particularly its vertical velocity component. Figure 3.6d shows the parabolic shape of the triple velocity correlation term which mainly dictates the linear shape of the transport due to velocity fluctuations T_u.

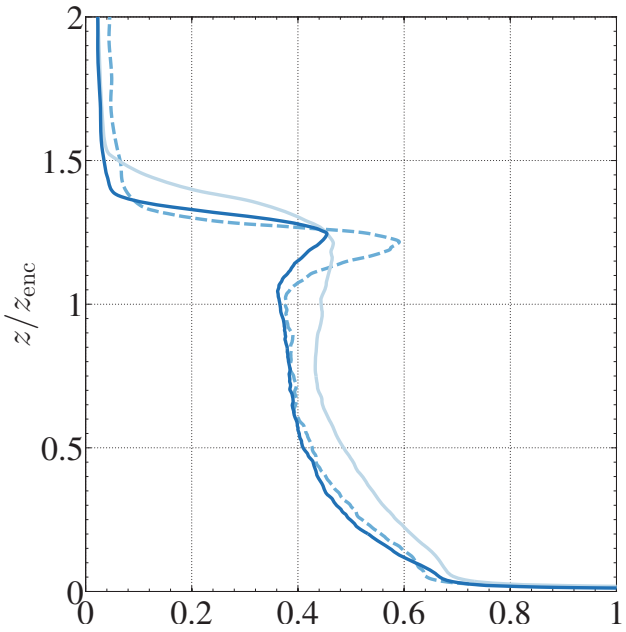

Figure 3.7: Vertical profile of the ratio $\varepsilon/(e^{3/2}/l_\varepsilon)$, where $l_\varepsilon = (0.5 z_i/w_*)\sqrt{e}$. Solid lines in light to dark colors correspond to Re100 case at $z_{\mathrm{enc}}/L_0 = \{10, 18\}$, respectively. Dashed line corresponds to Re040 case at final time $z_{\mathrm{enc}}/L_0 = 26$.

As shown in Witek et al. (2011a), using only an eddy diffusivity approach by modeling the transport term as $\partial/\partial z(-K\partial e/\partial z)$ (where K is the diffusivity coefficient for TKE), does not work because the vertical profile of the TKE is almost constant with height within the CBL (see Figure 3.6a). However, improvement is observed with the addition of a mass flux term that tries to represent the non-local turbulent transport by the large scale convective plumes. In particular, the mass flux representation of the transport leads to a parameterization of the triple velocity correlation as a cubic function of an updraft velocity, which can be roughly thought of as the velocity of the 10% most energetic updrafts, and is solved from an equation that includes a buoyancy source term(see Soares et al., 2004; Witek et al., 2011b). The cubic function of the updraft velocity achieves a similar shape as the triple velocity correlation term in Fig. 3.6d. The improvement brought in by the mass flux parameterization of the turbulent transport term hinges on capturing this general shape of the triple velocity correlation contribution.

On the other hand, the transport due to pressure fluctuations $\langle p'w' \rangle$ is typically taken for granted in usual parameterizations by assuming that it can be combined with– and behaves similarly to T_u. However, we see in Figure 3.6c,d that its behavior is opposite of the turbulent transport in the mixed layer, which slightly shifts the zero-crossing of the total transport and reduces its peaks. Interestingly, the pressure fluctuation contribution T_p becomes a positive contribution at the upper portion of the entrainment zone. The positive contribution is most likely due to the increase in pressure as the thermals push against the stable stratification since such a contribution does not exist in the neutrally-stratified case (not shown). We also point out that the small positive value of the pressure fluctuation flux $\langle p'w' \rangle$ above the entrainment zone (see Fig. 3.6d) is due to the outward radiation of gravity waves within the stably stratified region.

Another term of interest is the rate of viscous dissipation term. With DNS data, we can diagnose a typical parameterization

$$\varepsilon = c_\varepsilon e^{3/2}/l_\varepsilon, \tag{3.17}$$

where c_ε is a coefficient that can vary in time and the length scale $l_\varepsilon = (0.5 z_i/w_*)\sqrt{e}$ is the mixing length formulation proposed by Teixeira and Cheinet (2004). Figure 3.7 shows that the parameterization would only work satisfactorily for the upper half of the CBL but with $c_\varepsilon \simeq 0.4$, which is different from the value used in Witek et al. (2011a) ($c_\varepsilon = 0.6$). The parameterization, Eq. (3.17), when particularly combined with the above-mentioned choice of the mixing length, simply implies an assumption that the normalized viscous dissipation rate $\varepsilon/(w_*^3/z_i)$ is directly proportional to the normalized TKE e/w_*^2. We can deduce from Fig. 3.6a,b, and see more clearly in Fig. 3.7, that this does not necessarily hold even if the proportionality constant c_ε is allowed to vary in time.

3.6 The equilibrium entrainment regime

To show that we are analyzing statistics within a quasi-equilibrium state, we follow Fedorovich et al. (2004b) and perform an integral analysis of the evolution equation for the turbulence kinetic energy, Eq. (3.15). Integrating this transport equation from the surface up to a height z_∞ located far enough into the nonturbulent stably

stratified region yields

$$C_t = C_{bw} - C_\varepsilon - C_T \ , \tag{3.18}$$

where $C_t = w_{*,i}^{-3} \int_0^{z_\infty} (\partial e/\partial t)\, \mathrm{d}z$, and the terms at the right-hand side are

$$C_{bw} = w_{*,i}^{-3} \int_0^{z_\infty} \langle b'w' \rangle \, \mathrm{d}z \ , \qquad C_\varepsilon = w_{*,i}^{-3} \int_0^{z_\infty} \varepsilon \, \mathrm{d}z \tag{3.19}$$

and $C_T = w_{*,i}^{-3} T(z_\infty)$. The convective velocity in the expressions above is $w_{*,i} = (B_0 z_{i,i})^{1/3}$ (Deardorff, 1970). By construction, $C_{bw} = 0.4$. Unlike in Fedorovich et al. (2004b) where a zero-order model framework is assumed and Eq. 3.15 is thus integrated only up to z_i, the upper limit of integration is chosen to be z_∞ such that the transport term $C_T \simeq 0$ and no portion of the EZ, which has a finite thickness, is excluded from the integral analysis.

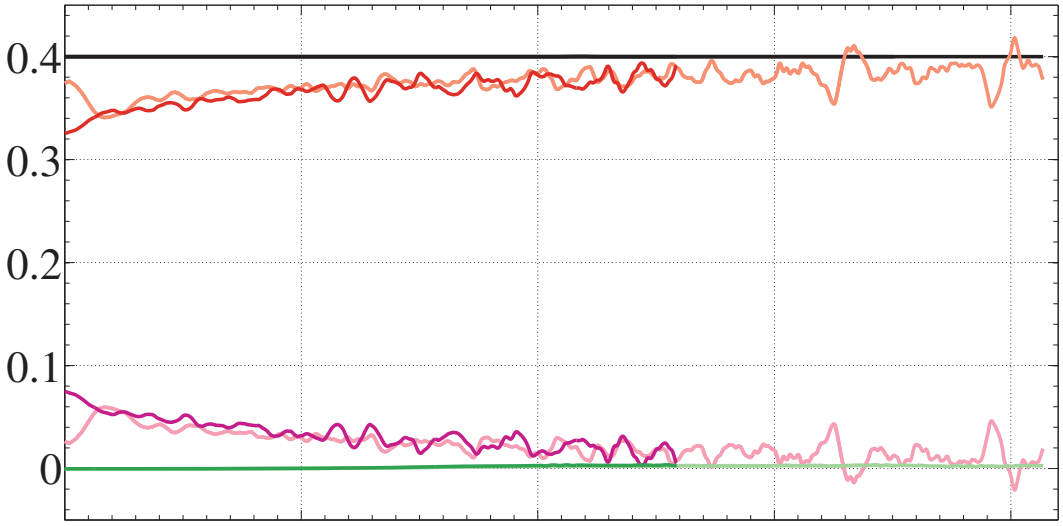

Figure 3.8: Temporal evolution of normalized terms of the integral budget equation of turbulence kinetic energy, Eq. (3.18) showing the dominant balance $C_{bw} \simeq C_\varepsilon$: C_ε (red), C_t (magenta) and C_T (green). $C_{bw} = 0.4$ (black), by definition. Light colors correspond to Re040, dark colors to Re100.

The evolution in time of the terms in Eq. (3.18), shown in Fig. 3.8a, has three main features. First, the collapse of the curves from simulations Re040 and Re100, particularly that of C_ε, indicates the tendency of the production and destruction rates of turbulence kinetic energy towards an inviscid scaling that depends solely on the integral scales $z_{i,i}$ and $w_{*,i}$, i.e., independent of the viscosity. This behavior is another manifestation of Reynolds number similarity (Tennekes and Lumley, 1972; Pope, 2000; Monin and Yaglom, 2007). Second, the negligibly small transport term,

C_T, implies a negligible energy drain due to the upward radiation of inertial gravity waves, in accord with previous findings in similar CBL configurations (Deardorff et al., 1980; Carruthers and Hunt, 1986; Fedorovich et al., 2004b). Finally, the decreasing tendency term C_t implies that beyond $z_{\rm enc}/L_0 \simeq 10$, the dominant balance in Eq. (3.18) is between the terms C_{bw} and C_ε, meaning

$$C_{bw} \simeq C_\varepsilon. \tag{3.20}$$

This balance corresponds to the equilibrium entrainment regime (Fedorovich et al., 2004b). Within this regime, the CBL is in a quasi-steady state in the sense that the time $z_{\rm enc}/w_{\rm e} = N^{-1}(z_{\rm enc}/L_0)^2$ required for a significant change of the CBL thickness is much longer than the turn-over time $z_{\rm enc}/w_* = N^{-1}(z_{\rm enc}/L_0)^{2/3}$ associated with the large-scale convective motions inside the CBL. Indeed, the ratio of these two time scales, $w_*/w_{\rm e} = (z_{\rm enc}/L_0)^{4/3}$, is larger than an order of magnitude for the interval of the normalized CBL thickness $z_{\rm enc}/L_0 \geq 10$ considered in this work.

4 The surface layer

The surface or inner layer of the atmospheric boundary layer (ABL) is roughly defined as the region close to the surface that extends up to 10%-20% of the ABL thickness. This region is characterized by turbulent fluxes and shear stress that are roughly constant with height, and is expected to be the layer where the effects of the outer layer drop out. Sandwiched between the surface and the rest of the ABL, the surface layer essentially links the surface and the atmosphere by regulating fluxes of quantities, such as heat, momentum, and moisture between them.

Introduction

The surface layer fluxes are usually related to corresponding vertical profiles of mean quantities by assuming Monin-Obukhov similarity theory (MOST) (Obukhov, 1946). This theory supposes that the nondimensional vertical gradients of mean quantities are universal functions of the atmospheric stability parameter. For ABLs with sufficiently strong mean winds, widely used flux calculation techniques based on MOST such as the Businger-Dyer profiles work satisfactorily, but then break down for strongly convective cases with vanishingly small winds. For most purposes of atmospheric modeling and field data analysis, the stability regime covered by such techniques were generally deemed adequate since ABLs with vanishingly small winds are extreme cases and the asymptotic limit of pure shear-free ABLs is virtually

unattainable in the ABL. However, recognition of the importance and considerable frequency of the strongly convective case in warm pools in the sea (see, e.g., Miller et al., 1992) has demanded for more generalized models that can handle vanishingly small winds in a consistent and robust manner.

To accommodate the strongly convective cases, flux parameterizations are generally extended by incorporating the MOST prediction in the asymptotic limit of vanishing mean wind (see, e.g., Akylas and Tombrou, 2005; Zhao et al., 2013). This limit, called the free convection limit, yields the classical similarity scalings, also known as Priestley scalings, wherein statistics scale as certain power laws with respect to the height z: the mean buoyancy gradient $\propto z^{-4/3}$, the r.m.s. of (vertical) velocity fluctuations $\propto z^{1/3}$, and the r.m.s. of buoyancy fluctuations $\propto z^{-1/3}$ (Prandtl, 1932; Obukhov, 1946; Priestley, 1954).

For atmospheric data, the validity of classical similarity theory remains questionable because only a few statistics seem to exhibit the theoretical scalings. For example, the Kansas field experiments seem to exhibit the 1/3 and -1/3 laws for the fluctuation of vertical velocity and buoyancy, respectively, even for remarkably small atmospheric stability values (Wyngaard et al., 1971) but do not support the -4/3 law for the mean buoyancy gradient and the 1/3 law for the horizontal velocity fluctuation. Instead, -3/2 power law (Businger et al., 1971) for the mean buoyancy gradient and a scaling of the horizontal velocity fluctuations with the convective velocity scale (Panofsky et al., 1977) have been reported. The Minnesota field experiment shows results similar to the Kansas field experiment except that the Minnesota data do not strongly support the -1/3 power law for the buoyancy fluctuations (Kaimal et al., 1976). Support for the classical similarity scalings is then further weakened by the scatter in the data that is enough to make agreement with other scalings also possible, and by the extrapolation of sheared convection data to the shear-free limit, which is unavoidable due to the limited stability range covered by measurements and the rarity of pure free convection observations.

In laboratory experiments where pure free convection is attainable, support for the classical similarity scalings is much less convincing. Similar to atmospheric measurements, the -4/3 law for the mean buoyancy gradient is generally not observed in the laboratory, instead -2 and -3/2 power laws have been reported (see Adrian et al., 1986, for a review). Moreover, the 1/3 and -1/3 power laws for the r.m.s. of vertical velocity and buoyancy fluctuations, respectively, are generally unsupported in the laboratory. Instead other scalings, such as logarithmic scaling with z for the

vertical velocity r.m.s. and -1/2 for the buoyancy r.m.s., to name a few, have been reported (Adrian, 1996). These deviations are clearly observed in the laboratory because the scatter in data is less; however, findings in the laboratory still cannot convincingly contradict classical similarity scalings because low Reynolds numbers effects may be significant.

Kraichnan (1962), regarding deviations in laboratory data, and later Businger (1973), regarding deviations in atmospheric data, proposed similar mechanisms to explain why the conditions for free convection scaling at the surface layer are never completely reached. The general idea is that even in the absence of mean wind, local shear effects within the convective cells are believed to be produced by 'convective wind' gusts caused by the large scale convective motions that penetrate into the surface. These gusts create a 'minimum friction velocity' that is believed to scale with the convective velocity w_*. Such an idea introduces outer scales like the CBL thickness into the set of characteristic scales, which then violates the assumptions of MOST. Still, the 'minimum friction velocity' is usually incorporated into parameterizations to extend the MOST framework by treating free convection as a particular case of forced convection (Sykes et al., 1993; Beljaars, 1994). Improvements to surface layer schemes have been claimed with the inclusion of a 'minimum friction velocity'. However, the underlying hypothesis and its resulting surface layer scalings have not been properly confirmed.

Banking on previous indications of outer layer effects on the inner layer, we further ask whether stratification would affect the inner layer dynamics, an effect that is so far unstudied. Switching off the presence of the background buoyancy stratification N^2 allows the boundary layer to grow faster and develop large scale motions that are vertically unhindered, unlike in the CBL. To analyze whether the presence or absence of stratification would affect the inner layer, we compare the surface layer statistics of our linearly stratified CBL ($N^2 > 0$) to the surface layer statistics of a neutrally-stratified free convection 'heated plate' case ($N^2 = 0$) also from DNS (Mellado, 2012), which corresponds to the asymptotic limit of the CBL for vanishingly weak stratification. The heated plate case is comparable to the state of the CBL during an early regime wherein the turbulent boundary layer is shallow enough to behave essentially as if it were developing in neutral conditions (e.g. morning transition when residual layer is broken down by the turbulent convective motions). As the CBL continues to grow, the CBL state enters a regime where the CBL feels N^2 more significantly, which then diminishes the CBL growth rate with respect to that of the early regime, and further evolves into its fully-developed state (see Appendix A).

Comparing the two cases can therefore be interpreted as a study on the effect of the CBL state on the inner layer statistics.

4.1 Characteristic scales

We will use two different sets of characteristic scales for discussing the results. The inner scales are constructed with B_0 and z_0, where z_0 indicates either the roughness length or the diffusion length, depending on the surface properties (Garratt, 1992). The corresponding velocity and buoyancy scales are $w_0 = (B_0 z_0)^{1/3}$ and $b_0 = (B_0^2/z_0)^{1/3}$, respectively. For a smooth wall and in the case $\mathrm{Pr} = \nu/\kappa = 1$ as considered in this work, the diffusion length is given by

$$z_0 = (\kappa^3/B_0)^{1/4}, \tag{4.1}$$

and the remaining inner scales (wall diffusion units) are

$$w_0 = (B_0\kappa)^{1/4},\ b_0 = (B_0^3/\kappa)^{1/4} \tag{4.2}$$

(Townsend, 1959). Variables normalized with the inner scales will be denoted with a superscript "+", e.g.,

$$z^+ = z/z_0\ . \tag{4.3}$$

The outer scales are constructed with B_0 and h, where h is a measure of the boundary layer thickness, to be defined later. The corresponding velocity and buoyancy scales are the convective scales, $w_* = (B_0 h)^{1/3}$ and $b_* = (B_0^2/h)^{1/3}$, respectively (Deardorff, 1970) (see Chapter 3).

As discussed in Chapter 2, the control parameters are $\{\nu,\ \kappa,\ B_0,\ N\}$ and the independent variables are $\{z, t\}$. For both cases, the Prandtl number $\nu/\kappa = 1$. The only difference between the CBL and the heated plate case is in the value of the parameter N: $N \neq 0$ for the CBL and $N = 0$ for the heated plate. Choosing κ and B_0 to nondimensionalize the problem, the statistics can be expressed as a function of the set of nondimensional variables $\{z^+,\ h^+,\ h/L_0\}$, where the dependence on the time has been expressed in terms of $h^+(t^+)$, i.e., the scale separation between the boundary layer height $h(t)$ and the diffusion length z_0. This ratio can alternatively be interpreted in terms of the convective Reynolds number (see Eq. 2.10) particularly in the form $\mathrm{Re}_* = hw_*/\nu = (h^+)^{4/3}$.

Case	Grid	Domain size	h^+	Re_*	Re_t	Ra_*	δ_b^+
$N^2 \neq 0$	$5120^2 \times 840$	$7630^2 \times 2010$	623	5320	2860	1.0×10^9	4.17
$N^2 = 0$	$5120^2 \times 1280$	$7630^2 \times 2666$	620	5287	1740	1.0×10^9	4.20
			1034	10320	3656	4.7×10^9	4.33

Table 4.1: Simulation grid, domain size in wall units and properties at different states of development as indicated by the boundary layer height $h^+ = h/z_0$, where z_0 is defined as $z_0 = (\kappa^3/B_0)^{1/4}$ (Townsend, 1959). The convective Reynolds number $\mathrm{Re}_* = hw_*/\nu = (h^+)^{4/3}$ is defined based on the convective velocity $w_* = (B_0 h)^{1/3}$. The turbulent Reynolds number $\mathrm{Re}_\mathrm{t} = e^2/(\varepsilon\nu)$, where e is the turbulence kinetic energy and ε its viscous dissipation rate, is the maximum value across the boundary layer.

Both the CBL and heated plate exhibit a quasi-steady regime after a certain interval of time, in the sense that the integral time scale of the turbulent fluctuations is much shorter than the characteristic time necessary for the evolution of the vertical profiles (Fedorovich et al., 2004b; Mellado, 2012). We are interested in this quasi-steady regime, therefore h^+ can be considered as a control parameter instead of an independent variable. For the CBL, we have shown that the quasi-steady regime occurs when the boundary layer height h becomes about an order of magnitude larger than L_0 (see Chapter 3 section 3.6). Within this regime, self-similar behavior of the outer layer statistics is observed regardless of the increasing value of h/L_0. We therefore hypothesize that the particular value of h/L_0 is irrelevant in the discussion that follows, except for the crucial fact that it is non-zero for the CBL ($N^2 \neq 0$) and zero for the heated plate ($N^2 = 0$). This difference leads to a different vertical structure of the boundary layer, as shown later. In sum, the statistics can be expressed as a function of $\{z^+, h^+\}$ and we analyze how these functions depend on the conditions $N^2 \neq 0$ and $N^2 = 0$.

4.2 Vertical structure in free convection

We roughly follow the vertical structure definition in free convection identified in Mellado (2012) based on adapting conventions in shear-driven flows to the free convection case.

The inner layer is usually identified based on the quasi-steady behavior of some statistics and is estimated to be a certain fraction α of the outer layer thickness h, namely, αh. As in Mellado (2012), we base the definition of the inner layer and its sublayers on the total buoyancy flux $B = \langle b'w' \rangle - \kappa(\partial\langle b \rangle/\partial z)$, shown in Fig. 4.1. The

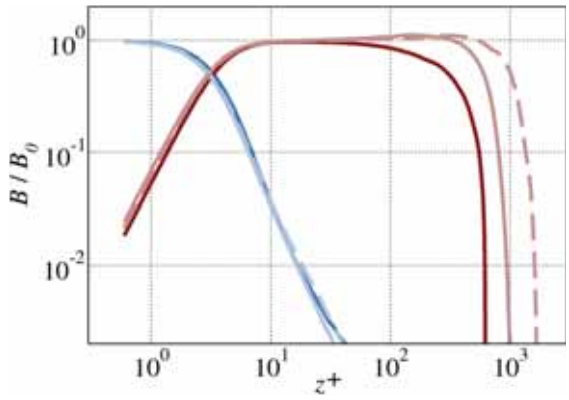

Figure 4.1: Vertical profile of the molecular (blue) and turbulent (red) contributions to the total buoyancy flux $B = \langle b'w' \rangle - \kappa(\partial\langle b \rangle/\partial z)$ plotted in wall diffusive units. Solid lines correspond to $h^+ \simeq 620$, and dashed lines to $h^+ \simeq 1034$ (only available for neutral case). Dark colors indicate the stably stratified case and light colors the neutrally stratified case.

inner layer includes the diffusive wall region $0 < z^+ \leq 10$, where molecular effects are non-negligible. Sublayers of the diffusive wall region are further defined based on the relative contributions of the molecular and turbulent buoyancy flux to the total buoyancy flux B. These sublayers are: the diffusive sublayer $z^+ \leq 1$, where the turbulent buoyancy flux contribution is roughly below 10%, and the buffer layer $1 \leq z^+ \leq 10$, where the turbulent buoyancy flux increases rapidly. At a height equal to the buoyancy gradient thickness

$$\delta_b = -(\Delta b)_s / \partial_z \langle b \rangle|_{z=0} \ , \tag{4.4}$$

($(\Delta b)_s$ is the buoyancy difference, to be defined later) both molecular and turbulent contributions to the total buoyancy flux B are comparable to each other. For the range of Rayleigh numbers achieved in the simulations, δ_b is slightly larger than four wall units (see Table 4.1). The order of one values of the normalized variables in the diffusive wall region and the independence of the profiles from h^+, confirm that the inner scaling of Townsend is appropriate for the diffusive wall region (see also Fig. 4.4).

Beyond $z^+ > 10$, the molecular buoyancy flux contribution to the total is less than 4% and is therefore negligible. This region is considered to mark the beginning of the outer layer, where molecular diffusivity drops out of the analysis and z/h remains as the only independent variable.

In contrast to the previous definitions, defining the upper limit of the inner layer's extent in the CBL is actually less straightforward. In Mellado (2012), the inner

layer is identified based on the quasi-steady behavior of the total buoyancy flux, and its thickness is defined as the extent of the region of approximately constant buoyancy flux, an extent of $\sim 0.4h$ as identified by Mellado (2012). However, for the CBL, a region of constant buoyancy flux does not exist because the total buoyancy flux is linearly decreasing. The inner layer in the CBL is therefore identified as a region where the fluxes are approximately constant, meaning they are not changing too rapidly with height. Garratt (1992) defines this region as the extent where the buoyancy flux is up to $\geq 0.9B_0$, which we observe in our CBL as equivalent to $\sim 0.1h$, although the choice of 90% of the surface buoyancy flux is somewhat arbitrary. The resulting region is clearly smaller than in the plate. In this study, we claim that an inner layer extent of $0.2h$ for both the CBL and the heated plate is a fair alternative definition that derives its justification on an interesting property that we observe in the co-spectra of the buoyancy and the vertical velocity, which we discuss later. We observe that such a definition corresponds to a region in the CBL where the turbulent buoyancy flux is at most $0.8B_0$.

Where the inner- and the outer layer overlap, the statistics presumably depend only on the parameters that are common to both the inner and outer layer, namely, $\{B_0, z\}$. These parameters are used to construct the free convection scales (see Prandtl, 1932; Obukhov, 1946; Priestley, 1954; Wyngaard et al., 1971) and the overlap region is where classical similarity theory proposes the power law scalings that were mentioned in the introduction. We will look into the statistics in this overlap region later on to see whether classical similarity predictions for the vertical profiles hold and whether the stratification affects the behavior of these profiles.

4.3 Differences between the outer layer of the CBL and the 'heated plate'

One main difference that the presence or absence of stratification brings about is the presence or absence of the capping action on the rising buoyant thermals. Whether these vertical motions are hindered or not have effects on the CBL and heated plate that can already be identified visually from Figure 4.2. Due to the overlying stably stratified layer in the CBL, sharp gradients can be seen at the top of the boundary layer as the rising thermals impact on the stable region, whereas in the heated plate where the thermals are free to rise, the top of the boundary layer ends up being characterized by largely intermittent regions and by engulfment of nonturbulent

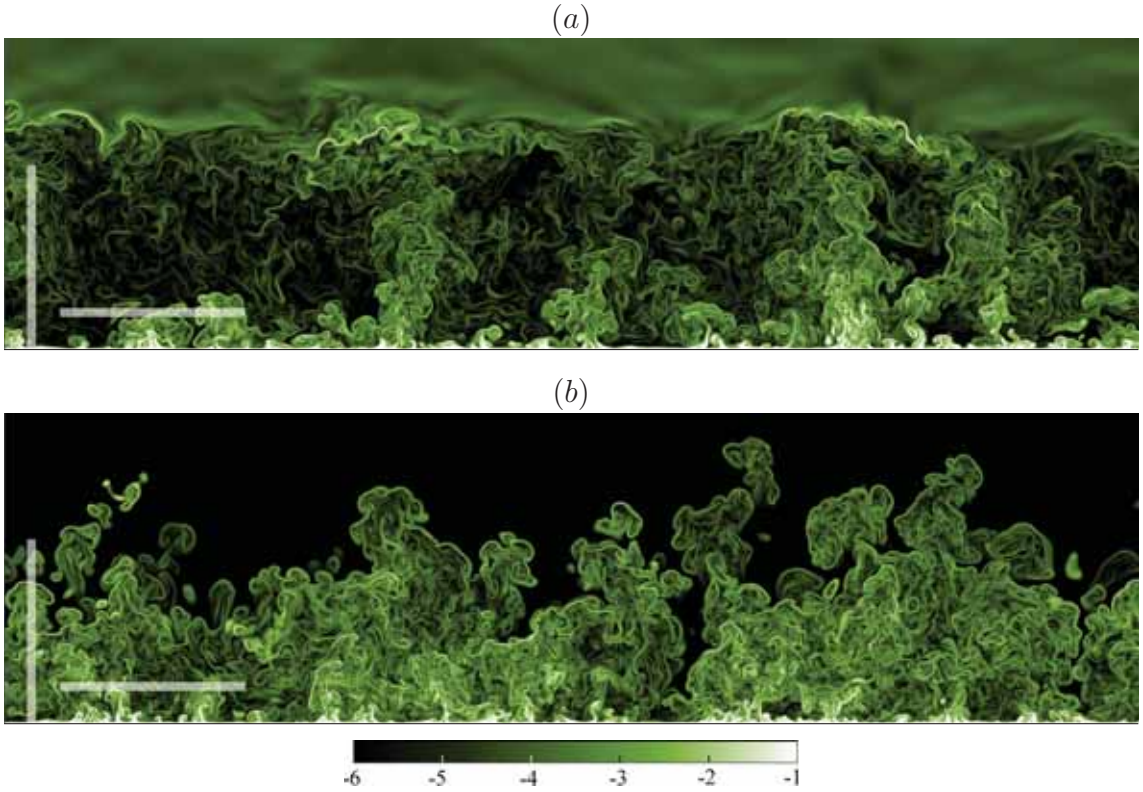

Figure 4.2: Vertical cross-section showing the logarithm of the scalar dissipation rate $\log_{10} \epsilon_b^+$ at $h^+ \simeq 620$: (a) stably stratified case, (b) neutrally stratified case. The vertical white bar in the bottom-left corner indicates the boundary layer height h. The horizontal white bar is located at $0.2h$ and extends a distance h in the horizontal. Only 1/2 of the domain is shown.

fluid. The capping effect of stable stratification further affects the structure of the large convective motions. In the CBL, the updrafts are more well-defined and tower-like, whereas those in the heated plate are less-defined, wider, and less clustered together. Consequently, the downdraft regions are also more distinct in the CBL and appear as regions of relatively weaker turbulence, whereas in the heated plate case, downdraft regions are more difficult to identify visually due to the spreading of updrafts and the large scale engulfment of nonturbulent fluid, which increases the global intermittency of the flow. The aspect ratio of the large convective motions are also visibly different: in the CBL the horizontal extent of the large convective cells are wider than that in the heated plate.

In order to quantitatively compare between the outer layer characteristics of the CBL and the heated plate, we need definitions of the boundary layer thickness that render both problems comparable. For the CBL, we saw in Chapter 3 that there are different possible definitions but all of them basically mark the mean vertical location of the entrainment zone. But unlike the CBL, the heated plate neither has a clearly defined entrainment zone nor a region of negative buoyancy flux. We therefore use the integral definition for the heated plate and the zero-crossing definition $z_{i,0}$ for the CBL to exclude the region of negative buoyancy flux,

$$h = \begin{cases} B_0^{-1} \int_0^\infty \langle b'w' \rangle \mathrm{d}z \ , & \text{in the neutrally stratified case } N^2 = 0 \ , \\ \{z : B(z) = 0\} \ , & \text{in the stably stratified case } N^2 \neq 0 \ , \end{cases} \tag{4.5}$$

where B is the total buoyancy flux. Note that unlike the CBL, the heated plate case does not have a factor 2.5 for the integral definition. Such a factor is unnecessary since the shape of the vertical profile of the heated plate's buoyancy flux is approximately rectangular, in contrast to the triangular shape in the CBL, as shown in Figure 4.3a. The quasi-steady regime in each configuration is characterized by corresponding growth rate laws

$$h \simeq \begin{cases} \left[B_0 (t/3)^3\right]^{1/2} \ , & \text{in the heated plate } N^2 = 0 \ , \\ \left[B_0 (2t/N^2)\right]^{1/2} \ , & \text{in the CBL } N^2 \neq 0 \ , \end{cases} \tag{4.6}$$

(see, e.g., Zilitinkevich, 1991; Fedorovich et al., 2004b; Mellado, 2012). Figure 4.3b shows that the both the CBL and the heated plate are in this quasi-steady regime beyond $h^+ \simeq 200$.

The aforementioned choice of boundary layer heights makes sense since it yields comparable vertical profiles of the r.m.s. of the fluctuations of horizontal and ver-

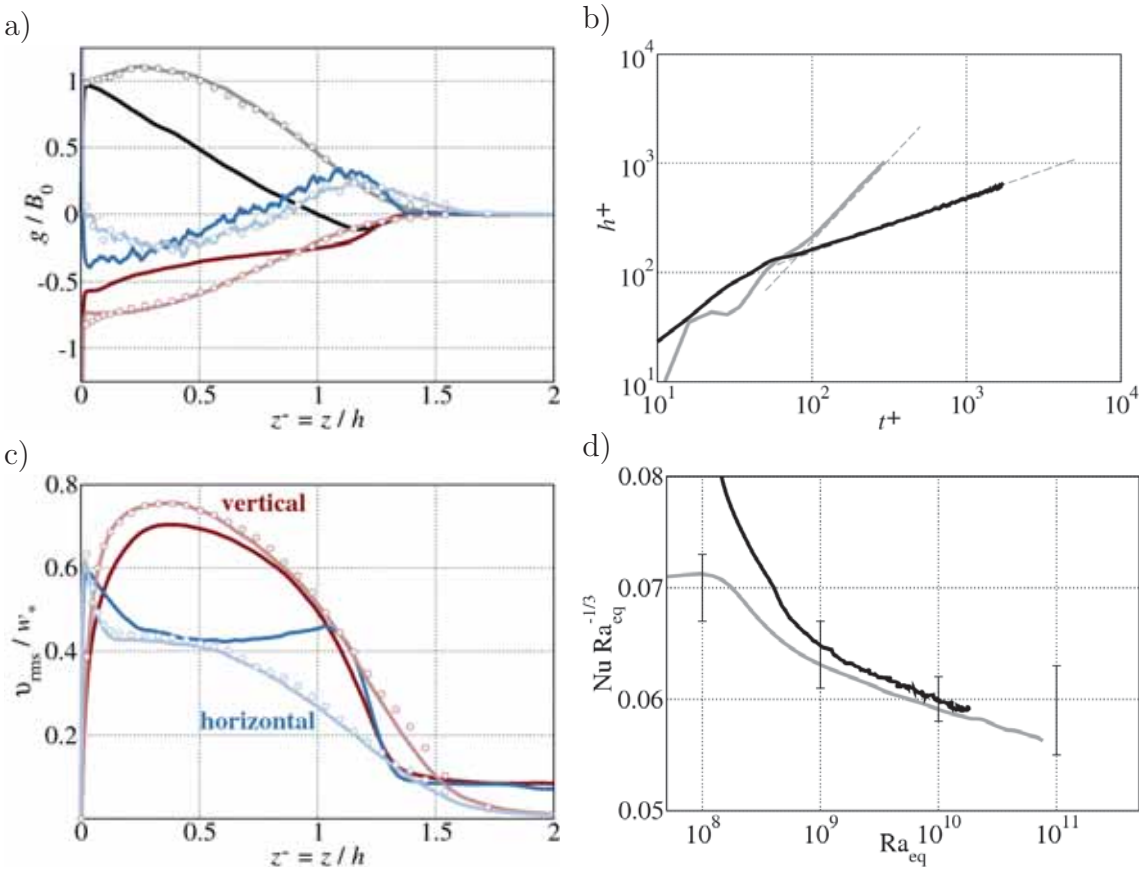

Figure 4.3: a) Vertical profiles of the buoyancy flux $\langle b'w' \rangle$ (black), turbulent transport $-\partial T/\partial z$ (blue) and viscous dissipation rate $-\varepsilon$ (red). b) Temporal evolution of boundary layer heights h, Eq. (4.5). Dashed lines indicate the corresponding scaling laws describing the quasi-steady regimes, Eq. (4.6). c) Vertical profiles of the r.m.s. of the velocity fluctuations normalized with outer scales. d) Compensated Nusselt number as a function of the Rayleigh number. The vertical bars indicate the interval of data measurement extracted from figure 2 in the review paper Chillà and Schumacher (2012). Solid lines correspond to $h^+ \simeq 620$, and circles to $h^+ = 1034$ (only available for neutrally stratified case). Dark colors indicate the stably stratified case and light colors the neutrally stratified case.

tical velocity shown in Figure 4.3c. Further differences between the CBL and the heated plate can now be quantitatively identified. At the top of the CBL, there are strong horizontal velocity fluctuations due to the deflection of thermals by the stable stratification, whereas such a peak is absent in the heated plate case. As for the vertical velocity fluctuation, the magnitude of the peak is smaller in the CBL, most likely due to hampering pressure effects of the stable stratification. Otherwise, the bulk profiles of the r.m.s. of velocity fluctuations are similar. Despite this similarity, the turbulent Reynolds number $\mathrm{Re_t} = e^2/(\nu\varepsilon)$ is larger in the CBL by about 50% at the same boundary layer height $h^+ \simeq 620$ (equivalently, the Taylor-based Reynolds number $\mathrm{Re}_\lambda = \sqrt{(20/3)\mathrm{Re_t}}$ is different by about a factor of 30%). The main difference lies in the dissipation rate, which is larger in the heated plate (see Fig. 4.3a), the underlying reason is mentioned later.

We also show that the CBL and the heated plate case can be compared with Rayleigh-Benárd convection, when both are interpreted as half a Benárd convection cell (Mellado, 2012). This interpretation means that h and $(\Delta b)_s$ are, respectively, half the height and half the buoyancy difference between the two plates in Rayleigh-Benárd convection (Adrian et al., 1986; Mellado, 2012)

$$(\Delta b)_s = \begin{cases} \langle b \rangle(0,t) \,, & \text{in the heated plate } N^2 = 0 \,, \\ \langle b \rangle(0,t) - N^2 h \,, & \text{in the CBL } N^2 \neq 0 \,. \end{cases} \tag{4.7}$$

The buoyancy term $N^2 h$ is the encroachment buoyancy (see Chapter 3 section 3.2). Such an interpretation introduces a factor of 16 in the equivalent Rayleigh number defined as $\mathrm{Ra_{eq}} = 16\mathrm{Ra}_*$, where

$$\mathrm{Ra}_* = \frac{h^3 (\Delta b)_s}{\nu\kappa} = (h^+)^3 (\Delta b)_s^+ \,. \tag{4.8}$$

The Nusselt number (where the condition $\mathrm{Pr} = 1$ has been used)

$$\mathrm{Nu} = \frac{B_0}{\kappa (\Delta b)_s / h} = \frac{h^+}{(\Delta b)_s^+} \,, \qquad , \tag{4.9}$$

is plotted in Figure 4.3d as a function of the equivalent Rayleigh number in the compensated form $\mathrm{Nu}\,\mathrm{Ra_{eq}^{-1/3}} = [2(\Delta b)_s^+]^{-4/3}$, which shows that data from both the neutrally and the stably stratified cases agree with the data from Rayleigh-Benárd convection beyond $\mathrm{Ra_{eq}} \simeq 5 \times 10^8$, once both boundary layer systems are in their corresponding quasi-steady regime (i.e., beyond $h^+ \simeq 200$). This result further

supports our choice of boundary layer height definitions, Eq. (4.5).

4.4 Effects of the outer layer on the surface layer statistics

4.4.1 Vertical profiles

For both the CBL and the heated plate, the r.m.s. of horizontal velocity fluctuations in the inner layer is varying in time (see Fig. 4.4a) and the maximum r.m.s. value seems to scale with the convective velocity (see Fig. 4.6a). This observation agrees with the findings of Panofsky et al. (1977) in atmospheric flows at much larger Rayleigh numbers and also implies that the outer layer indeed penetrates down to the inner layer. As for the vertical velocity and buoyancy in Figure 4.4b-d, we see deviations from classical similarity theory and differences between the CBL and heated plate statistics. Although we cannot strongly propose the observed scalings as alternatives due to the limited extent of the overlap region $10 < z^+ < 0.2h^+$ and possible Reynolds number effects, the difference in behavior between the CBL and the heated plate despite the Reynolds number being similar suggests a dependence of surface layer statistics on N, and therefore on the outer scales, which proves the assumptions behind classical similarity theory as wrong. We look into these differences in detail in the following.

In the CBL, the mean buoyancy gradient $\partial\langle b\rangle/\partial z$ seems to be tangential to the $(z^+)^{-2}$ line for a short extent that slightly goes beyond the diffusive wall region, but then the exhibited power law changes to $(z^+)^{-4/3}$ slightly further into the overlap region and even extends into the outer layer. The scaling $\partial\langle b\rangle^+/\partial z^+ = (\partial\langle b\rangle/\partial z)(z_0/b_0) \propto (z^+)^{-4/3}$ is in agreement with classical similarity theory. This observation is slightly surprising since the $-4/3$ power law is never achieved in the atmosphere, and rarely in the laboratory. On the other hand, the r.m.s. of the buoyancy fluctuations is clearly better described by $b^+_{\mathrm{rms}} \propto (z^+)^{-1/2}$, and that of the vertical velocity fluctuations by $w^+_{\mathrm{rms}} \propto \log(z^+)$. The observed scalings for the r.m.s. of fluctuations seem to support the theoretical scalings proposed by Adrian (1996), derived from an extension of Castaing et al. (1989) theory, which proposes an alternative heat transfer relation, namely, $\mathrm{Nu} \propto \mathrm{Ra}^{2/7}$. However, neither this alternative relation nor a key assumption of Adrian (1996) are supported by our data. We will

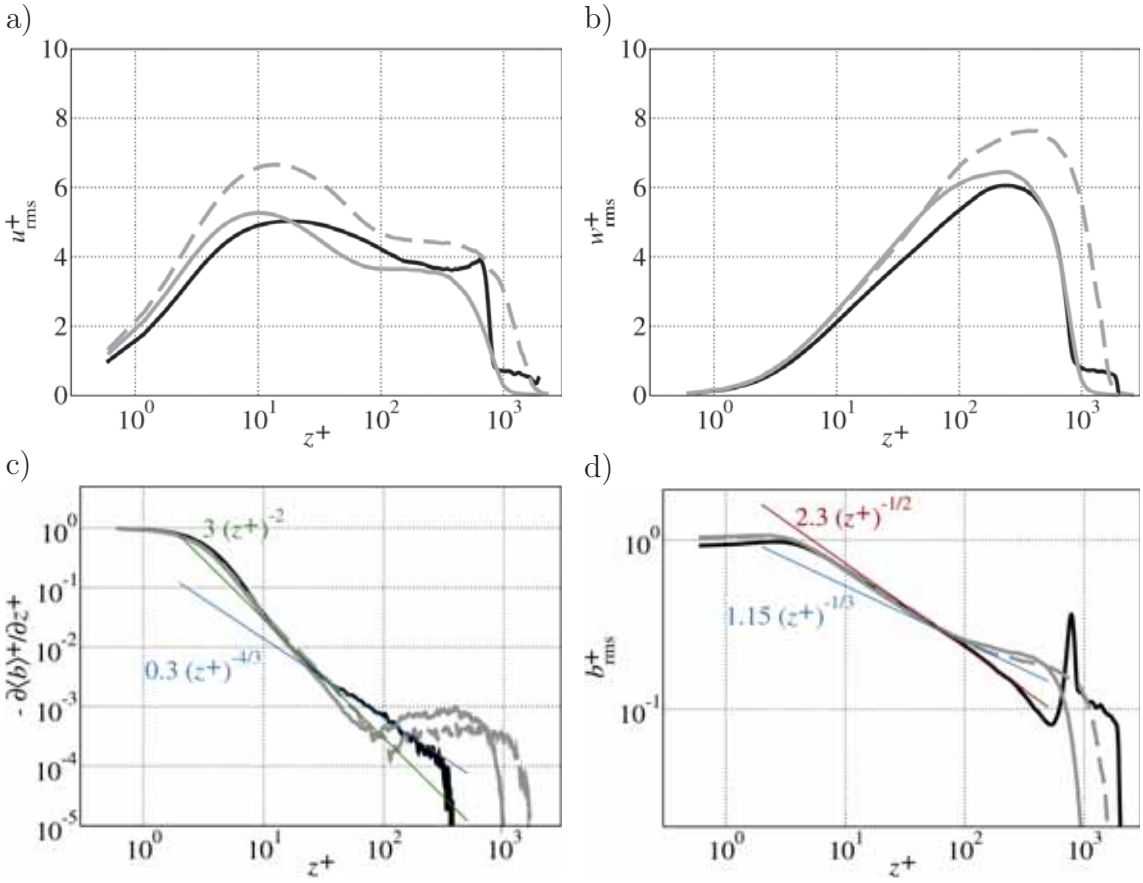

Figure 4.4: Vertical profiles of the horizontal (one component), in panel a, and vertical, in panel b, velocity r.m.s., plotted in wall diffusive units. Vertical profiles of the mean buoyancy gradient, in panel c, and buoyancy r.m.s, in panel d, plotted in wall diffusive units. Solid lines correspond to $h^+ \simeq 620$, and dashed lines to $h^+ = 1034$ (only available for neutral case). Dark colors indicate the stably stratified case and light colors the neutral case.

briefly discuss why this key assumption does not hold using the spectral analysis.

In the heated plate case, w^+_{rms} also varies logarithmically with height, $w^+_{\text{rms}} \propto \log(z^+)$ but with a different proportionality constant, likely due to the difference in the level of turbulence intensity of the flows (Adrian, 1996). However, the buoyancy profiles exhibit differences in the observed power laws from those in the CBL, namely, $\partial\langle b\rangle^+/\partial z^+ \propto (z^+)^{-2}$ and $b^+_{\text{rms}} \propto (z^+)^{-3/2}$. In particular, the mean buoyancy gradient in the heated plate maintains the -2 power law deeper into the overlap region, unlike the CBL. We note that the -2 power law for the mean buoyancy gradient was predicted by Malkus' theory for turbulent convection (Malkus, 1954). As for the b_{rms}, we observe that it behaves as $(z^+)^{-1/2}$ up to roughly $z^+ \simeq 10^2$, similar to the CBL but becomes tangentially close to $(z^+)^{-1/3}$, which then makes $b^+_{\text{rms}} \propto (z^+)^{-3/2}$ within the whole overlap region seem more appropriate. To decide which power law better represents the behavior of the profiles in the overlap region is difficult since one can argue that the inner layer extent of the heated plate case could actually be larger ($\sim 0.4h$) (Mellado, 2012) and it is in this region where we see the variation. A thicker overlap region is then required for any claims to be conclusive. An implication of the observed dependence of b_{rms} on the presence or absence of stratification of the fluid aloft is that the observed scatter of the atmospheric measurements of b_{rms} between $z^{-1/2}$ and $z^{-1/3}$ could be partly due to the different states of the development of the CBLs in which the measurements were obtained, and not only due to departures from free convection conditions caused by mean horizontal winds.

4.4.2 Spectral analysis

By studying the vertical structure of the radial spectra of buoyancy and velocity components, we support the hypothesis that the effect of the presence or absence of stratification, which induces differences between the CBL and heated plate inner layer statistics, manifests mainly as a difference in how organized are the large scale convective motions.

Figure 4.5a-c shows the co-spectra of the buoyancy and vertical velocity for the CBL ($h^+ \simeq 623$) and the heated plate case ($h^+ \simeq 620, 1034$). The CBL's co-spectra shows that the dominant wavelengths contributing to the turbulent buoyancy flux $\langle b'w'\rangle$ grows approximately like $\lambda = 5z$ (diagonal dashed line Fig. 4.5a). We interpret the approximately linear growth of the dominant wavelength as a signature of the coalescence of small active plumes into fewer but larger plumes that are farther apart

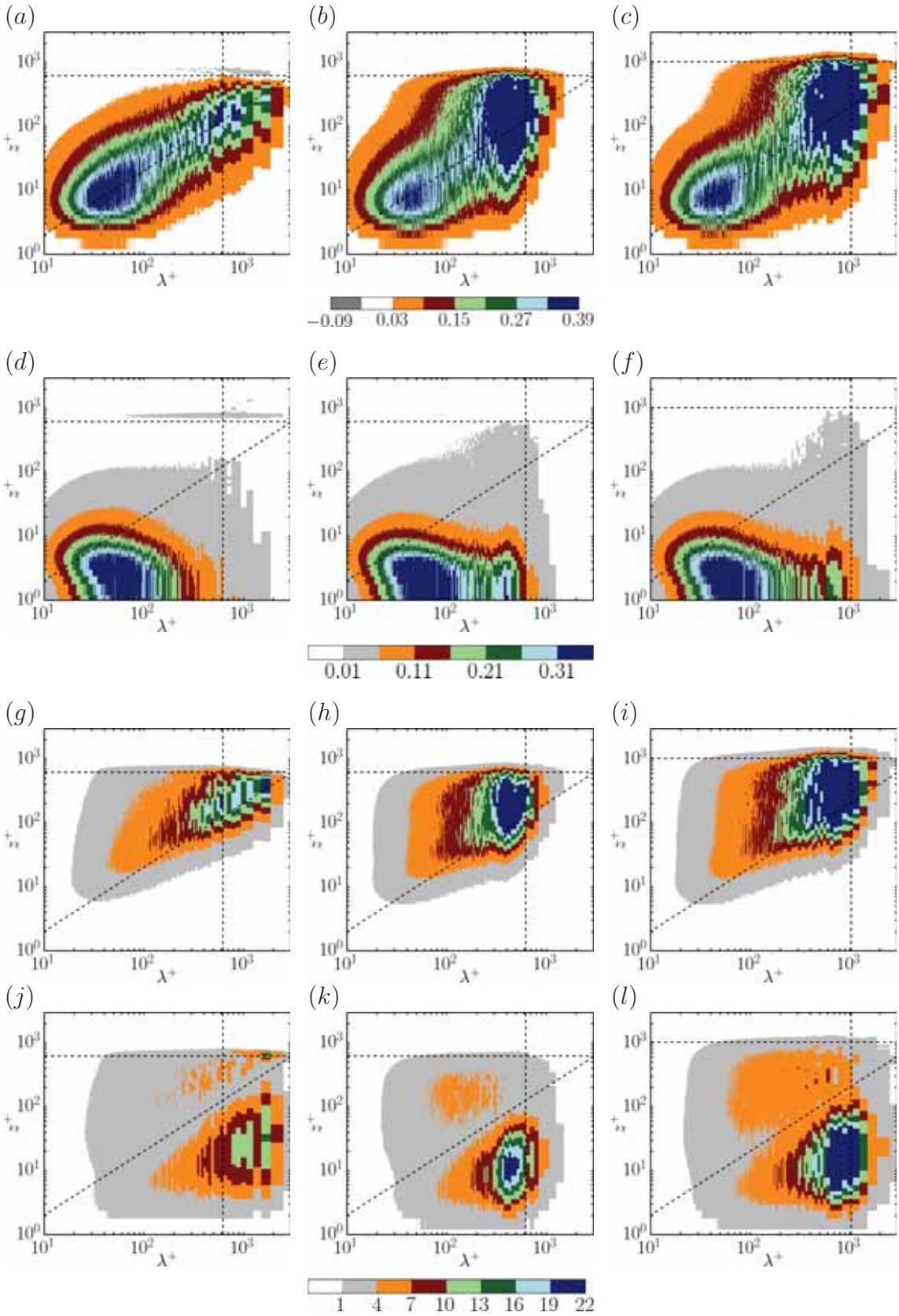

Figure 4.5: Radial pre-multiplied co-spectra and spectra, $\phi^{(\mathrm{r})}(\lambda, z)$, as a function of the radial wavelength, $\lambda = 2\pi/\kappa$, and the distance to the wall, z, in wall diffusive units. Rows: (a, b, c) buoyancy flux $\phi^{(\mathrm{r})}_{bw} = \kappa E^{(\mathrm{r})}_{bw}(\kappa)$; (d, e, f) buoyancy $\phi^{(\mathrm{r})}_{bb} = \kappa E^{(\mathrm{r})}_{bb}(\kappa)$; (g, h, i) vertical (wall-normal) velocity $\phi^{(\mathrm{r})}_{ww} = \kappa E_{ww}(\kappa)$; (j, k, l) horizontal (wall-parallel) velocity component $\phi^{(\mathrm{r})}_{uu} = \kappa E^{(\mathrm{r})}_{uu}(\kappa)$. Columns: (a, d, g, j), stably stratified case at $h^+ = 623$; (b, e, h, k), neutrally stratified case at $h^+ = 620$; (c, f, i, l), neutrally stratified case at $h^+ = 1034$. The vertical and horizontal lines correspond to a wavelength and a height equal to the boundary layer height h^+; the diagonal line corresponds to $\lambda = 5z$.

in the horizontal directions. This coalescence process is stronger between $z^+ \simeq 10$ and the height z where the dominant wavelength $\lambda = 5z$ becomes comparable to the boundary layer height h, i.e., $z = 0.2h$. This observation seems to favor a definition of the inner layer extent as $\sim 0.2h$. Beyond this height, the plumes seem to continue their ascent without further merging, and simply continue to rise in the form of towers that are separated a distance proportional to h (see Fig. 4.2a). As already pointed out, these towers are more well defined in the CBL than in the heated plate, which is most likely due to the capping effect of the stable stratification. The capping effect and the deflection of vertical motions to the horizontal support the formation of a strong coherent large-scale circulations that push the plumes to organize themselves into well-defined towers. The small negative contribution observed in Fig. 4.5a corresponds to the entrainment zone that develops in the strongly stratified case. This region is discussed in Chapter 5.

The heated plate's co-spectra differs from that of the CBL due to the additional strong and spectrally-broader signal with a wavelength of about $0.7h$ that extends from the boundary top at $z = h$ down to a small fraction of the boundary layer height, $\simeq 0.03h$ [1]. This additional contribution leads to the difference between the mean buoyancy flux profile of a heated plate and that of a CBL, as seen in Fig. 4.3a. Such a signal exists in the heated plate because in the absence of a capping layer, the thermals are free to rise, and are then breaking up and spreading as they do so. This phenomenon is corroborated by the larger dissipation rate found in the heated plate (see Fig. 4.3a). And since deflections of vertical motions to the horizontal direction are absent, there is also no strong driver for organization into coherent large-scale circulation.

Figure 4.5d-f shows the buoyancy spectra, where we see that most of the contribution to the buoyancy fluctuation is in the near-wall region and scales with inner scales, in agreement to the b_{rms} profile in Fig. 4.4d. The difference between the CBL and the heated plate case mainly lies within the diffusive wall region. In particular, a small modulation in the larger wavelengths is visible in the heated plate, but not in the CBL. We associate the absence of this signal in the CBL to the possibility that the large and more organized convective motions in the CBL mix buoyancy more efficiently in the near-wall region. In the heated plate, this signal in the larger wavelengths further penetrates into the overlap region, which is why the r.m.s. of the buoyancy fluctuation decays slower than in the CBL.

[1] For the scale separation achieved in these simulations, $\simeq 0.03h$ is relatively close to the wall diffusive region (about 20 and 30 wall units for the states $h^+ = 620$ and $h^+ = 1034$, respectively).

Figure 4.5g-i shows the vertical velocity spectra and figure 4.5j-l, the horizontal velocity spectra. The CBL and heated plate vertical velocity spectra are quite different roughly beyond the buoyancy gradient thickness $\delta_b^+ \simeq 4$. Consistent with the picture that the CBL has convective cells that have larger aspect ratio, both the vertical and horizontal velocity spectra have a signal in larger wavelengths in the CBL. The vertical velocity spectra does not support the key assumption of Adrian (1996) that the velocity scale near the wall region is comparable to that in the outer layer. Instead, the characteristic scale keeps increasing in magnitude with height, and it is displaced towards larger wavelengths as the boundary layer grows. Therefore, the theory of Adrian (1996) is not supported by our data even though the scalings that follow from this theory, $b^+_{\rm rms} \propto (z^+)^{-1/2}$ and $w^+_{\rm rms} \propto \log(z^+)$, seem to be observed in the corresponding DNS vertical profiles (see Fig. 4.4).

4.5 Discussion

The results in the previous sections support the propositions of Kraichnan (1962) and Businger (1973) that large scale convective motions produce 'convective wind gusts' that are affected by the outer scales, which is in contrast to the picture of classical similarity theory of spreading turbulent buoyant plumes that only depend on z. These convective wind gusts produce surface shears, although the mean of the vertical flux of horizontal momentum

$$\tau_{x_i z}/\rho_0 = v_i w - \nu \left(\partial_z v_i + \partial_{x_i} w\right), \tag{4.10}$$

is zero for both horizontal directions ($i = 1, 2$) due to the symmetry of the flow (the convective wind gusts do not have a preferred horizontal direction). Consequently, the usual atmospheric definition of friction velocity $u_* = \left[\langle v_1' w' \rangle^2 + \langle v_2' w' \rangle^2\right]^{1/4}$ is zero. On the other hand, the r.m.s. of the fluctuations of the turbulent (first term on r.h.s.) and molecular (second term) contributions to Eq. (4.10) are non-zero, as can be seen in Fig. 4.6b. The r.m.s. of the turbulent contribution is used in the definition of the minimum friction velocity (Businger, 1973; Zilitinkevich et al., 2006), $U_* = [\langle (v_1' w')^2 \rangle + \langle (v_2' w')^2 \rangle]^{1/4}$. But since DNS allows for the measurement of viscous shear stress at the wall [corresponding to the molecular contribution to Eq. (4.10)], the wall friction velocity can be measured as it is defined in wall-bounded shear flows,

$$u_\tau = \sqrt{\tau_w/\rho_0}\,, \tag{4.11}$$

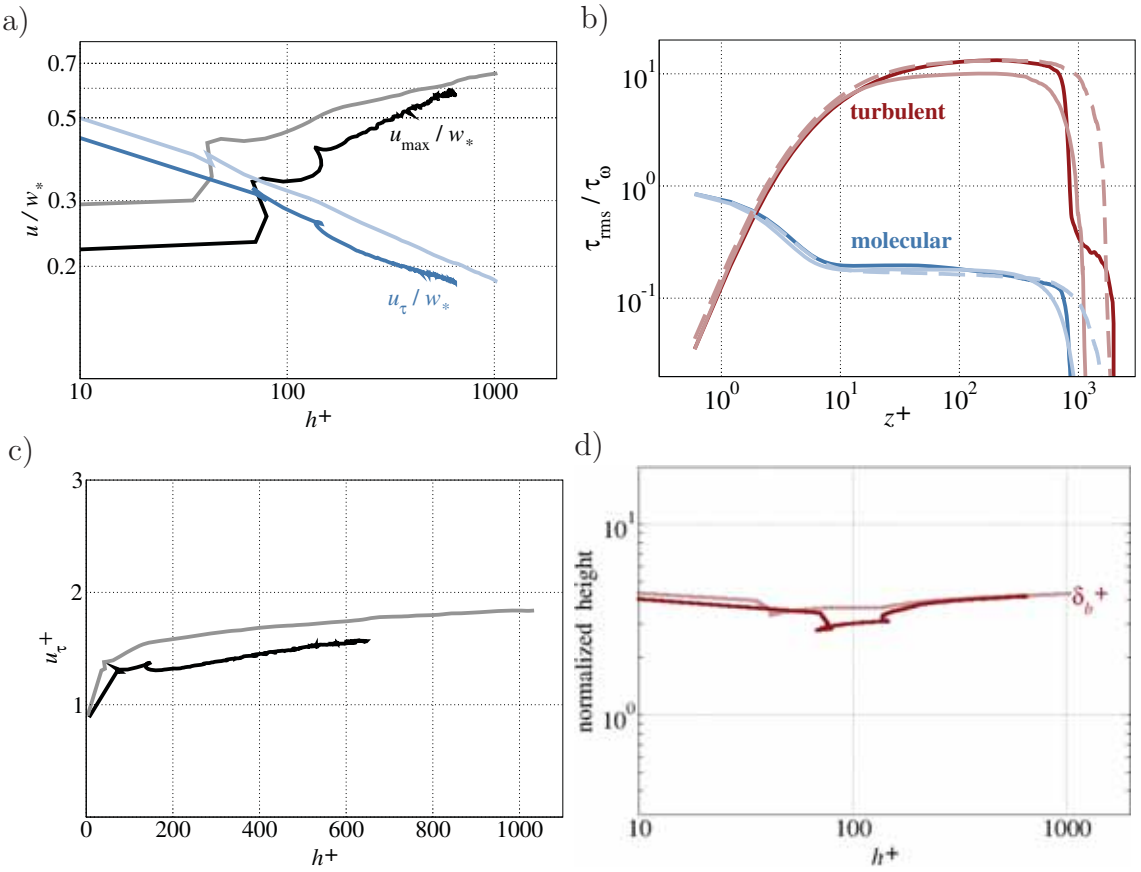

Figure 4.6: a)Temporal evolution of the maximum r.m.s. of the horizontal velocity fluctuation $u_{\max}$ normalized with the convective velocity w_* (black) and the resistance coefficient u_τ/w_* (blue). b) Vertical profile of the r.m.s. of the molecular (blue) and turbulent (red) contributions to vertical flux of horizontal momentum (one component). c) Temporal evolution of the wall friction velocity u_τ defined in Eq. (4.11) in wall diffusive units. d) Temporal evolution of the buoyancy gradient thickness, Eq. (4.4). Solid lines correspond to $h^+ \simeq 620$, and dashed lines to $h^+ \simeq 1034$ (only available for neutral case). Dark colors indicate the stably stratified case and light colors the neutral case.

where τ_w is the wall shear stress defined as $\tau_w = \sqrt{\langle \tau_{x_1 z}^2 \rangle + \langle \tau_{x_2 z}^2 \rangle}$ calculated at the wall $z = 0$. As seen in Figure 4.6b, the turbulent contribution to the flux of horizontal momentum within the surface layer is roughly an order of magnitude larger than the molecular contribution at the wall. This translates to U_* being roughly a factor of three ($\sim 10^{1/2}$) larger than u_τ. The advantage of using the wall friction velocity u_τ is its straightforward evaluation, unlike U_* which depends on z and the definition of the overlap region's extent. Figure 4.6c shows that the friction velocity in wall units u_τ^+ is of order one, which indicates that diffusive and viscous units are comparable, at least for the range of Rayleigh numbers considered in this work.

The ratio of the friction velocity u_τ and the convective velocity w_*, also called the resistance coefficient, is hypothesized by Businger (1973) to be a decreasing function of $h^+ = h/z_0$, in particular as $(h^+)^{-1/6}$ (see, e.g., Schumann, 1988; Zilitinkevich et al., 2006). For our aerodynamically smooth case, this means that the friction velocity should evolve as $(h^+)^{1/6}$, which seems to describe well the slight growth of u_τ^+ in Figure 4.6a (not explicitly shown). The values that we get for u_τ/w_* decrease from roughly 0.3 to 0.2 for scale separation h/z_0 of order 10^2 to 10^3, as shown in Fig. 4.6a. These values are comparable to the values presented in Zilitinkevich et al. (2006), which are values found in atmosphere and in LES, although the scale separation we achieve with our aerodynamically smooth case falls within the range of scale separation h/z_0 achieved with rough surfaces in Zilitinkevich et al. (2006). The decreasing behavior of the resistance coefficient is in contrast to the assumption of Beljaars (1994)'s that the friction velocity in the limit of free convection is proportional to the convective velocity w_*, which follows from Beljaars' treatment of the convective velocity as an extra wind component in the bulk transfer laws for the surface layer.

Similar to Beljaar's idea of using the convective velocity as an extra wind component, an alternative bulk buoyancy transfer law (equivalent to heat in the dry case) in the absence of a mean wind

$$B_0 = C_b (\Delta b)_s w_* \,, \tag{4.12}$$

uses the convective velocity w_* as a proxy for the friction velocity, where C_b is the heat transfer coefficient. Rewriting Eq. (4.12) as a ratio of buoyancies

$$\frac{(\Delta b)_s}{b_*} = C_b^{-1} = \left[(\Delta b)_s^+\right] (h/z_0)^{1/3} \,, \tag{4.13}$$

shows that the relation takes into account the roughness length z_0 and depends

on the boundary layer height. In particular, Schumann (1988) highlights how the nondimensional buoyancy difference $(\Delta b)_s/b_*$ is a function of the nondimensional height (h/z_0), namely $(h/z_0)^{1/3}$. Schumann (1988) and Zilitinkevich et al. (2006) prefer this alternative buoyancy transfer law over the traditional buoyancy transfer law for free convection (Townsend, 1964)

$$B_0 = C_s(\kappa^2/\nu)^{1/3}(\Delta b)_s^{4/3}, \tag{4.14}$$

because the traditional one only applies for smooth surfaces and does not consider the boundary layer thickness as a parameter. Notice however that the $h^{1/3}$ dependence of the Eq. (4.13) simply follows from the definition of $1/b_* = w_*/B_0 = B_0^{-2/3}h^{1/3}$. Rewriting Eq. (4.12) in the form

$$B_0 = Cz_0^{1/2}(\Delta b)_s^{3/2}\ , \tag{4.15}$$

eliminates the dependence on h that comes from w_* and reveals that the relevant part is actually the proportionality coefficient C that is affected by $(\Delta b)_s$ and the surface roughness z_0. The coefficient C is assumed in Schumann (1988) and Zilitinkevich et al. (2006) to be a constant. The value quoted in Schumann (1988) is $C \simeq 2.15^{-3/2} \simeq 0.32$ and those quoted in Zilitinkevich et al. (2006) are $C \simeq 3.3^{-3/2} \simeq 0.17$, from previous work and $C \simeq 0.6^{3/2} \simeq 0.46$, from their own work where they considered a wide range of surface roughness values.

Although there is clearly no consensus over the value of this coefficient, assuming this coefficient is constant implies for the aerodynamically smooth case that the relation Eq. (4.15) still assumes a constant $(\Delta b)_s^+$ and is therefore not different from the assumption of the traditional heat transfer law, Eq. (4.14). In this work where we only have a smooth wall, $(\Delta b)_s^+ = \delta_b^+$ and we observe that δ_b^+ is slightly varying in time, or scale separation h^+, as shown in Fig. 4.6d. The normalized buoyancy gradient thickness δ_b^+ is only slightly affected by stratification and therefore by outer scale effects. The transfer coefficient of the traditional transfer law C_s is then estimated in our case (Pr=1) by $(\delta_b^+)^{-4/3}$, which is actually the compensated Nusselt number shown in Figure 4.3d multiplied by $2^{4/3} \simeq 2.5$. Values of the order of $C_s \simeq 0.14$ at the latest time of the neutral case, as derived from Figure 4.3d, agrees relatively well with the value $C_s \simeq 0.10$ proposed by Beljaars (1994). For the alternative transfer law, Eq. (4.15), $C = (\delta_b^+)^{-3/2}$, and at the latest time, we obtain $C \simeq 0.11$, which is small compared to the aforementioned values, most likely due to absence of roughness effects.

We have shown that although our data and other studies (see, e.g., van Reeuwijk et al., 2008; du Puits et al., 2014) increasingly support the existence of convectively-driven shear flows near the wall, how to incorporate the convective winds into parameterizations is not as straightforward as using the convective velocity w_* as a proxy for the friction velocity, since we have also shown in the spectral analysis that w_* does not characterize the vertical velocities at the near wall region. Moreover, it is also unclear whether a simple application of MOST to these 'convective winds' is indeed appropriate. The applicability of MOST hinges on the quasi-steady behavior of the mean wind. But far from being quasi-steady, these 'convective winds' are actually largely perturbed and strongly affected by heterogeneity in the pressure gradients near the surface. Thus properly describing this mechanism might not be as simple as treating the convective winds in the sense of a quasi-steady wind-driven boundary layers at the surface, in which the smaller-scale turbulence is in local equilibrium or treating these near-surface flows as similar to stagnation-point boundary layers, both of which are suggested in Zilitinkevich et al. (2006). Moreover, there is no guarantee nor supporting evidence that the local mean wind profiles would exhibit logarithmic profiles, as assumed in Sykes et al. (1993). Further analysis of the internal boundary layer that is possibly developing near the wall due to these wind gusts is clearly required in the future.

5 The entrainment zone

The entrainment zone is the region where turbulence and stratification directly interact. This interaction affects the properties of the entrainment zone (e.g. EZ thickness and characteristics scales), such that the scaling for the entrainment zone statistics are different from the scaling in the convective well-mixed layer; as shown in Fig. 3.3 and Fig. 5.1, statistics at the EZ do not collapse when normalized with the encroachment and convective scales. Hence, unlike the mixed layer, the EZ does not have established scales that characterize the statistics there. Our aim is to investigate the characteristic scales of the entrainment zone, and the possible self-similar behavior of the buoyancy profiles inside the entrainment zone (Fedorovich and Mironov, 1995; Sorbjan, 1999; Fedorovich et al., 2004b) associated with these characteristic scales. We also assess the effect of this vertical structure on the entrainment-rate parameters (Betts, 1974; Sullivan et al., 1998) and the relation between the entrainment rate and a Richardson number (Deardorff et al., 1980; Fedorovich et al., 2004b; Träumner et al., 2011).

5.1 Vertical structure of the entrainment zone

In light of the common assumption that the EZ thickness is proportional to the CBL thickness (Sullivan et al., 1998), we define a first sublayer in the entrainment zone with a thickness $z_{i,g} - z_{i,0}$ that is proportional to the CBL thickness, based on

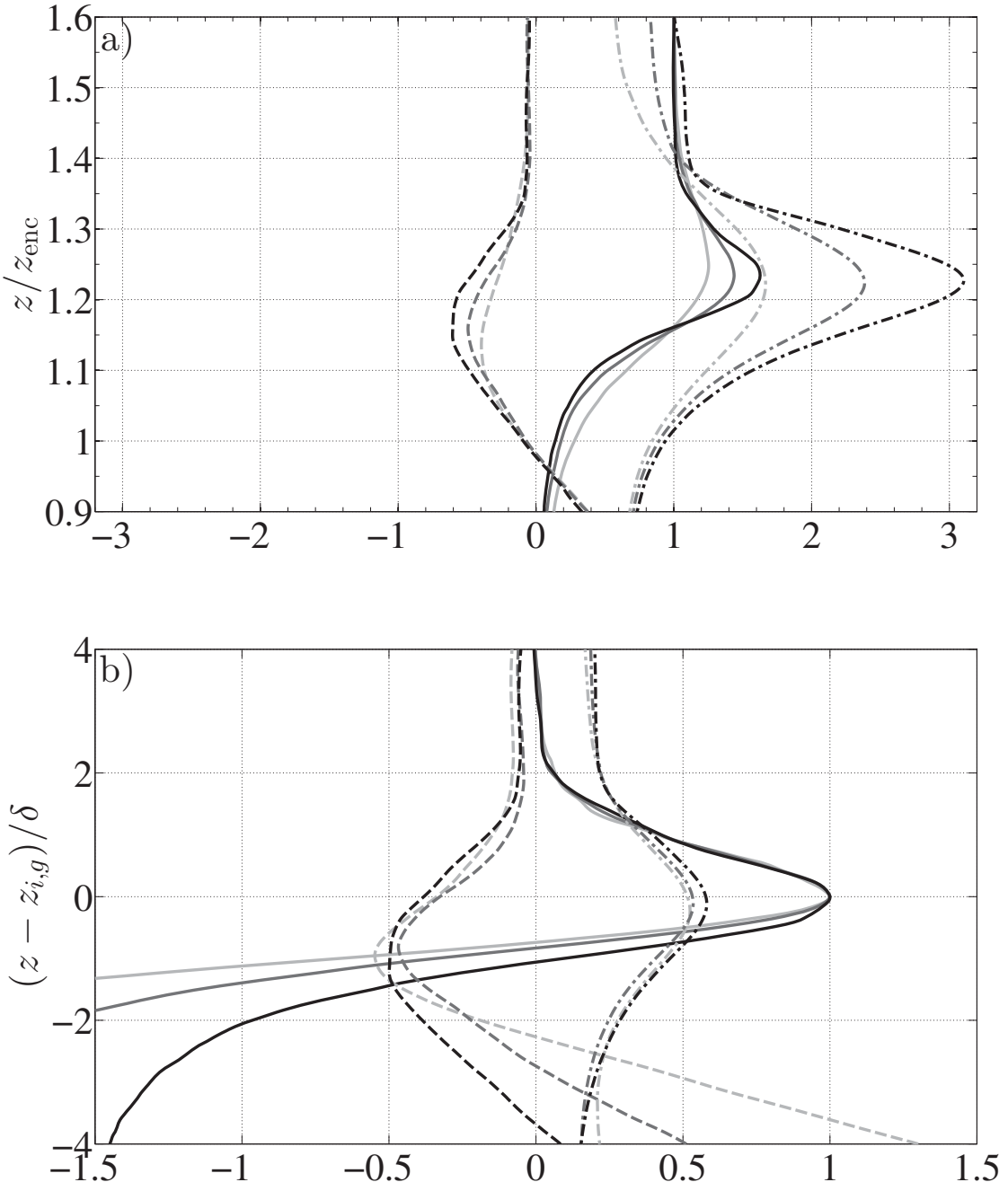

Figure 5.1: a) Vertical profiles inside the entrainment zone normalized by z_{enc}: $(\partial \langle b \rangle / \partial z)/N^2$ (solid), b_{rms}/b_* (dash-dotted line), and B/B_0 multiplied by a factor of 5 for emphasis (dashed line). b) Vertical profiles inside the entrainment zone centered at $z_{i,g}$ and normalized by δ: $(\partial \langle b \rangle / \partial z - N^2)/(b_\delta/\delta - N^2)$ (solid), $b_{\mathrm{rms}}/b_\delta$ (dash-dotted line), and $B/(b_\delta w_{\mathrm{rms}}(z_{i,g}))$ multiplied by a factor of 5 for emphasis (dashed line). Light gray, gray, and black indicate snapshots from simulation Re100 at $z_{\mathrm{enc}}/L_0 \simeq \{10, 14, 18\}$, respectively.

the observed proportionality among the different definitions of the CBL-top height discussed in Chapter 3 (Fig. 3.1). Using the coefficients from Table 3.1, we can write $z_{i,g} - z_{i,0} = (C_{\mathrm{enc},g} - C_{\mathrm{enc},0}) z_{\mathrm{enc}} \simeq 0.25 z_{\mathrm{enc}}$. Notice that roughly from $z_{i,0}$ to $z_{i,f}$, the mean buoyancy gradient is smaller than the original background buoyancy gradient N^2, while the r.m.s. of the buoyancy fluctuations at the most part of this lower sublayer still seems to be scaling with b_* (Fig. 5.1a).

However, as we approach the height of maximum mean buoyancy gradient $z_{i,g}$, the vertical profiles of the mean buoyancy gradient and of the r.m.s. of the buoyancy fluctuations, $b_{\mathrm{rms}} = \langle b'b' \rangle^{1/2}$, do not scale with either the encroachment scales nor with the convective scales; as shown in Fig. 5.1a. Around the height $z_{i,g}$, the magnitude of these normalized quantities keep increasing in time. This behavior suggests that we consider an upper EZ sublayer centered at $z_{i,g}$ whose thickness is not a constant fraction of the CBL thickness, but instead is proportional to a local length scale. One possible definition of this characteristic length scale is based on the relation

$$\langle b \rangle (z_{i,g}) + \frac{\partial \langle b \rangle}{\partial z}(z_{i,g}) \delta = b_{\mathrm{bg}}(z_{i,g}) + N^2 \delta \ , \tag{5.1}$$

sketched in Fig. 5.2. This expression can be written as

$$\delta = - \frac{\langle b \rangle (z_{i,g}) - b_{\mathrm{bg}}(z_{i,g})}{\frac{\partial \langle b \rangle}{\partial z}(z_{i,g}) - N^2} \ . \tag{5.2}$$

This is a gradient thickness definition that is often employed in the characterization of turbulent mixing layers that separate two regions where the flow is statistically homogeneous in the two directions perpendicular to the mean gradient (see, e.g., Pope, 2000). Hence, the definition (5.2) supports the interpretation of the upper EZ sublayer as a transition region, based on the buoyancy field, between the nonturbulent, stably stratified fluid above and the turbulent layer below.

The corresponding buoyancy scale within the upper EZ sublayer is

$$b_\delta = \frac{\partial \langle b \rangle}{\partial z}(z_{i,g}) \delta \ , \tag{5.3}$$

which is similar to the scaling proposed by Sorbjan (1999).

When normalized with δ and b_δ, the profiles of mean buoyancy gradient and buoyancy r.m.s. at different times approximately collapse on top of each other (Fig. 5.1b). This self-similar behavior of the buoyancy profiles resembles the self-similarity hypothesis that underlies the general structure models of the EZ (Fedorovich and

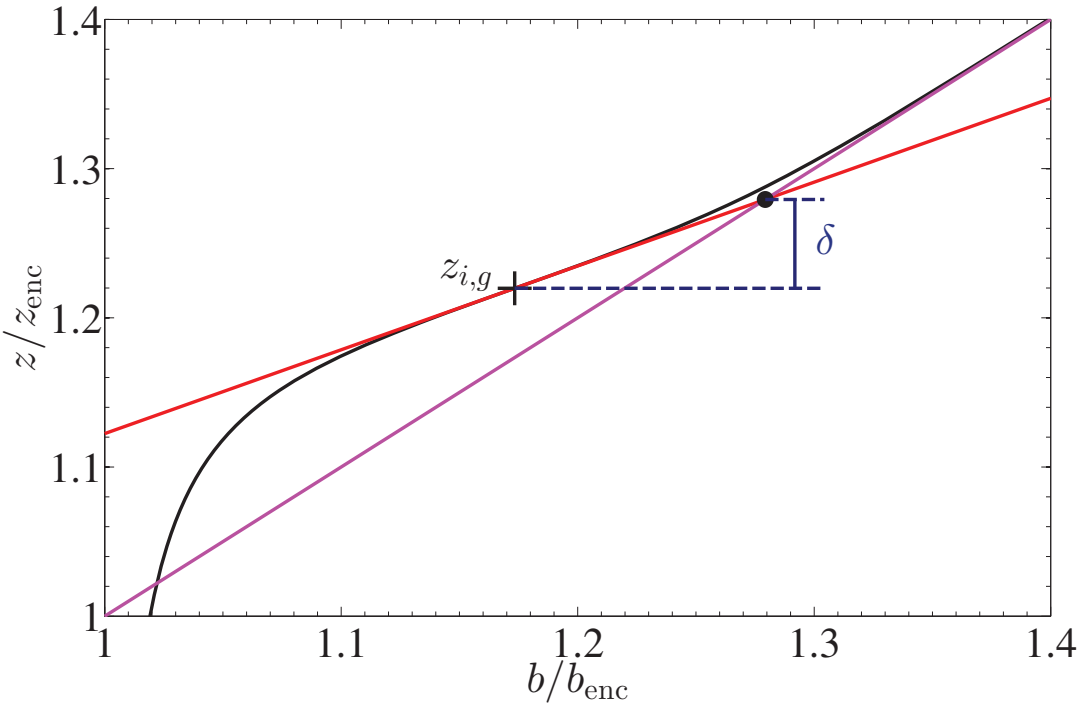

Figure 5.2: Sketch illustrating the definition of the local thickness δ, Eq. (5.2), characterizing the upper EZ sublayer. The mean buoyancy profile (solid black) corresponds to the final time of simulation Re040 ($z_{\rm enc}/L_0 \simeq 26$); tangent line at the point of maximum buoyancy gradient (marked with a +) is shown in red; the background buoyancy profile is shown in magenta.

Mironov, 1995; Fedorovich et al., 2004b), though we find that it applies only within the upper EZ sublayer, namely, in a region $z_{i,g} \pm \delta$, and not across the entire entrainment zone, as originally postulated in those models.

For the rest of this section, we discuss the physical mechanism that causes this mixing region $z_{i,g} \pm \delta$ and the interpretation of the characteristic scales δ and b_δ. In addition, we also provide explicit parameterizations for these scales as a function of the independent variable $z_{\rm enc}/L_0$, so that the buoyancy profiles inside the EZ can be reconstructed at any time, if desired.

5.1.1 The length scale δ

δ as the mean penetration depth of thermals

Figure 3.2 and, with more detail, Fig. 5.3a,b illustrate that the upper EZ sublayer is a region characterized by turbulent thermals penetrating into a smoothly varying environment. Qualitatively, we can interpret the height $z_{i,g}$ and the thickness δ, respectively, as a rough estimate of the mean and standard deviation of the vertical location of the top of the interface undulations, or domes, that are created by the overshooting thermals (Fig. 5.4). On the other hand, the lower EZ sublayer is characterized by the updrafts, acting as pillars that support the domes in the upper EZ sublayer, and by the turbulent troughs in between the domes (Fig. 5.3c,d). Within this lower EZ sublayer, we find strong fluctuations in buoyancy field all across the horizontal extent.

The interpretation of δ as the mean penetration depth above $z_{i,g}$ that the thermals reach is supported by parcel theory. This theory states that given a parcel of fluid with a vertical velocity w' at its neutral buoyancy level, the vertical displacement reached by this parcel of fluid inside a linearly stratified region with buoyancy frequency N is proportional to w'/N (Zeman and Tennekes, 1977; Xuequan and Hopfinger, 1986; Hopfinger, 1987; Smyth and Moum, 2000).

For the fluid parcels at $z_{i,g}$, we can propose that $w' \sim w_{\mathrm{rms}}(z_{i,g})$. At the same time, we observe in our simulation that the integral velocity scale of the turbulence inside the upper EZ sublayer is a constant fraction of the convective velocity,

$$w_{\mathrm{rms}}(z_{i,g}) \simeq c_{w2} w_* \tag{5.4}$$

(Fig. 5.5a) beyond $z_{\mathrm{enc}}/L_0 \simeq 10$, where $c_{w2} \simeq 0.2$ (Table 5.1). Therefore, we can write

$$\delta \simeq c_\delta (w_*/N) \; . \tag{5.5}$$

Indeed, Fig. 5.5b demonstrates that δ follows this scaling within the equilibrium entrainment regime, beyond $z_{\mathrm{enc}}/L_0 \simeq 10$, and that $c_\delta \simeq 0.55$. The Reynolds number dependence of this constant is already negligibly small for the Reynolds numbers $\mathrm{Re}_0 \simeq 100$ achieved in our simulations (about 2%, less than the uncertainty $\simeq 5\%$ associated with the statistical convergence, see Table 5.1).

From Eq. (5.5) and the definition of w_*, we see that δ is actually increasing in time

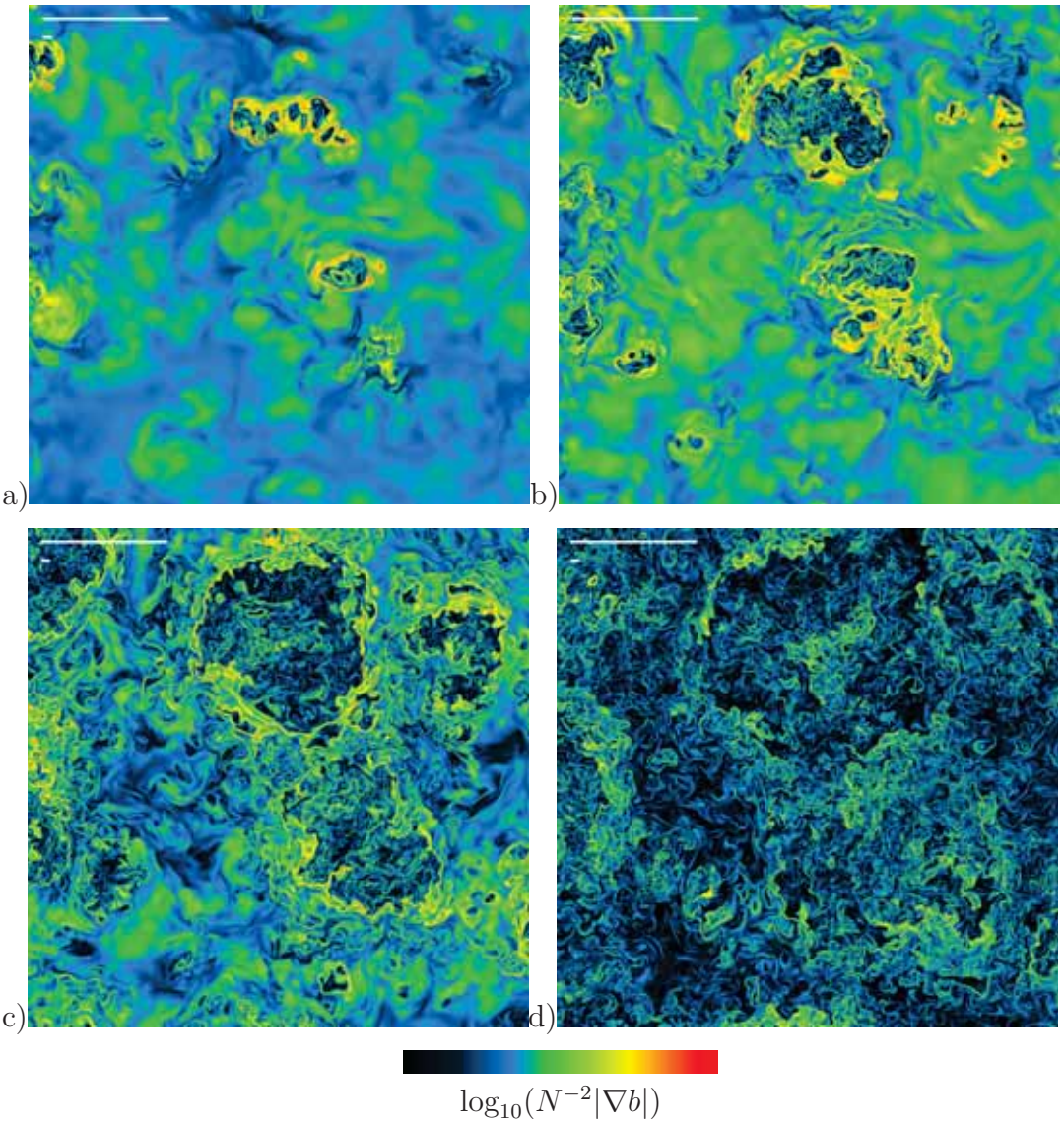

Figure 5.3: Horizontal cross-sections showing the logarithm of the magnitude of the buoyancy gradient $N^{-2}|\nabla b|$ inside the entrainment zone for the case Re100 at the final time $z_{\rm enc}/L_0 = 18$ (only 1/9 of the domain is shown). Colors black, blue, yellow and red correspond, respectively, to values varying between 10^{-1} and 10^2 in intervals of 10. The heights are: a) $z = z_{i,1} = z_{i,g} + \delta$; b) $z = z_{i,g}$; c) $z = z_{i,f}$; d) $z = z_{i,0}$. The long horizontal white bar at the top-left corner of each panel indicates a length equal to $z_{\rm enc}$, Eq. (2.5); the short one indicates a length equal to δ, Eq. (5.2).

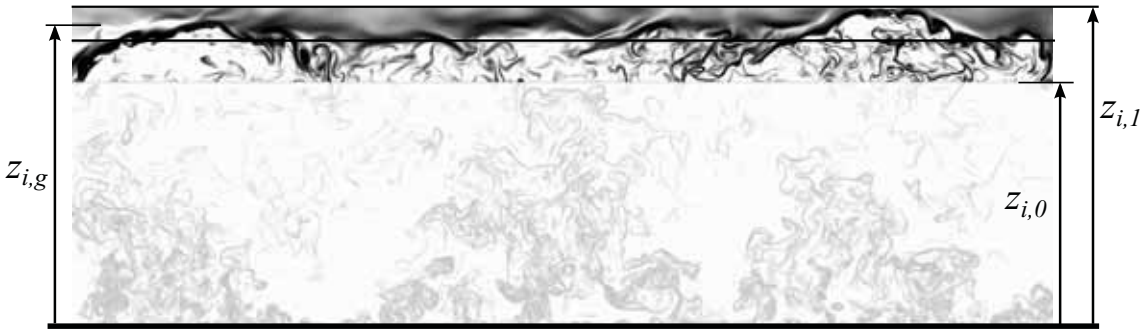

Figure 5.4: Extracted region from Fig. 3.2 (there highlighted) emphasizing the entrainment zone. The upper EZ sublayer, $z_{i,g} \pm \delta$, (enclosed by two horizontal lines, where $z_{i,1} = z_{i,g} + \delta$) features the overshooting thermals, and corresponds to the region directly affected by the stably stratified overlying fluid. The lower EZ sublayer, $z_{i,g} - z_{i,0}$, features the troughs of the undulations there. The layer below $z_{i,0}$ (masked region) is the well-mixed layer.

according to

$$\delta/L_0 = c_\delta (z_{\rm enc}/L_0)^{1/3} \,, \tag{5.6}$$

but, with respect to $z_{\rm enc}$, it continuously decreases as

$$\delta/z_{\rm enc} = c_\delta \, (z_{\rm enc}/L_0)^{-2/3} \,. \tag{5.7}$$

This scaling of δ highlights the effect of the stratification on the geometry of the turbulent structures inside the entrainment zone. If there were no stratification ($N^2 = 0$), the size of the undulations due to the thermals would scale with the boundary-layer thickness and entrainment would be dominated by large-scale engulfment (Mellado, 2012) [see also Fig. 4.2b]. With stratification, an interval $z_{i,g} - z_{i,0}$ of the entrainment zone retains the scaling proportional to the CBL thickness $z_{\rm enc}$, but a second sublayer develops within the region of the EZ that is closer to the stably stratified layer. This upper EZ sublayer can be interpreted as a transition region between the convectively mixed layer, characterized to leading order by $z_{\rm enc}$ and w_*, and the stably stratified layer above, characterized by w_* and N. The properties of this upper EZ sublayer depend directly on N, in contrast to those inside the lower EZ sublayer, where N enters only indirectly through the dependence of the CBL thickness $z_{\rm enc}$ on the buoyancy frequency N as in Eq. (2.5).

Finally, the scaling above also means that, as the CBL grows, the upper EZ sublayer, with extent $z_{i,g,} \pm \delta$, becomes a smaller fraction of the lower EZ sublayer, with an extent $(z_{i,g} - z_{i,0}) \simeq 0.25 z_{\rm enc}$. Notice, however, that for a significant range of typical atmospheric conditions ($z_{\rm enc}/L_0 \simeq 10 - 50$, see section 2.2), the upper EZ sublayer

still occupies a significant fraction of the entrainment zone, since $2\delta/(z_{i,g} - z_{i,0})$ varies between 0.95 and 0.46 within this range.

δ as the integral length scale of turbulence

Simple models of the CBL usually assume that the turbulence within the CBL is characterized by a single length scale, that is, the CBL thickness z_i. Such an assumption corresponds to the loss of TKE to viscous dissipation as a fixed fraction of the total TKE production because $\varepsilon \propto w_*^3/z_i = B_0$. However, the existence of a turbulence integral length inside the EZ that is different from the CBL thickness z_{enc} (or a constant fraction thereof) has previously been considered due to increasing evidence that the viscous dissipation rate ε inside the EZ is not a fixed fraction of the rate of energy input into the system (Linden, 1975; Tennekes, 1975; Guillemet et al., 1983). The reason for this behavior was attributed to the influence of stratification on the turbulence near the stratified interface (Zeman and Tennekes, 1977; Mahrt, 1979). The scaling

$$\varepsilon(z_{i,g}) \simeq c_\varepsilon [w_{\mathrm{rms}}(z_{i,g})]^3/\delta \tag{5.8}$$

observed in Fig. 5.5c for roughly $z_{\mathrm{enc}}/L_0 \geq 10 - 15$, where $c_\varepsilon \simeq 0.5$, supports those hypotheses. In particular, this inviscid scaling of the viscous dissipation rate implies that δ is not only the mean penetration depth of thermals, but also represents the integral length scale of the turbulence inside the crests or domes of the overshooting thermals (Pope, 2000). Note that although Eq. (5.8) implies that the dissipation rate at the upper EZ sublayer is increasing, the integrated or bulk dissipation rate within that region does not blow up in time since the ratio δ/z_{enc} is concurrently decreasing (Eq. 5.7).

Consistent with the scalings Eq. (5.5) and Eq. (5.8), the Ozmidov scale within these turbulence regions or turbulence pockets inside the upper EZ sublayer (Fig. 5.3a,b) is proportional to δ according to

$$\left[\frac{\varepsilon(z_{i,g})}{N^3}\right]^{1/2} = (c_\varepsilon c_{w2}^3/c_\delta^3)^{1/2}\,\delta\ , \tag{5.9}$$

with $(c_\varepsilon c_{w2}^3/c_\delta^3)^{1/2} \simeq 0.2$ (Table 5.1). The Ozmidov scale characterizes the size of the largest eddies in fully developed turbulence under a homogeneous stratification (Ozmidov, 1965; Smyth and Moum, 2000) and thus the local integral scale, δ in our case. Interestingly, the reference Ozmidov scale L_0 is actually comparable in

magnitude to δ within the interval $z_{\rm enc}/L_0 \simeq 10-26$ (see Table 2.1). Therefore, L_0 provides a first estimate of the characteristic length δ for this range of typical atmospheric conditions. This also implies that the reference Reynolds number Re_0 is not only a control parameter of the problem, but also approximates well the Reynolds number Re_δ that characterizes the turbulence inside part of the entrainment zone, since

$$\mathrm{Re}_\delta = \frac{\delta\, w_{\rm rms}(z_{i,g})}{\nu} = (c_{w2}/c_\delta)\mathrm{Re}_0\,(\delta/L_0)^2\ , \tag{5.10}$$

where $c_{w2}/c_\delta \simeq 0.44$ (Table 5.1) and δ/L_0 varies between 1.1 and 1.9 (Eq. 5.6) for $z_{\rm enc}/L_0$ varying between 10 and 50. As expected, the Reynolds number within this region is smaller (around $\sim 10^2$) than the convective one due to the impeded vertical motions of turbulence. The scale separation between δ and η is still moderate, a possible explanation for the Reynolds number effects (slight difference of some EZ scalings between Re040 and Re100) that we observe for some EZ statistics.

In sum, our results confirm the previous hypothesis (Zeman and Tennekes, 1977; Mahrt, 1979) that the integral length scale of the turbulence locally within the entrainment zone is modified by the stable stratification, more specifically, within the upper EZ sublayer. In addition, we have provided an explicit parameterization of this integral length scale in terms of the independent variable $z_{\rm enc}/L_0$ in Eq. (5.6).

		c_{w2}	c_δ	c_ε	c_{b1}	c_{b2}	c_{b3}
Re040	Mean	0.19	0.53	0.68	0.39	0.47	0.43
	$\sigma(\%)$	5.1	5.0	7.5	4.2	4.8	16
Re100	Mean	0.23	0.52	0.51	0.39	0.55	0.44
	$\sigma(\%)$	3.8	6.5	6.3	5.3	5.2	11

Table 5.1: Constants defining the vertical structure of the entrainment zone, calculated within the equilibrium entrainment regime ($z_{\rm enc}/L_0 \geq 10$).

5.1.2 The buoyancy scale b_δ

From Eq. (5.2) and Eq. (5.3), the buoyancy scale b_δ can be equivalently defined as

$$b_\delta = N^2\delta + \left[b_{\rm bg}(z_{i,g}) - \langle b\rangle\,(z_{i,g})\right]\ . \tag{5.11}$$

This expression allows us to interpret b_δ, and therefore the maximum buoyancy r.m.s. (Fig. 5.1b), as a combination of two buoyancy increments.

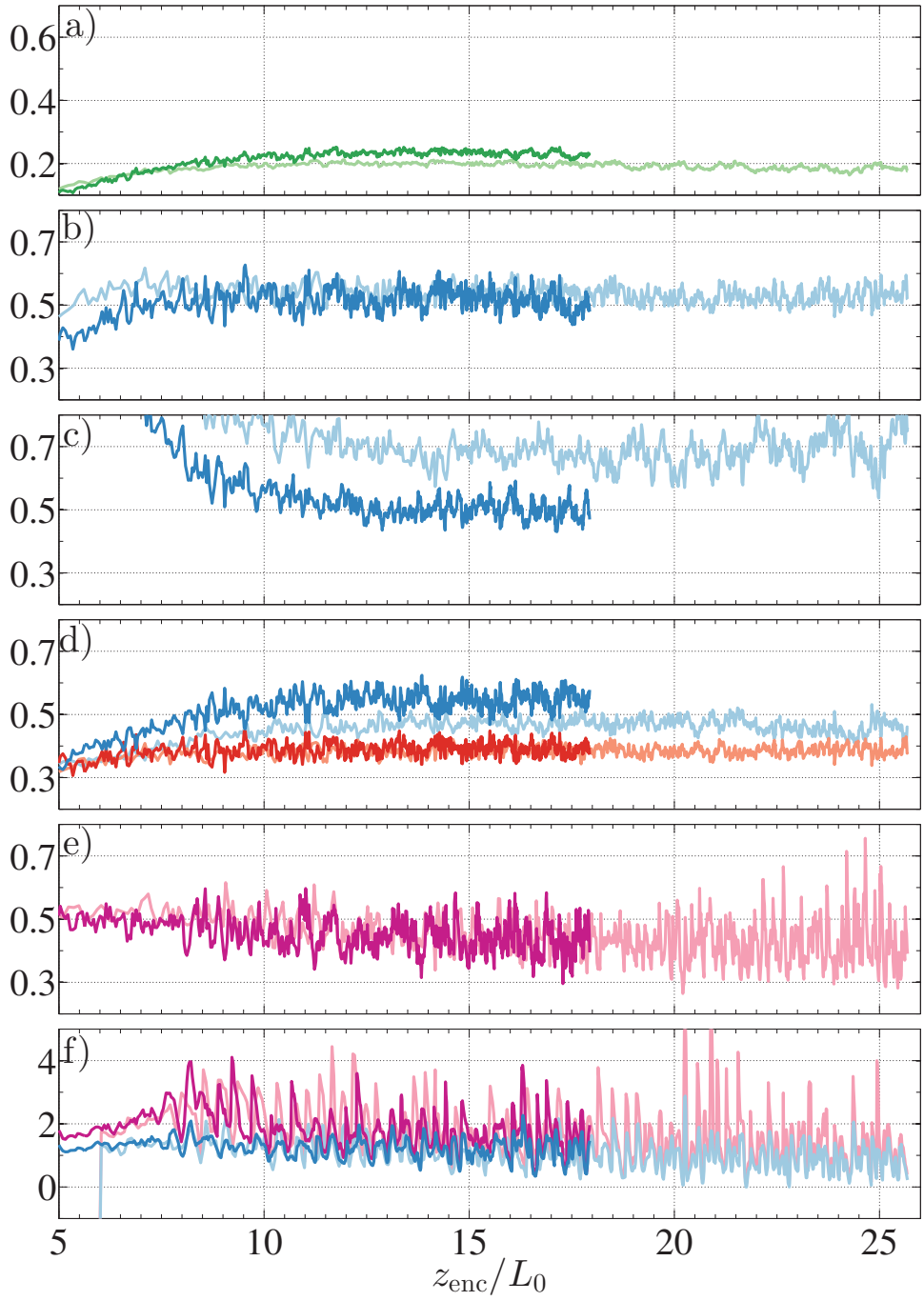

Figure 5.5: Temporal evolution of the characteristic scales inside the upper EZ sublayer: a) velocity, $w_{\mathrm{rms}}(z_{i,g})/w_*$; b) length, $\delta/(w_*/N)$; c) local inviscid scaling of the viscous dissipation rate, $\delta\varepsilon(z_{i,g})/[w_{\mathrm{rms}}(z_{i,g})]^3$; d) buoyancy, $b_{\mathrm{rms}}(z_{i,g})/b_\delta$ (blue) and $b_\delta/\left[N^2\delta + N^2(z_{i,g} - z_{\mathrm{enc}})\right]$ (red). Panel e) corresponds to the buoyancy scale inside the lower EZ sublayer, $[\langle b\rangle(z_{i,f}) - b_{\mathrm{enc}}]/[\langle b\rangle(z_{i,g}) - b_{\mathrm{enc}}]$. Panel f) shows $(z_{10\%\mathrm{mbf}} - z_{i,g})/\delta$ (blue) and $(z_{5\%\mathrm{mbf}} - z_{i,g})/\delta$ (magenta), comparing the upper EZ limit definitions $z_{10\%\mathrm{mbf}}$, the height where the buoyancy flux is 10% of the minimum, and $z_{5\%\mathrm{mbf}}$, corresponding to 5%, to the definition $z_{i,1} = z_{i,g} + \delta$. Quasi-steady behavior beginning at $z_{\mathrm{enc}}/L_0 \simeq 10$ is observed for all quantities and the corresponding mean values are summarized in Table 5.1. Light colors correspond to Re040, dark colors to Re100.

The first contribution in Eq. (5.11), $N^2\delta$, can be interpreted, according to parcel theory, as the buoyancy force experienced by a parcel of fluid after a displacement δ from its neutral level across a region with a buoyancy stratification N^2. Our numerical results show that the corresponding Richardson number

$$\mathrm{Ri}_\delta = \frac{\delta(N^2\delta)}{w_*^2} = c_\delta^2 \tag{5.12}$$

is constant ($c_\delta^2 \simeq 0.3$). This constant behavior represents a continuous balance of potential and kinetic energy in the entrainment zone: on the one hand, if the buoyancy difference between the thermals and the environment is much stronger than $N^2\delta$ such that the thermals cannot penetrate into the stably stratified region anymore, then continuous buoyancy input from below will decrease this buoyancy difference until the thermals can overshoot again; on the other hand, if the buoyancy difference is much weaker than $N^2\delta$, the unhindered thermals will overshoot to a level of higher buoyancy, consequently steepening the mean buoyancy gradient across the upper portion of the EZ.

The second contribution in Eq. (5.11), the buoyancy difference $b_{\mathrm{bg}}(z_{i,g}) - \langle b\rangle(z_{i,g})$, can be interpreted as the effective buoyancy increment with respect to $\langle b\rangle(z_{i,g})$, that is felt by the non-thermal regions, whose buoyancy is better characterized by the background buoyancy profile b_{bg}. The existence of two contributions to b_δ is consistent with the visualization (Fig. 5.3a,b and Fig. 5.4), because only a fraction of the upper EZ sublayer is occupied by penetrating thermals.

In order to predict b_δ, Eq. (5.11), and thereby the mean buoyancy gradient and the r.m.s. of the buoyancy fluctuations inside the EZ, we still need an explicit parameterization of $\langle b\rangle\,(z_{i,g})$. From the previous observation that the mean state of the upper EZ sublayer seems to represent an average of thermal- and non-thermal regions, we propose the relation

$$b_\delta = c_{b1}\left[N^2\delta + N^2(z_{i,g} - z_{\mathrm{enc}})\right] \ . \tag{5.13}$$

This parameterization is validated in Fig. 5.5d. The constant is $c_{b1} \simeq 0.4$ (see Table 5.1).

With this last step, we have obtained a complete parameterization of the buoyancy-related quantities within the upper EZ sublayer, given the controlling parameters

B_0 and N^2: The buoyancy scale is parameterized as

$$b_\delta = c_{b1} b_{\rm enc} \left[C_{{\rm enc},g} - 1 + (\delta / z_{\rm enc}) \right] \ , \tag{5.14}$$

where $\delta / z_{\rm enc}$ is given by Eq. (5.7) and $b_{\rm enc} = N^2 z_{\rm enc}$ (see Chapter 3 section 3.2). The mean buoyancy at $z_{i,g}$, using Eq. (5.11), is parameterized as

$$\langle b \rangle \left(z_{i,g} \right) = b_{\rm enc} + \left[(1 - c_{b1}) / c_{b1} \right] b_\delta \ , \tag{5.15}$$

the mean buoyancy gradient at $z_{i,g}$, from Eq. (5.3), is parameterized as

$$b_\delta / \delta = c_{b1} N^2 \left[1 + (C_{{\rm enc},g} - 1)(\delta / z_{\rm enc})^{-1} \right] \ , \tag{5.16}$$

and the maximum r.m.s. of the buoyancy fluctuations is parameterized as

$$b_{\rm rms}(z_{i,g}) = c_{b2} b_\delta \tag{5.17}$$

where $c_{b2} \simeq 0.55$ (Fig. 5.5d and Table 5.1).

We note that despite the relatively low Reynolds numbers ${\rm Re}_\delta = O(10^2)$ inside the EZ that we achieve in the simulations (Eq. 5.10), the coefficients that are relevant for the discussion that follows, namely, $\{c_\delta,\, c_{b1},\, c_{b2}\}$ and c_{b3} in section 5.2, already show a relatively low Reynolds number dependence (Table 5.1). The largest variation between the two cases Re040 and Re100 occurs in c_{b2} and it is less than 15%, and for the other coefficients, is about 2%. More importantly, we can differentiate between the variation of the mean and variance profiles of the buoyancy field that is caused by the temporal evolution of the EZ, and the variation due to Reynolds number effects. In particular, the r.m.s. of buoyancy fluctuation varies by a factor of 3 between $z_{\rm enc}/L_0 = 10$ and $z_{\rm enc}/L_0 = 26$, whereas the change due to an increase by almost a factor of three in the Reynolds number between case Re040 and case Re100 is less than 15% (coefficient c_{b2}).

5.1.3 Discussion on the multiplicity of scales

Although the length scale δ characterizes the thickness of the upper EZ sublayer and the integral length scale inside the turbulence pockets that exist in this sublayer, δ is not the only characteristic length scale within the entrainment zone. For example, the wavelength of the undulations along the horizontal directions are characterized

by the CBL thickness, as observed from spectral and correlation analysis (not shown) and as documented previously (see, e.g., de Roode et al., 2004). However, in this work we focus solely on δ because of its relevance for the buoyancy profiles, for the two-layer structure of the entrainment zone, and for the entrainment-rate parameters (section 5.2).

We also point out that Eq. (5.13) can be written as

$$b_\delta = c_{b1}\delta b_i \ , \tag{5.18}$$

where

$$\begin{aligned} \delta b_i &= b_{\rm bg}(z_{i,1}) - b_{\rm enc} = N^2 \delta z_i \ , \\ \delta z_i &= z_{i,g} + \delta - z_{\rm enc} = z_{\rm enc}\left[C_{{\rm enc},g} - 1 + (\delta / z_{\rm enc})\right] \ , \end{aligned} \tag{5.19}$$

and that we can interpret δb_i and δz_i as the buoyancy difference and EZ thickness definitions proposed and used in Fedorovich et al. (2004b) to parameterize the vertical profiles inside the entrainment zone according to the general structure model. However, there are notable differences. First, due to the clear definition of δ, the definition of the EZ upper extent as $z_{i,1} = z_{i,g} + \delta$ is equivalent to but more robust than the definition used by Fedorovich et al. (2004b) based on the zero-crossing (not shown due to large scatter in data), or based on a given fraction of the turbulent buoyancy flux, (see Fig. 5.5f for a comparison). Second, we have shown that each of these two parameters δb_i and δz_i are composed of two characteristic scales that evolve differently in time as the CBL grows. Third, the self-similar behavior of the vertical profiles normalized using δ and b_δ is restricted to the upper EZ sublayer, and is not observed for the entire region of negative mean buoyancy flux.

This multi-layer structure and the multiplicity of scales inside the EZ help to explain why difficulties were encountered in finding the appropriate scaling of the thickness for general structure models (Fedorovich and Mironov, 1995; Fedorovich et al., 2004b), since these models rely on a single scale. This explanation seems to be more satisfactory than one based on gravity-wave radiation, whose effect in the analysis of the EZ vertical structure has often been reported to be small (Deardorff et al., 1980; Zilitinkevich, 1991; Fedorovich et al., 2004b). Our findings could then be used to guide the development of a blending length scale that transitions from the convective length scale to the local gradient thickness that could be used to extend the general structure model of Fedorovich and Mironov (1995).

It is worth emphasizing that b_δ, or δb_i as defined above, quantifies the variation of the

mean buoyancy and buoyancy r.m.s. that results from an average between the crest regions with relatively large mean buoyancy gradient, and the regions in between with relatively small mean buoyancy gradient (Fig. 5.3a,b). The buoyancy scales b_δ and δb_i should not be interpreted as the buoyancy increment that the thermals feel or work against, which is better represented by $N^2\delta$ only. In other words, the CBL grows continuously against a constant stratification N^2, and not against an increasing buoyancy increment δb_i. (The decrease in time of the growth rate is due to the increasing CBL thickness over which the constant surface energy flux needs to be distributed, as quantified by the encroachment height, and not due to the increasing stratification δb_i.)

Last, the ratio between the EZ thickness, defined as δz_i, and the CBL thickness, $z_{\rm enc}$, evolves according to

$$\frac{\delta z_i}{z_{\rm enc}} = C_{{\rm enc},g} - 1 + (\delta / z_{\rm enc}) \; . \tag{5.20}$$

The corresponding decrease in time towards the asymptotic value $C_{{\rm enc},g} - 1 \simeq 0.24$ as $\delta / z_{\rm enc}$ decreases was already found by Deardorff et al. (1980). However, as explained by those authors, the corresponding scaling was not well understood because neither the penetration depth δ nor the CBL thickness $z_{\rm enc}$, separately, could explain the evolution of the ratio $\delta z_i / z_{\rm enc}$. Here we show that the combination of both length scales, δ and $z_{\rm enc}$, a consequence of the two-layer structure of the EZ, explains the observed behavior.

Based on our knowledge of the literature, δ and b_δ have neither been properly identified from, nor strongly supported by data from previous work, in contrast to our findings here. We speculate that this is due to the difficulty in achieving the resolution and accuracy needed to identify these two scales. Although the point of maximum buoyancy gradient is commonly taken as the height of the CBL top by studies using LES, identifying and measuring δ from LES data is possibly obscured by the significant effects of subgrid-scale fluxes in that region (Sullivan and Patton, 2011). For laboratory and atmospheric measurements, high vertical resolution is necessary to measure δ and b_δ. The low Reynolds numbers in the tank experiments by Deardorff et al. (1980), where ${\rm Re}_0 \simeq 10$, may also be a reason why both scales were not identified in those experiments, since the diffusion of both momentum and buoyancy tend to reduce the penetration depth derived from the parcel theory.

5.2 The entrainment-rate parameters

Parameterizations of the entrainment rate are usually developed from the transport equation of the mean buoyancy. Often the shape of the profiles of the mean buoyancy and the buoyancy flux is imposed, depending on the type of bulk model used (zero-order model, first-order models, general structure models) (see, e.g., Betts, 1974; Fedorovich and Mironov, 1995; Sullivan et al., 1998; Fedorovich et al., 2004b, and references therein). However, the relation between the mean entrainment rate w_e, Eq. (3.4), and the parameters that affect the mean entrainment rate (which we call '*entrainment-rate parameters*'), such as the minimum turbulent buoyancy flux and the buoyancy increment across the entrainment zone, are bulk-model dependent (Fedorovich et al., 2004b), and are thus dependent on the assumptions made about the shapes of the profiles. This dependence can be seen clearly when the entrainment rate and entrainment-rate parameters are formulated as an entrainment rate - Richardson number relation. As a case in point, the well-known -1 power law relation between the entrainment rate and convective Richardson number comes out directly from the equations when a ZOM framework is assumed although the ZOM unrealistically represents the EZ as infinitesimally thin. But for slightly more realistic representations of the EZ (first-order models and general structure models), deviations to this power law are observed (see Fedorovich et al., 2004b).

To gain an understanding of the relation between the entrainment rate and its parameters that is free from uncertainties induced by bulk model assumptions, we perform an analysis directly on the mean entrainment rate equation that is derived from the mean buoyancy transport equation, without imposing any bulk model assumption on the vertical profiles of mean buoyancy and mean buoyancy flux. An analysis based on the actual profiles can help to eliminate part of the uncertainty and arbitrariness in those definitions. In particular, we show that the two-layer structure found in the entrainment zone explains part of the disagreement among previous works. The purpose is to understand better the behavior in time of those entrainment-rate parameters, in particular, to understand how the two-layer structure discussed in the previous section affects this behavior, and thereby to provide reference data for model development.

For the particular case of the CBL growing against a linearly stratified fluid, the derivation is as follows. Integrating in space the transport equation of the mean

buoyancy deviation $\langle b\rangle - b_{\mathrm{bg}}$,

$$\frac{\partial\left(\langle b\rangle - b_{\mathrm{bg}}\right)}{\partial t} = -\frac{\partial}{\partial z}\left(\langle b'w'\rangle - \kappa\frac{\partial\langle b\rangle}{\partial z}\right), \tag{5.21}$$

from a given height $z_i(t)$ upwards and applying the Leibniz rule yields

$$\frac{\mathrm{d}}{\mathrm{d}t}\int_{z_i}^{z_\infty}\left(\langle b\rangle - b_{\mathrm{bg}}\right)\mathrm{d}z + \left[\langle b\rangle\left(z_i,t\right) - b_{\mathrm{bg}}(z_i)\right]\frac{\mathrm{d}z_i}{\mathrm{d}t} = \int_{z_i}^{z_\infty}\frac{\partial}{\partial z}\left[\kappa\frac{\partial\langle b\rangle}{\partial z} - \langle b'w'\rangle\right]\mathrm{d}z\ . \tag{5.22}$$

The analysis of the mean buoyancy as a deviation from the reference background profile b_{bg}, instead of just $\langle b\rangle$, has the advantage that the result is independent of the upper limit of integration z_∞ when it is located far enough into the nonturbulent stably stratified region. Dividing by B_0, we obtain the entrainment rate equation

$$\frac{1}{B_0}\Delta b_i\frac{\mathrm{d}z_i}{\mathrm{d}t} = A\ , \tag{5.23}$$

where

$$\Delta b_i(t) = b_{\mathrm{bg}}(z_i) - \langle b\rangle\left(z_i,t\right), \tag{5.24}$$

and

$$A(t) = A_{\mathrm{t}}(t) + A_{\mathrm{m}}(t) + A_{\mathrm{d}}(t). \tag{5.25}$$

The term Δb_i is the buoyancy deviation of the current mean buoyancy from the background reference buoyancy $b_{\mathrm{bg}}(z)$ at the height $z_i(t)$. The normalized entrainment flux, A, also known as entrainment ratio, is composed of three terms,

$$\begin{aligned} A_{\mathrm{t}}(t) &= -\frac{\langle b'w'\rangle\left(z_i\right)}{B_0}, \\ A_{\mathrm{d}}(t) &= -\frac{1}{B_0}\frac{\mathrm{d}}{\mathrm{d}t}\int_{z_i}^{z_\infty}\left(b_{\mathrm{bg}} - \langle b\rangle\right)dz, \\ A_{\mathrm{m}}(t) &= \frac{\kappa}{B_0}\frac{\partial\langle b\rangle}{\partial z}(z_i) - \mathrm{Re}_0^{-1}, \end{aligned} \tag{5.26}$$

corresponding, respectively, to the turbulent contribution, the distortion or shape contribution due to the EZ's finite thickness, and the molecular contribution (which includes the molecular contribution of the background stratification as Re_0^{-1}).

The previous equation and definitions can be applied at any CBL-top height z_i. For the rest of this section, we particularize them at $z_i = C_{\mathrm{enc},f}z_{\mathrm{enc}}$, the height of minimum buoyancy flux, to be consistent with the usual definition of the entrainment

ratio A. We use the smooth approximation $C_{\mathrm{enc},f} z_{\mathrm{enc}}$ to the instantaneous value $z_{i,f}$, valid for $z_{\mathrm{enc}}/L_0 \gtrsim 10$ (see Chapter 3 section 3.1), in order to reduce the variability in the calculation of the time derivative in the distortion or shape contribution, A_{d}; the corresponding effect on the calculated values of A and $\Delta b_{i,f}$ is less than 5%.

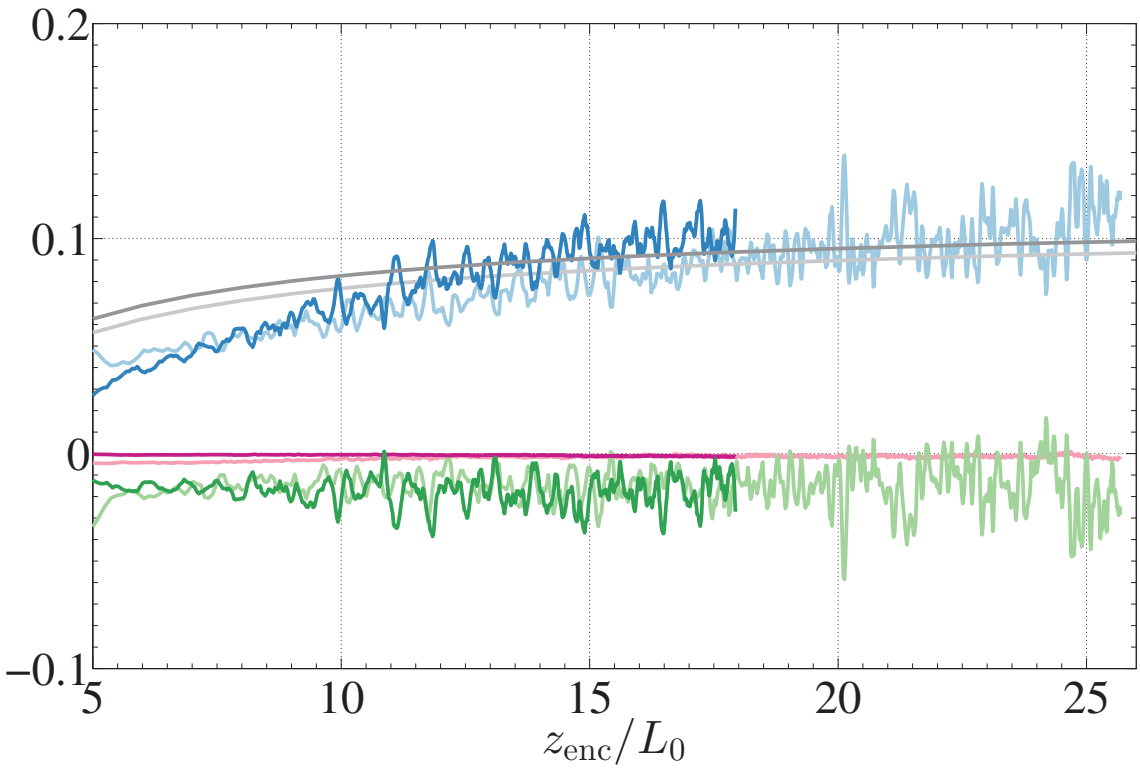

Figure 5.6: Temporal evolution of the contributions to the entrainment ratio A measured at $z_{i,f}$, Eq. (5.26): A_{t} (blue), A_{d} (green), and A_{m} (magenta). The gray line is the parameterization of A_{t} in Eq. (5.31). Light colors correspond to Re040, dark colors to Re100.

5.2.1 Contributions to the entrainment ratio A

The largest contribution to the entrainment ratio A is the turbulent term A_{t} (Fig. 5.6). On the one hand, the growth of A_{t} by about a factor of two as the CBL develops in time between $z_{\mathrm{enc}}/L_0 < 10$ and $z_{\mathrm{enc}}/L_0 > 20$ is consistent with the factor of two variation observed by Fedorovich et al. (2004b) in their LES data when the strength of the stratification is increased from the weak stratification, corresponding to the CBL state $z_{\mathrm{enc}}/L_0 \simeq 7$, to the strong stratification, corresponding to the CBL state $z_{\mathrm{enc}}/L_0 \simeq 23$ (see section 2.2). However, the DNS values $A_{\mathrm{t}} \lesssim 0.1$ at $z_{\mathrm{enc}}/L_0 \simeq 20$ are systematically smaller than the interval $0.1 - 0.15$ reported by

those authors. Since the Reynolds number effect on A_t is less than 15% (Fig. 5.6) and both cases consider a CBL growing into a linearly stratified atmosphere, this difference is likely due to subgrid-scale model effects inside the entrainment zone. On the other hand, values of A_t smaller than DNS values were observed in the convective tank experiments by Deardorff et al. (1980), despite the larger z_enc/L_0, about 50. This apparent discrepancy is possibly due to the relatively small reference Reynolds number in those tank experiments, $\mathrm{Re}_0 \simeq 10$ instead of $\mathrm{Re}_0 \simeq 100$ here, which in turn implies a relatively small Reynolds number inside the entrainment zone in the tank experiments and a tendency to have a thicker EZ and a less pronounced minimum in the profile of the turbulent buoyancy flux. Differences in Prandtl numbers by an order of magnitude could also explain the apparent discrepancy, since Prandtl number effects can be substantial at low Reynolds numbers (Jonker et al., 2012).

The second contribution to the entrainment ratio is the distortion or shape term A_d. Its value is relatively small compared to the contribution of the turbulent buoyancy flux A_t. On average, we observe

$$A_\mathrm{d} \simeq -0.02 \,, \tag{5.27}$$

whereas $A_\mathrm{t} \simeq 0.1$. This result is in contrast with the conclusion of Sullivan et al. (1998), which states that both terms are comparable to each other for CBLs with relatively thick EZ. We take note, however, that the buoyancy term $\Delta b_{i,f}$ in Eq. (5.23) when particularized at $z_{i,f}$, and thereby A_d, are defined here differently, namely, as a local deviation with respect to the background profile $b_\mathrm{bg}(z)$, and not as a global buoyancy δb_i increment across the whole entrainment zone (Fig. 5.7).

Another difference of A_d from A_t is that the distortion or shape term A_d is approximately constant in time (Fig. 5.6). This steady behavior can be understood from the two-layer vertical structure of the EZ that is described in the previous section. The integral in Eq. (5.26) can be split into two integrals: one integral from $z_{i,f}$ to $z_{i,g}$ and another integral from $z_{i,g}$ to z_∞. It is then easy to show from the scalings derived in the previous section that this second contribution from the upper EZ sublayer continuously decreases, whereas the first contribution from the lower EZ sublayer is indeed constant in time. This latter contribution, according to Fig. 5.6, seems to dominate the evolution of A_d.

Last, the molecular contribution to the entrainment ratio, A_m, is already negligibly small for the Reynolds numbers achieved in this work (Fig. 5.6).

5.2.2 The local buoyancy increment $\Delta b_{i,f}$

We have learned before that the contribution to the entrainment ratio A from the finite EZ thickness through the distortion term $A_{\rm d}$ is relatively small, about 20% or less. However the finite EZ thickness still remains important because the smooth variation of the mean buoyancy inside the entrainment zone over a finite EZ thickness determines a local buoyancy increment $\Delta b_{i,f}$ in Eq. (5.23) that is significantly smaller than the global buoyancy increment δb_i across the whole entrainment zone (see Fig. 5.7). We can quantify this difference as follows.

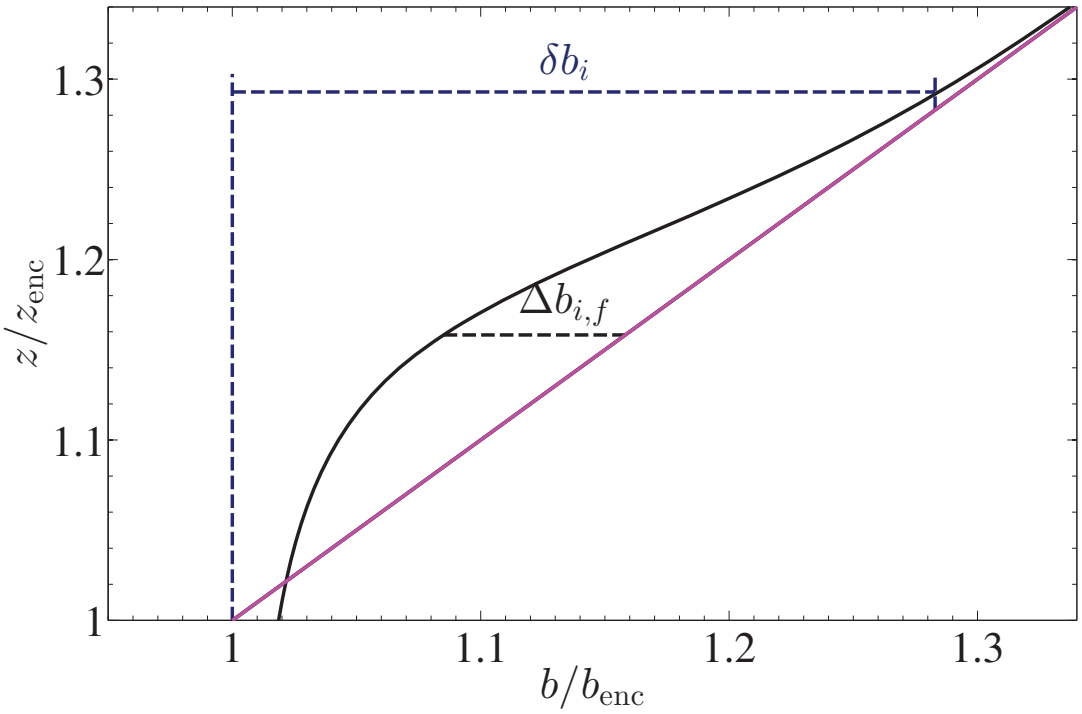

Figure 5.7: Sketch illustrating the difference between the local buoyancy increment $\Delta b_{i,f}$, Eq. (5.24) evaluated at $z_i = z_{i,f}$, and the global buoyancy difference δb_i across the whole entrainment zone, Eq. (5.19).

As a first approximation, we can assume that the mean buoyancy inside the lower EZ sublayer, in particular $\langle b \rangle (z) - b_{\rm enc}$, tends towards a steady profile when normalized with $\langle b \rangle (z_{i,g}) - b_{\rm enc}$. The reason is that the lower EZ sublayer is relatively well mixed and approximately quasi-steady in the equilibrium entrainment regime (see Chapter 3 section 3.6): the top and bottom values $\langle b \rangle (z_{i,g})$ and $\langle b \rangle (z_{i,0}) \simeq b_{\rm enc}$ (see Chapter 3 section 3.2) vary in time, but turbulence mixes the buoyancy across that

region relatively fast. Hence, we can hypothesize that

$$\langle b\rangle\,(z_{i,f}) - b_{\rm enc} = c_{b3}[\langle b\rangle\,(z_{i,g}) - b_{\rm enc}]\;, \tag{5.28}$$

since the height of minimum buoyancy flux $z_{i,f}$ is approximately in the middle of the lower EZ sublayer (see Fig. 5.1b and Fig. 5.4). Figure 5.5e supports this relation for $z_{\rm enc}/L_0 > 10-15$, the constant of proportionality being $c_{b3} \simeq 0.45$ (see Table 5.1).

Combining this result with Eq. (5.14) and Eq. (5.15) yields

$$\Delta b_{i,f}/b_{\rm enc} = \beta_0 - \beta_1(\delta/z_{\rm enc})\;, \tag{5.29}$$

where

$$\begin{aligned} \beta_0 &= C_{{\rm enc},f} - 1 - c_{b3}(1-c_{b_1})(C_{{\rm enc},g}-1)\;,\\ \beta_1 &= c_{b3}(1-c_{b_1})\;, \end{aligned} \tag{5.30}$$

and $\delta/z_{\rm enc}$ is given by Eq. (5.7). Based on the constants in Table 3.1 and Table 5.1, $\beta_0 \simeq 0.086$ and $\beta_1 \simeq 0.27$. Comparing with δb_i, Eq. (5.19), we observe that $\Delta b_{i,f}$ tends asymptotically towards a constant fraction $\simeq 0.26$ of δb_i. However, the ratio $\Delta b_{i,f}/\delta b_i$ increases in time by a factor of two during the intermediate states $z_{\rm enc}/L_0 \simeq 10-26$, when the contribution of δ to the EZ structure is not negligible.

5.2.3 Asymptotic behavior of A

Substituting Eq. (5.29) in Eq. (5.23) and using Eq. (3.5), we obtain an explicit expression for the entrainment ratio in the form

$$A_{\rm t} = \gamma_0 - \gamma_1(\delta/z_{\rm enc})\;, \tag{5.31}$$

where

$$\begin{aligned} \gamma_0 &= C_{{\rm enc},f}\beta_0 - A_{\rm d}\;,\\ \gamma_1 &= C_{{\rm enc},f}\beta_1\;. \end{aligned} \tag{5.32}$$

From the previous section, we obtain the estimates $\gamma_0 \simeq 0.12$ and $\gamma_1 \simeq 0.31$. The good agreement of this parameterization with the DNS data (Fig. 5.6) is mainly a consequence of the good prediction of the local buoyancy increment by Eq. (5.29), since Eq. (5.31) follows from the exact relation, Eq. (5.23). Hence, the evolution of A in time is a consequence of the evolution of the two-layer structure of the EZ. We can also infer that, for a CBL penetrating into a linearly stratified atmosphere, $A_{\rm t}$

tends towards an asymptotic value $\simeq 0.12$, within an accuracy of $\simeq 15\%$ (Table 5.1). This value is significantly below the entrainment ratio value $\simeq 0.2$ that works well for predicting the mean entrainment rate using the zero-order bulk model. However, as stated in the introduction and emphasized by Fedorovich et al. (2004b), there is no inconsistency between both results because the zero-order model is not designed to capture the effects of the EZ's finite thickness.

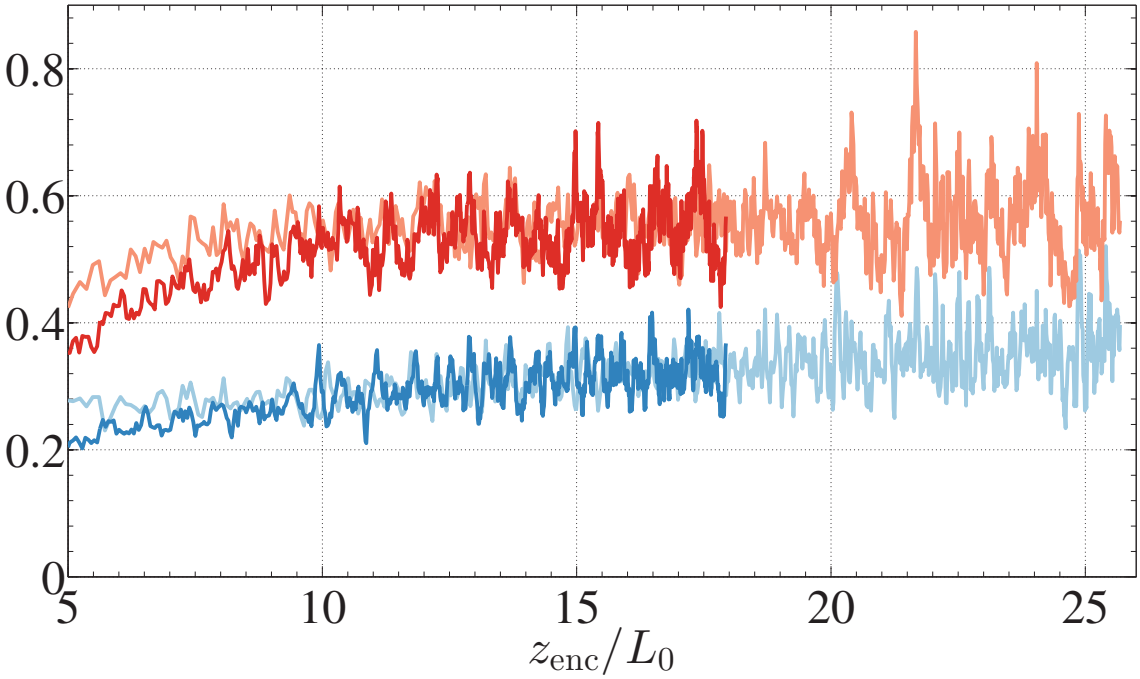

Figure 5.8: Temporal evolution of the normalized terms of the local budget equation of turbulence kinetic energy, Eq. (3.15), $\varepsilon/\left(-\partial T/\partial z\right)$ (red) and $-\left\langle b'w'\right\rangle/\left(-\partial T/\partial z\right)$ (blue) evaluated at the height of minimum buoyancy flux $z_{i,f}$. Light colors correspond to Re040, dark colors to Re100.

The evolution of A_{t} according to Eq. (5.31) can be interpreted in terms of the dominant balance in the turbulence kinetic energy equation Eq. (3.15), particularized at $z_{i,f}$, between the turbulent transport, and the turbulent buoyancy flux and the viscous dissipation (Fig. 5.8). The three terms are expected to follow an inviscid scaling in terms of the local integral length and velocity scales of the turbulence. Since $z_{i,f}$ is still relatively close to the upper EZ sublayer for the interval $z_{\mathrm{enc}}/L_0 \simeq 10-26$ (see Fig. 5.1b), we can also anticipate that the integral length and velocity scales that are observed at $z_{i,f}$ are a combination of the corresponding scales within each of the two EZ sublayers within that interval of time. Although the velocity scales in both EZ sublayers are proportional to the convective velocity, the length scales are different: a constant fraction of z_{enc} in the lower EZ sublayer and δ in the upper

EZ sublayer. If we propose

$$-\langle b'w'\rangle(z_{i,f}) = \gamma_0 \frac{w_*^3}{z_{\rm enc} + (\gamma_1/\gamma_0)\delta} \,, \tag{5.33}$$

and expand the fraction in terms of the small number $(\gamma_1/\gamma_0)(\delta/z_{\rm enc})$, we recover Eq. (5.31) as a first approximation. Hence, the combined effect of the two-layer structure on the local energetics inside the entrainment zone, Eq. (3.15), including the turbulent buoyancy flux, can be interpreted in terms of an average length scale proportional to $z_{\rm enc} + (\gamma_1/\gamma_0)\delta$, where $\gamma_1/\gamma_0 \simeq 1.3$. As the CBL develops in time and the ratio $\delta/z_{\rm enc}$ decreases, the upper EZ sublayer recedes towards $z_{i,g}$ and the length scale that remains effective at $z_{i,f}$ is that of the lower EZ sublayer, namely, $z_{\rm enc}$.

5.2.4 The entrainment rate - Richardson number power law

The entrainment rate equation, Eq. (5.23), is sometimes expressed as a relation between a nondimensional or normalized mean entrainment rate $E = w_{\rm e}/w_*$ and a Richardson number Ri. Different power laws $E \propto {\rm Ri}^{-n}$ have been proposed in the literature, although scatter in the data and uncertainty in the exponent n still prevent us from reaching a definitive conclusion, in particular for intermediate values of Ri (see, e.g., Zilitinkevich, 1991; Fedorovich et al., 2004b; Jonker et al., 2012, and references therein). For the case of a CBL growing into a linearly stratified fluid, the different choices for the CBL-top height $z_{i,\xi}$ that is used in the definition of $w_{\rm e}$ and w_* can only explain a relatively small variation in the proportionality coefficient of this relation, since all of these heights become commensurate with each other beyond $z_{\rm enc}/L_0 \simeq 5 - 10$ (Chapter 3 section 3.1). In contrast, the particular buoyancy scale that is used to define the Richardson number can affect the functional relation between E and Ri more significantly. This section is devoted to this issue.

Conventionally, a convective Richardson number is defined as

$${\rm Ri}_* = \frac{z_{\rm enc}\delta b_i}{w_*^2} \,, \tag{5.34}$$

where δb_i, Eq. (5.19), is a measure of the buoyancy variation across the whole entrainment zone (Deardorff et al., 1980; Sullivan et al., 1998; Fedorovich et al.,

2004b). Combining this definition with Eq. (3.5), we obtain the relation

$$E = \alpha \mathrm{Ri}_*^{-1} \ , \tag{5.35}$$

where

$$\alpha = C_{\mathrm{enc},f} \left[C_{\mathrm{enc},g} - 1 + (\delta / z_{\mathrm{enc}}) \right] \ . \tag{5.36}$$

[The prefactor $C_{\mathrm{enc},f}$ in the expression above results from calculating the entrainment velocity at $z_{i,f}$ and computing w_* according to Eq. (2.11) – as already mentioned, other choices vary this prefactor merely by a constant of order one and its particular value is irrelevant for the discussion that follows.] This analytic result has two important implications.

First, asymptotically, the proportionality coefficient $\alpha(t)$ approaches $\alpha_0 = C_{\mathrm{enc},f}(C_{\mathrm{enc},g}-1) \simeq 0.28$ and hence $E \propto \mathrm{Ri}_*^{-1}$. This is one of the power laws proposed in the literature based on the estimate $\langle b'w' \rangle (z_i) \propto w_*^3 / z_i \simeq B_0$ for the turbulent flux within the entrainment zone and the approximation $w_\mathrm{e} \delta b_i \simeq - \langle b'w' \rangle (z_i)$ (see, e.g., Fernando, 1991, for more details). However, for the interval $\mathrm{Ri}_* \simeq 8 - 23$ ($z_{\mathrm{enc}}/L_0 \simeq 10 - 26$) considered in this study, which is representative of atmospheric conditions (see Chapter 2 section 2.2), the evolution of the normalized mean entrainment rate E deviates from that asymptotic limit: a steeper curve is observed in Fig. 5.9, in agreement with previous results that suggested exponents n larger than 1 (Turner, 1973; Deardorff et al., 1980; Fedorovich et al., 2004b). Our results indicate that these deviations stem from the effect that the upper EZ sublayer has on the entrainment-rate parameters, specifically, the term $\delta / z_{\mathrm{enc}}$ in Eq. (5.36). When we express $\delta / z_{\mathrm{enc}}$ as a function of Ri_* using Eq. (5.19),

$$\delta / z_{\mathrm{enc}} = \frac{c_\delta^2}{2 \mathrm{Ri}_*} \left\{ 1 + \left[4 c_\delta^{-2} (C_{\mathrm{enc},g} - 1) \mathrm{Ri}_* + 1 \right]^{1/2} \right\} \ , \tag{5.37}$$

we obtain the approximation

$$E \simeq (\alpha_0 + \alpha_1 \mathrm{Ri}_*^{-1/2} + \alpha_2 \mathrm{Ri}_*^{-1}) \mathrm{Ri}_*^{-1} \ , \tag{5.38}$$

valid for $\mathrm{Ri}_* \gg c_\delta^2 / [4(C_{\mathrm{enc},g} - 1)] \simeq 0.28$, where

$$\begin{aligned} \alpha_0 &= C_{\mathrm{enc},f} (C_{\mathrm{enc},g} - 1) \ , \\ \alpha_1 &= C_{\mathrm{enc},f} (C_{\mathrm{enc},g} - 1)^{1/2} c_\delta \ , \\ \alpha_2 &= C_{\mathrm{enc},f} c_\delta^2 / 2 \ . \end{aligned} \tag{5.39}$$

From the constants in Table 3.1 and Table 5.1, we obtain $\alpha_0 \simeq 0.28$, $\alpha_1 \simeq 0.29$ and $\alpha_2 \simeq 0.16$. Equation (5.38) helps to explain the different scalings $E \propto \mathrm{Ri}_*^{-n}$, $1 \leq n < 2$, found in the literature for intermediate values of the convective Richardson number Ri_*. Equation (5.38) also allows us to estimate the error in predicting E according to $E \simeq \alpha_0 \mathrm{Ri}_*^{-1}$: even at the strong stratification limit $z_{\mathrm{enc}}/L_0 \simeq 50$ ($\mathrm{Ri}_* \simeq 50$), this error is still larger than 10%. The question still remains, though, whether we could interpret Eq. (5.38) and the effect of the upper EZ sublayer on α in terms of some of the mixing mechanisms that have been proposed to play a role at the entrainment zone, in particular those associated with the interaction of turbulence and gravity waves (Carruthers and Hunt, 1986; Fernando, 1991).

It is worth noting that an alternative definition of a Richardson number as $\mathrm{Ri}_{N,\xi} = N^2 z_{i,\xi}^2 / w_{*,\xi}^2$, where $w_{*,\xi} = (B_0 z_{i,\xi})^{1/3}$, leads to the exact relation $w_{e,\xi}/w_{*,\xi} = C_{\mathrm{enc},\xi}^2 \mathrm{Ri}_{N,\xi}^{-1}$ once $z_{i,\xi}$ becomes proportional to z_{enc}, which occurs at about $z_{\mathrm{enc}}/L_0 \simeq 10$ (see Chapter 3 section 3.1). The range $z_{\mathrm{enc}}/L_0 \simeq 10 - 26$ considered in our study corresponds to $N^2 z_{\mathrm{enc}}^2 / w_*^2 \simeq 21 - 77$. Hence, a very clear relation $E \propto \mathrm{Ri}^{-1}$ appears much earlier than when using the convection Richardson number Ri_*. However, $\mathrm{Ri}_{N,\xi}$ does not reflect the evolution of the local dynamics inside the EZ during the intermediate range of atmospheric Richardson numbers considered in this study but just the CBL thickness.

Last, by comparing cases Re040 and Re100 we also observe in Fig. 5.9 that Reynolds number effects in the functional relation $E = f(\mathrm{Ri}_*)$ are negligibly small beyond $\mathrm{Re}_* \simeq 10^3$, which is the value attained in simulation Re040 at $z_{\mathrm{enc}}/L_0 \simeq 10$. This result agrees with previous data (see, e.g., Fernando and Little, 1990; Jonker and Jimnez, 2014). [Prandtl numbers greater than 1, not considered in this study, might affect this mixing transition into an inviscid behavior (see, e.g., Jonker et al., 2012)].

The second implication of Eq. (5.36) is that the proportionality coefficient α is different from the entrainment ratio A. It is not only different by a proportionality constant of order one, but it also evolves differently in time, since $A(t)$ increases (Fig. 5.6) and $\alpha(t)$ decreases (since δ/z_{enc} decreases). If desired, a functional relation in which the proportionality coefficient is the entrainment ratio $A(t)$ can be obtained by rewriting Eq. (5.23) as

$$E = A \mathrm{Ri}_{i,f}^{-1} \, . \tag{5.40}$$

Similar to the previous observation, a strong deviation during the interval $z_{\mathrm{enc}}/L_0 \simeq 10 - 26$ from the asymptotic behavior $E \propto \mathrm{Ri}_{i,f}^{-1}$ is exhibited in Fig. 5.9. This deviation is again due to the upper EZ sublayer, in this case, due to its effect on the

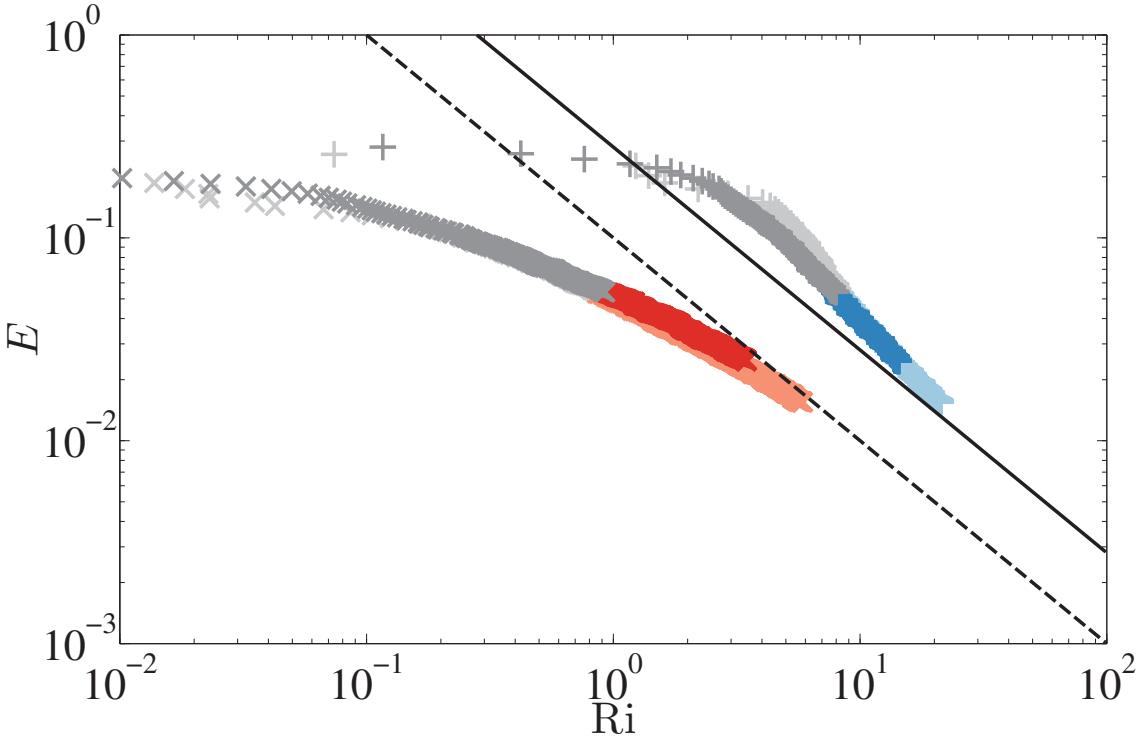

Figure 5.9: Scatter plot of the normalized entrainment rate $E = w_e/w_*$ against the Richardson numbers $\mathrm{Ri}_* = z_{\mathrm{enc}}\delta b_i/w_*^2$ and $\mathrm{Ri}_{i,f} = z_{\mathrm{enc}}\Delta b_{i,f}/w_*^2$. Gray denotes data from earlier time $z_{\mathrm{enc}}/L_0 < 10$. For $z_{\mathrm{enc}}/L_0 \geq 10$, blue corresponds to Ri_* and red to $\mathrm{Ri}_{i,f}$. The solid black line is $0.28\mathrm{Ri}_*^{-1}$, based on the asymptotic behavior of $\alpha(t)$ towards 0.28. The dashed black line is $0.10\mathrm{Ri}_{i,f}^{-1}$, based on the asymptotic behavior of $A(t)$ towards 0.10. Light colors correspond to Re040, dark colors to Re100.

evolution of A towards its asymptotic value, Eq. (5.31). However, the Richardson number

$$\mathrm{Ri}_{i,f} = \frac{z_{\mathrm{enc}}\Delta b_{i,f}}{w_*^2} \tag{5.41}$$

is now based on the local buoyancy increment $\Delta b_{i,f}$ characterizing the entrainment rate equation at $z_{i,f}$, and not on the buoyancy increment δb_i as used in the definition of the convective Richardson number Ri_*. Hence, Eq. (5.23), which is derived from first principles, reduces the degree of freedom to choose the proportionality coefficient and the Richardson number in the entrainment rate equation $E \propto \mathrm{Ri}^{-n}$: if we choose the proportionality coefficient to be the usual entrainment ratio A defined as Eq. (5.25), then the exact equation imposes a corresponding Richardson number defined with a local buoyancy increment $\Delta b_{i,f}$. On the other hand, if we simply relate the normalized mean entrainment rate E to the convective Richardson number Ri_*, then the exact equation imposes a corresponding proportionality coefficient α that is different from the entrainment ratio A.

On the convective Richardson number

In the previous section, we showed how different Richardson numbers can be defined and be related to the entrainment rate. However, none of them quantifies the balance of kinetic and potential energy at the EZ predicted by parcel theory, which we have shown to be quantified by Ri_δ (Eq. 5.12), a Richardson number that is quasi-steady and of order one. Because of how Ri_* is defined, interpreting it as a balance of potential and kinetic energy is problematic, especially in the context of local entrainment. This reflects on the seemingly paradoxical behavior of the CBL being able to continue on growing (although slower) and still maintain an entrainment rate similar to the encroachment rate, even when the convective Richardson number increases in time beyond 10. We therefore try to understand the relevance of the convective Richardson number with respect to entrainment at the EZ.

Recall that the basic ingredients for entrainment at a density interface are a characteristic velocity scale, a characteristic length scale, and a characterization of the opposing buoyancy force. At the entrainment zone of the CBL, we have shown that the characteristic velocity is proportional to the convective velocity. However, due to the multiplicity of length and buoyancy scales, it is unclear which length scale and buoyancy scale are appropriate. The convective Richardson number has the CBL thickness as the length scale. Indeed, for the case we considered in this study, z_i is the relevant length scale for the mean CBL growth since the growth rate of the encroachment scale already characterizes the growth rate of the CBL and the details of entrainment do not seem to affect the entrainment rate. However, neither the entire length scale z_i nor a constant fraction of it characterizes the length scale of penetration depth of the thermals at the entrainment zone (see section 5.1.1).

Another questionable aspect of the convective Richardson number definition is the use of δb_i to characterize the opposing buoyant force. As already mentioned before, the increase of the buoyancy increment δb_i in time is not the reason why w_e is decreasing; the deceleration of entrainment rate is simply due to the farther distance that the thermals have to travel while the input of energy remains constant. Besides, the buoyancy increment δb_i cannot become too strong since the CBL we consider has a continuous buoyancy input at the surface that regulates this buoyancy difference at the EZ. Therefore, the increase of Ri_* in time is mainly due to the increase in z_i and not due to an increasingly steeper δb_i. Consequently, Ri_* can be thought of as a proxy for the independent variable time tN, similar to z_enc/L_0. In contrast, the situation would be different if turbulence is only mechanically driven: as the

entrainment zone moves farther away from the momentum source (e.g. an oscillating grid) the buoyancy difference between the turbulent and the nonturbulent region can become steep because buoyancy flux is solely coming from entrainment (see Perera et al., 1994). In this case, the convective Richardson number mainly increases due to the steepening of δb_i.

To reconcile the over-all picture given by an increasing Ri_* to the quasi-steady Richardson number Ri_δ, we point out that δ is not directly dictated by z_i and is thus unaware of the increasing distance the penetrating thermals have to travel and the increasing time for these penetrations to occur. The quasi-steady behavior of Ri_δ only reflects the local balance of potential energy and kinetic energy for the penetrating thermals. As for Ri_*, it seems appropriate to interpret it as the over-all Richardson number as it takes into account the development of the large circulation in time, which we expound on by writing it as

$$\mathrm{Ri}_* = \frac{\delta b_i}{b_*} = \frac{t_*}{t_{\delta b_i}} \,, \tag{5.42}$$

where $t_* = z_{\mathrm{enc}}/w_*$ and $t_{\delta b_i} = w_*/\delta b_i$. The first ratio in Eq. (5.42) is comparing the mean buoyancy increment over the EZ to the convective buoyancy that characterizes the buoyancy fluctuations in the mixed layer. In time, δb_i is slowly increasing while b_* is decreasing relatively faster in time. The latter implies that the buoyancy surplus of the more buoyant thermals decreases with respect to the mean due to convective mixing. However, this does not mean that the thermals will overshoot less since the velocity of the thermals, which is proportional to w_*, is increasing. The second ratio simply compares the time scale of undulations at the EZ $t_{\delta b_i}$ and the convective time scale t_*. As the CBL grows, the undulation time scale is slowly decreasing while t_* is increasing relatively faster. We picture this as the large eddies taking a longer time to overturn and in contrast, the undulations at the entrainment zone occurring fast enough such that the entrainment zone can return to equilibrium. The convective Richardson number therefore compares the scales of convection to the scales of the undulations at the entrainment zone and is different from the basic definition of the Richardson number that compares the potential energy and kinetic energy at the entrainment zone.

6 Summary and Conclusions

We used direct numerical simulation to investigate the fully-developed regime of a convective boundary layer with constant surface buoyancy flux B_0 growing into a linearly stratified fluid characterized by a positive and constant buoyancy gradient N^2. The ratio between the CBL height z_i and the reference Ozmidov scale $L_0 = (B_0/N^3)^{1/2}$ considered in the simulations covers an interval $5 - 26$ and therefore includes typical atmospheric values, for which $L_0 \simeq 40 - 130$ m according to the typical estimates $N \simeq 0.6 - 1.8 \times 10^{-2}$ s^{-1} and $B_0 \simeq 0.3 - 1.0 \times 10^{-2}$ m^2 s^{-3}. The only difference with real conditions is the reference buoyancy Reynolds number $B_0/(\nu N^2)$, which is 10^2 in the DNS as compared to 10^6 in the atmosphere. In terms of the convective Reynolds number $\mathrm{Re}_* = w_* z_i/\nu$, we achieved values nearing 10^4, whereas the atmospheric values are approximately 10^8.

We have shown in Chapter 3 that, in spite of this moderate Reynolds number, the scale separation we attain is sufficient for the CBL to exhibit Reynolds number similarity in the statistics of interest. In particular, the following CBL features are reproduced:

- The CBL thickness scales with the encroachment height.
- Vertical profiles of mean and variance of buoyancy and velocity exhibit self-similar behavior in time within the well-mixed layer when normalized by the convective scales, and are comparable to profiles from measurements and LES results.
- Vertical profiles of higher-order moments of the vertical velocity exhibit Reynolds number similarity within the well-mixed layer.
- Turbulence kinetic energy budget profiles exhibit the expected shapes and show self-similar behavior within the well-mixed layer.
- The CBL has developed into the equilibrium entrainment regime, wherein the convective motions are faster than the growth of the CBL.

The aforementioned results validate the use of DNS for studying the surface layer and the entrainment zone, where LES is limited. Using DNS data, we addressed some questions regarding the surface layer and the entrainment zone. Concerning the surface layer, we addressed the questions:

- Do statistics at the surface layer for flows in pure free convection obey classical similarity scaling?
- Does stratification, and therefore the outer scale, affect the surface layer statistics? If so, how?

The answer to the first question depends on the statistic. In particular, we observe agreement with the classical similarity scaling for the mean buoyancy profile $\langle b \rangle(z)$ of the CBL since it varies as $\langle b \rangle^+ = \langle b \rangle / b_0 \propto (z^+)^{-4/3}$ beyond 10 wall diffusive units z_0, where $b_0 = (B_0^2/z_0)^{1/3}$. However, the root-mean-square of the buoyancy fluctuations is better described by $b^+_{\mathrm{rms}} \propto (z^+)^{-1/2}$, and that of the vertical velocity fluctuations by $w^+_{\mathrm{rms}} \propto \log(z^+)$, instead of the $-1/3$ and $1/3$ power laws, respectively, that are predicted by classical similarity theory. These deviations are clearly observed in the absence of mean wind, which contradicts the typical explanation for the deviations of atmospheric observations from the predictions of classical similarity theory. Although for the DNS data, the effects of moderate Reynolds numbers cannot be completely ruled out.

We check whether these deviations are due to penetration of outer layer scales into the inner layer by switching off stratification and comparing the CBL to the neutrally-stratified case (the second question). The answer to the second question is **yes**. In particular, we observe that although the neutral stratification vertical velocity r.m.s. w^+_{rms} also varies logarithmically with height, $w^+_{\mathrm{rms}} \propto \log(z^+)$, the coefficients are different. Moreover, the buoyancy-related profiles are different to those of the stably stratified case, namely, $\langle b \rangle^+ \propto (z^+)^{-2}$ and $b^+_{\mathrm{rms}} \propto (z^+)^{-3/2}$.

By doing a spectral analysis, we observe that the vertical structure of the radial spectra of velocity components and buoyancy are dependent on the presence or absence of stratification even within the inner layer. This dependence is interpreted as a direct influence of outer layer large-scale motions on the inner layer, which then confirms previous suggestions and proves that the assumptions behind classical similarity theory are wrong. An implication of this is that the observed dependence on the outer stratification strength, or, equivalently, on the state of development

of the convective boundary layer, contribute to the scatter of the atmospheric data that is often attributed to other effects like horizontal wind.

Concerning the entrainment zone, we addressed the questions:

- Does stratification impose a characteristic length scale inside the EZ that is different from the CBL thickness?
- Does the EZ vertical structure affect the functional relationship between the mean entrainment rate $E = (1/w_*)dz_i/dt$ and a convective Richardson number?

The answer to the first question is **yes**. In particular, we find that

- The entrainment zone is better described by two overlapping sublayers (an upper and a lower), each with a different characteristic vertical length scale.
- The upper EZ sublayer is the one directly affected by the stratification N^2, which reflects on the characteristic length scale δ that is observed to vary proportionally to the penetration depth of thermals, w_*/N, that is predicted by parcel theory.
- δ is also the length scale of turbulence in the upper EZ sublayer, meaning the dissipation rate at the upper EZ sublayer $\varepsilon \propto w_*^3/\delta$.
- The lower EZ sublayer is only indirectly affected by the stratification, and is better characterized by the CBL thickness z_i.

Correspondingly, different buoyancy scales are found, which reflects on the buoyancy fluctuations being a combination of the buoyancy increment associated with the penetrating thermal, and the buoyancy increment associated with the non-thermal regions that mainly retain the original stratification N^2. We provide parameterizations for the characteristic scales, which allows for the reconstruction of the vertical profiles of the mean and variance of the buoyancy within the EZ at any time within the equilibrium entrainment regime.

These findings imply a justification for considering a second turbulence length scale at the EZ for turbulence models, one that is different from z_i and behaves according to the parcel theory prediction. This multiplicity of scales inside the EZ also explains

difficulties found in previous analyses that considered the entrainment zone as a single layer with vertical profiles characterized by a single set of characteristic scales.

Regarding the second EZ question, the answer is **yes**. By analyzing the terms of an exact equation for the entrainment rate using DNS data, we found that

- The direct contribution of the EZ finite thickness to the entrainment ratio A through the distortion term is small.
- The indirect contribution of the finite thickness is to decrease the local buoyancy increment associated with the exact equation, which then compensates for the small entrainment ratio A.
- Deviation from the power-law with exponent -1 under typical atmospheric conditions is explained by the effect of the upper EZ sublayer on the buoyancy increment across the whole EZ and on the corresponding proportionality coefficient α.
- As the upper EZ sublayer becomes thinner relative to the CBL, α asymptotes to a constant and the functional relation between the normalized mean entrainment rate E and the convective Richardson number Ri_* approaches a power law behavior with exponent -1.

This finding shows that deviations from the -1 power law are normal for typical atmospheric values of the convective Richardson number and the -1 power law may not be relevant as it requires very large values of the convective Richardson number that are atypical in the atmosphere. Moreover, this finding shows that the deviation is apparently not due to the radiation of gravity waves, confirming previous indications. We noted also that the proportionality coefficient α evolves in time differently from the entrainment ratio A, implying that an inappropriate $\{A, \mathrm{Ri}\}$ pair could partially explain the failure of previous attempts to relate E to a certain Richardson number, Ri, through a power law.

In sum, we showed in this work that DNS is emerging as a feasible and sensible alternative tool for understanding the details of the problematically thin regions, such as the surface layer and the entrainment zone, and will increasingly be so as computing power continues to increase.

References

Adrian, R. J. (1996). Variation of temperature and velocity fluctuations in turbulent thermal convection over horizontal surfaces. *International Journal of Heat and Mass Transfer*, **39**(11), 2303–2310.

Adrian, R. J., R. T. D. S. Ferreira and T. Boberg (1986). Turbulent thermal convection in wide horizontal layers. *Exp. Fluids*, **4**, 121–141.

Akylas, E. and M. Tombrou (2005). Interpolation between BusingerDyer formulae and free convection forms: a revised approach. *Bound.-Layer Meteor.*, **115**(3), 381–398.

Ball, F. K. (1960). Control of inversion height by surface heating. *Q. J. Roy. Meteorol. Soc.*, **86**(370), 483–494.

Batchelor, G. K. (1967). An Introduction to Fluid Dynamics. Cambridge University Press.

Beljaars, A. C. M. (1994). The parametrization of surface fluxes in large-scale models under free convection. *Q. J. Roy. Meteorol. Soc.*, **121**, 255–270.

Betts, A. K. (1974). Reply to comment on the paper "Non-precipitating cumulus convection and its parameterization". *Q. J. Roy. Meteorol. Soc.*, **100**(425), 469–471.

Bretherton, C., M. MacVean, P. Bechtold, A. Chlond, W. Cotton, J. Cuxart, H. Cuijpers, M. Mhairoutdinov, B. Kosovic, D. Lewellen *et al.* (1999). An intercomparison of radiatively driven entrainment and turbulence in a smoke cloud, as simulated by different numerical models. *Q. J. Roy. Meteorol. Soc.*, **125**(554), 391–423.

Buckingham, E. (1914). On physically similar systems: illustrations of the use of dimensional equations. *Phys. Rev.*, **4**, 345–376.

Businger, J. A. (1973). A note on free convection. *Bound.-Layer Meteor.*, **4**, 323–326.

Businger, J. A., J. C. Wyngaard, Y. Izumi and E. F. Bradley (1971). Flux-Profile Relationships in the Atmospheric Surface Layer. *J. Atmos. Sci.*, **28**(2), 181–189.

Carruthers, D. J. and J. C. R. Hunt (1986). Velocity fluctuations near an interface between a turbulent region and a stably stratified layer. *J. Fluid Mech.*, **165**(-1), 475–501.

Carson, D. and F. Smith (1975). Thermodynamic Model for the Development of a Convectively Unstable Boundary Layer. In *Advances in Geophysics*, Vol. 18, pp. 111–124. Elsevier.

Carson, D. J. (1973). The development of a dry inversion-capped convectively unstable boundary layer. *Q. J. Roy. Meteorol. Soc.*, **99**(421), 450–467.

Castaing, B., G. Gunaratne, F. Heslot, L. Kadanoff, A. Libchaber, S. Thomae, X.-Z. Wu, S. Zaleski and G. Zanetti (1989). Scaling of hard thermal turbulence in Rayleigh-Bnard convection. *J. Fluid Mech.*, **204**(-1), 1.

Chillà, F. and J. Schumacher (2012). New perspectives in turbulent Rayleigh-Bénard convection. *Eur. Phys. J. E*, **35**(58), 1–25.

Chung, D. and G. Matheou (2012). Direct numerical simulation of stationary homogeneous stratified sheared turbulence. *J. Fluid Mech.*, **696**, 434–467.

Coleman, G. (1999). Similarity statistics from a direct numerical simulation of the neutrally stratified planetary boundary layer. *J. Atmos. Sci.*, **56**(6), 891900.

Coleman, G. N., J. H. Ferziger and P. R. Spalart (1994). A numerical study of the convective boundary layer. *Bound.-Layer Meteor.*, **70**(3), 247–272.

de Roode, S., P. Duynkerke and H. Jonker (2004). Large-eddy simulation: How large is large enough? *J. Atmos. Sci.*, **61**(4), 403–421.

Deardorff, J., G. Willis and D. Lilly (1969). Laboratory investigation of non-steady penetrative convection. *J. Fluid Mech.*, **35**(part 1), 731.

Deardorff, J. W. (1970). Convective velocity and temperature scales for the unstable planetary boundary layer and for Rayleigh convection. *J. Atmos. Sci.*, **27**, 1211–1213.

Deardorff, J. W. (1972). Numerical Investigation of Neutral and Unstable Planetary Boundary Layers. *J. Atmos. Sci.*, **29**(1), 91–115.

Deardorff, J. W. (1973). The Use of Subgrid Transport Equations in a Three-Dimensional Model of Atmospheric Turbulence. *Journal of Fluids Engineering*, **95**(3), 429.

Deardorff, J. W. (1979). Prediction of Convective Mixed-Layer Entrainment for Realistic Capping Inversion Structure. *J. Atmos. Sci.*, **36**(3), 424–436.

Deardorff, J. W. (1980a). Cloud top entrainment instability. *J. Atmos. Sci.*, **37**, 131–147.

Deardorff, J. W. (1980b). Stratocumulus-capped mixed layers derived from a three-dimensional model. *Bound.-Layer Meteor.*, **18**(4), 495–527.

Deardorff, J. W. and G. E. Willis (1967). Investigation of turbulent thermal convection between horizontal plates. *J. Fluid Mech.*, **28**, 675–704.

Deardorff, J. W. and G. E. Willis (1985). Further results from a laboratory model of the convective planetary boundary layer. *Bound.-Layer Meteor.*, **32**, 205–236.

Deardorff, J. W., G. E. Willis and B. H. Stockton (1980). Laboratory studies of the entrainment zone of a convectively mixed layer. *J. Fluid Mech.*, **100**, 41–64.

Dimotakis, P. E. (2000). The mixing transition in turbulent flows. *J. Fluid Mech.*, **409**, 69–98.

Driedonks, A. G. M. (1982). Models and observations of the growth of the atmospheric boundary layer. *Bound.-Layer Meteor.*, **23**(3), 283–306.

du Puits, R., L. Li, C. Resagk, A. Thess and C. Willert (2014). Experimental Evidence of Turbulence in the Boundary Layer in High Rayleigh Number Convection in Air. *to appear in Phys. Rev.Lett.*.

Fedorovich, E., R. Conzemius, I. Esau, F. K. Chow, D. Lewellen, C.-H. Moeng, D. Pino, P. Sullivan and J. V.-G. de Arellano (2004a). Entrainment into sheared convective boundary layers as predicted by different large eddy simulation codes. *Preprints, 16th Symp. on Boundary Layers and Turbulence, Portland, ME, USA, Amer. Meteorol. Soc.*, p. P4.7.

Fedorovich, E., R. Conzemius and D. Mironov (2004b). Convective entrainment into a shear-free linearly stratified atmosphere: bulk models reevaluated through large-eddy simulation. *J. Atmos. Sci.*, **61**, 281–295.

Fedorovich, E. E. and D. V. Mironov (1995). A Model for a Shear-Free Convective Boundary Layer with Parameterized Capping Inversion Structure. *J. Atmos. Sci.*, **52**(1), 83–96.

Fernando, H. J. S. (1991). Turbulent mixing in stratified fluids. *Annu. Rev. Fluid Mech.*, **23**, 455–493.

Fernando, H. J. S. and L. J. Little (1990). Molecular-diffusive effects in penetrative convection. *Phys. Fluids A*, **2**, 1592–1596.

Fox, D. and J. Deardorff (1972). Computer methods for simulation of multidimensional, nonlinear, subsonic, incompressible flow. *Journal of Heat Transfer*, **94**(4), 337–&.

Garratt, J. R. (1992). The Atmospheric Boundary Layer. Cambridge University Press.

Grabon, J. S., K. J. Davis, C. Kiemle and G. Ehret (2009). Airborne Lidar Observations of the Transition Zone Between the Convective Boundary Layer and Free Atmosphere During the International H2O Project (IHOP) in 2002. *Bound.-Layer Meteor.*, **134**(1), 61–83.

Grachev, A. A., C. W. Fairall and E. F. Bradley (2000). Convective profile constants revisited. *Bound.-Layer Meteor.*, **94**, 495–515.

Guillemet, B., H. Isaka and P. Mascart (1983). Molecular dissipation of turbulent fluctuations in the convective mixed layer part I: Height variations of dissipation rates. *Bound.-Layer Meteor.*, **27**(2).

Hatlee, S. C. and J. C. Wyngaard (2007). Improved Subfilter-Scale Models from the HATS Field Data. *J. Atmos. Sci.*, **64**(5), 1694–1705.

Hebert, D. A. and S. M. de Bruyn Kops (2006). Predicting turbulence in flows with strong stable stratification. *Phys. Fluids*, **18**(6), 066602.

Hogan, R. J., A. L. M. Grant, A. J. Illingworth, G. N. Pearson and E. J. O'Connor (2009). Vertical velocity variance and skewness in clear and cloud-topped boundary layers as revealed by Doppler lidar. *Q. J. Roy. Meteorol. Soc.*, **135**(640), 635–643.

Hopfinger, E. J. (1987). Turbulence in stratified fluids: A review. *J. Geophys. Res.*, **92**(C5), 5287.

Huang, H.-Y., B. Stevens and S. A. Margulis (2007). Application of Dynamic Subgrid-scale Models for Large-eddy Simulation of the Daytime Convective Boundary Layer over Heterogeneous Surfaces. *Bound.-Layer Meteor.*, **126**(3), 327–348.

Jimenez, J. (2013). Near-wall turbulence. *Phys. Fluids*, **25**(101302).

Jonker, H. J. J. and M. A. Jimnez (2014). Laboratory Experiments on Convective Entrainment Using a Saline Water Tank. *Bound.-Layer Meteor.*, **151**, 479–500.

Jonker, H. J. J., M. van Reeuwijk, P. Sullivan and N. Patton (2012). Interfacial layers in clear and cloudy atmospheric boundary layers. *Turbulence, Heat and Mass Transfer 7*, pp. 3–14.

Kaimal, J. C. and J. C. Wyngaard (1990). The Kansas and Minnesota experiments. *Bound.-Layer Meteor.*, **50**(1-4), 31–47.

Kaimal, J. C., J. C. Wyngaard, D. A. Haugen, O. R. Cot, Y. Izumi, S. J. Caughey and C. J. Readings (1976). Turbulence Structure in the Convective Boundary Layer. *J. Atmos. Sci.*, **33**(11), 2152–2169.

Kleissl, J., V. Kumar, C. Meneveau and M. B. Parlange (2006). Numerical study of dynamic Smagorinsky models in large-eddy simulation of the atmospheric boundary layer: Validation in stable and unstable conditions. *Water Resources Research*, **42**(6).

Kline, S. J. (1986). Similitude and approximation theory. Springer-Verlag, Berlin ; New York. ISBN 0387165185.

Kraichnan, R. H. (1962). Turbulent Thermal Convection at Arbitrary Prandtl Number. *Phys. Fluids*, **5**(11), 1374.

Lee, M., N. Malaya and R. D. Moser (2013). Petascale direct numerical simulation of turbulent channel flow on up to 786K cores. In *SC 2013 Proceedings of the International Conference on High Performance Computing, Networking, Storage and Analysis*, pp. 1–11. ACM Press.

Lenschow, D. H., M. Lothon, S. D. Mayor, P. P. Sullivan and G. Canut (2011). A Comparison of Higher-Order Vertical Velocity Moments in the Convective Boundary Layer from Lidar with In Situ Measurements and Large-Eddy Simulation. *Bound.-Layer Meteor.*, **143**(1), 107–123.

Lenschow, D. H., J. C. Wyngaard and W. T. Pennell (1980). Mean-Field and Second-Moment Budgets in a Baroclinic, Convective Boundary Layer. *J. Atmos. Sci.*, **37**(6), 1313–1326.

Lilly, D. K. (1968). Models of cloud-topped mixed layers under a strong inversion. *Q. J. Roy. Meteorol. Soc.*, **94**(401), 292–309.

Linden, P. (1973). The interaction of a vortex ring with a sharp density interface: a model for turbulent entrainment. *Journal of Fluid Mechanics*, **60**(03), 467480.

Linden, P. F. (1975). The deepening of a mixed layer in a stratified fluid. *J. Fluid Mech.*, **71**(02), 385–405.

Mahrt, L. (1979). Penetrative convection at the top of a growing boundary layer. *Q. J. Roy. Meteorol. Soc.*, **105**(444), 469–485.

Malkus, W. V. R. (1954). The Heat Transport and Spectrum of Thermal Turbulence. *Proceedings of the Royal Society A: Mathematical, Physical and Engineering Sciences*, **225**(1161), 196–212.

Mason, P. J. (1994). Large-eddy simulation: A critical review of the technique. *Quarterly Journal of the Royal Meteorological Society*, **120**(515), 1–26.

McNaughton, K. (2004). Turbulence Structure of the Unstable Atmospheric Surface Layer and Transition to the Outer Layer. *Bound.-Layer Meteor.*, **112**(2), 199–221.

Mellado, J. P. (2012). Direct numerical simulation of free convection over a heated plate. *J. Fluid Mech.*, **712**, 418–450.

Mellado, J. P. and C. Ansorge (2012). Factorization of the Fourier transform of the pressure-Poisson equation using finite differences in colocated grids. *Z. Angew. Math. Mech.*, **92**, 380–392.

Miller, M. J., A. C. M. Beljaars and T. N. Palmer (1992). The Sensitivity of the ECMWF Model to the Parameterization of Evaporation from the Tropical Oceans. *J. Climate*, **5**(5), 418–434.

Moeng, C.-H. and R. Rotunno (1990). Vertical velocity skewness in the buoyancy-driven boundary layer. *J. Atmos. Sci.*, **47**, 1149–1162.

Moeng, C.-H. and P. P. Sullivan (1994). A Comparison of Shear- and Buoyancy-Driven Planetary Boundary Layer Flows. *J. Atmos. Sci.*, **51**(7), 999–1022.

Moin, P. and K. Mahesh (1998). Direct numerical simulation: A tool in turbulence research. *Annu. Rev. Fluid Mech.*, **30**, 539–578.

Monin, A. S. and A. M. Yaglom (2007). Statistical Fluid Mechanics. Mechanics of Turbulence. Dover Publications.

Nieuwstadt, F. T. M. and H. v. Dop (eds.) (1984). Atmospheric turbulence and air pollution modelling: a course held in The Hague, 21-25 September, 1981. D. Reidel.

Obukhov, A. (1946). Turbulence in an atmosphere with a non- uniform temperature. *Tr. Inst. Teor. Geofiz. Akad. Nauk. SSSR*, **1**, 95–115.

Orlanski, I. (1975). Rational subdivision of scales for atmospheric processes. *B. Am. Meteorol. Soc.*, **56**(5), 527–530.

Ozmidov, R. V. (1965). On the turbulent exchange in a stably stratified ocean. *Izv., Atmospheric and Oceanic Physics Series*, **1**(8), 853–860.

Panofsky, H. A., H. Tennekes, D. H. Lenschow and J. C. Wyngaard (1977). The characteristics of turbulent velocity components in the surface layer under convective conditions. *Bound.-Layer Meteor.*, **11**, 355–361.

Perera, M., H. Fernando and D. Boyer (1994). Turbulent mixing at an inversion layer. *J. Fluid Mech.*, **267**, 275298.

Pino, D., J. De Arellano and P. Duynkerke (2003). The contribution of shear to the evolution of a convective boundary layer. *J. Atmos. Sci.*, **60**(16), 1913–1926.

Pino, D. and J. Vil-Guerau De Arellano (2008). Effects of shear in the convective boundary layer: analysis of the turbulent kinetic energy budget. *Acta Geophysica*, **56**(1), 167–193.

Pope, S. B. (2000). Turbulent Flows. Cambridge University Press.

Prandtl, L. (1932). Meteorologische Anwendung der Strömungslehre. *Beitr. Phys. Atmos.*, **19**, 188–202.

Priestley, C. H. B. (1954). Convection from a large horizontal surface. *Austr. J. Phys.*, **7**, 176–201.

Rogallo, R. S. and P. Moin (1984). Numerical Simulation of Turbulent Flows. *Annual Review of Fluid Mechanics*, **16**(1), 99–137.

Rouse, H. and J. Dodu (1955). Diffusion turbulence á traverse une discontinuitè. *Houille Blanche*, **10**, 405.

Schmidt, H. and U. Schumann (1989). Coherent structure of the convective boundary layer derived from large-eddy simulations. *J. Fluid Mech.*, **200**, 511–562.

Schumann, U. (1988). Minimum friction velocity and heat transfer in the rough surface layer of a convective boundary layer. *Bound.-Layer Meteor.*, **44**(4), 311–326.

Smyth, W. D. and J. N. Moum (2000). Length scales of turbulence in stably stratified mixing layers. *Phys. Fluids*, **12**(6), 1327–1342.

Soares, P., P. Miranda, A. Siebesma and J. Teixeira (2004). An eddy-diffusivity/mass-flux parametrization for dry and shallow cumulus convection. *Q. J. Roy. Meteorol. Soc.*, **130**(604), 3365–3383.

Sorbjan, Z. (1996). Comments on "A convective transport theory for surface fluxes". *J. Atmos. Sci.*, **54**, 576–578.

Sorbjan, Z. (1999). Similarity of scalar fields in the convective boundary layer. *J. Atmos. Sci.*, **56**(13), 2212–2221.

Sorbjan, Z. (2007). A numerical study of daily transitions in the convective boundary layer. *Bound.-Layer Meteor.*, **123**(3), 365–383.

Spalart, P. R., R. D. Moser and M. M. Rogers (1991). Spectral methods for the Navier-Stokes equations with one infinite and two periodic directions. *J. Comput. Phys.*, **96**, 297–324.

Stevens, B. (2002). Entrainment in stratocumulus-topped mixed layers. *Q. J. Roy. Meteorol. Soc.*, **128**, 2663–2690.

Stevens, B. and D. H. Lenschow (2001). Observations, Experiments, and Large Eddy Simulation. *B. Am. Meteorol. Soc.*, **82**(2), 283–294.

Stevens, B., C.-H. Moeng, A. S. Ackerman, C. S. Bretherton, A. Chlond, S. de Roode, J. Edwards, J.-C. Golaz, H. Jiang, M. Khairoutdinov, M. P. Kirkpatrick, D. C. Lewellen, A. Lock, F. Müller, D. E. Stevens, E. Whelan and P. Zhu (2005). Evaluation of large-eddy simulations via observations of nocturnal marine stratocumulus. *Mon. Wea. Rev.*, **133**, 1443–1462.

Stevens, B., C.-H. Moeng and P. P. Sullivan (1999). Large-Eddy Simulations of Radiatively Driven Convection: Sensitivities to the Representation of Small Scales. *J. Atmos. Sci.*, **56**(23), 3963–3984.

Stevens, B., C.-H. Moeng and P. P. Sullivan (2000a). Entrainment and subgrid lengthscales in large-eddy simulations of atmospheric boundary layer flows. *Developments in Geophysical Turbulence: Selected Contributions to the IUTAM meeting*.

Stevens, D. E., J. B. Bell, A. S. Almgren, V. E. Beckner and C. A. Rendleman (2000b). Small-scale processes and entrainment in a stratocumulus marine boundary layer. *J. Atmos. Sci.*, **57**, 567–581.

Stull, R. B. (1988). An Introduction to Boundary Layer Meteorology. Kluwer Academic Publishers.

Sullivan, P. P., C.-H. Moeng, B. Stevens, D. H. Lenschow and S. D. Mayor (1998). Structure of the entrainment zone capping the convective atmospheric boundary layer. *J. Atmos. Sci.*, **55**, 3042–3064.

Sullivan, P. P. and E. G. Patton (2011). The effect of mesh resolution on convective boundary layer statistics and structures generated by large-eddy simulations. *J. Atmos. Sci.*, **68**, 2395–2415.

Sykes, R. I., D. S. Henn and W. S. Lewellen (1993). Surface-layer description under free-convection conditions. *Q. J. Roy. Meteorol. Soc.*, **119**(511), 409–421.

Teixeira, J. and S. Cheinet (2004). A Simple Mixing Length Formulation for the Eddy-Diffusivity Parameterization of Dry Convection. *Bound.-Layer Meteor.*, **110**(3), 435–453.

Tennekes, H. (1975). Reply. *J. Atmos. Sci.*, **32**(5), 992–995.

Tennekes, H. and A. G. M. Driedonks (1981). Basic entrainment equations for the atmospheric boundary layer. *Bound.-Layer Meteor.*, **20**, 515–531.

Tennekes, H. and J. L. Lumley (1972). A First Course in Turbulence. MIT Press.

Townsend, A. A. (1959). Temperature fluctuations over a heated horizontal surface. *J. Fluid Mech.*, **5**, 209–241.

Townsend, A. A. (1964). Natural convection in water over an ice surface. *Q. J. Roy. Meteorol. Soc.*, **90**(385), 248–259.

Träumner, K., C. Kottmeier, U. Corsmeier and A. Wieser (2011). Convective Boundary-Layer Entrainment: Short Review and Progress using Doppler Lidar. *Bound.-Layer Meteor.*, **141**(3), 369–391.

Tsinober, A. (2009). An Informal Conceptual Introduction to Turbulence. Springer, 2nd edition.

Tsinober, A. (2013). The essence of turbulence as a physical phenomenon with emphasis on issues of paradigmatic nature. Springer.

Turner, J. (1986). Turbulent entrainment: the development of the entrainment assumption, and its application to geophysical flows. *J. Fluid Mech*, **173**(431), 71.

Turner, J. S. (1973). Buoyancy Effects in Fluids. Cambridge University Press.

van Reeuwijk, M., H. J. J. Jonker and K. Hanjalic (2008). Wind and boundary layers in Rayleigh-Bnard convection. II. Boundary layer character and scaling. *Physical Review E*, **77**(3).

Willis, G. E. and J. W. Deardorff (1974). A laboratory model of the unstable planetary boundary layer. *J. Atmos. Sci.*, **31**, 1297–1307.

Wilson, D. K. (2001). An alternative function for the wind and temperature gradients in unstable surface layers. *Bound.-Layer Meteor.*, **99**(1), 151158.

Winters, K. B., P. N. Lombard, J. J. Riley and E. A. D'Asaro (1995). Available potential energy and mixing in density-stratified fluids. *J. Fluid Mech.*, **289**(-1), 115.

Witek, M. L., J. Teixeira and G. Matheou (2011a). An Eddy Diffusivity-Mass Flux Approach to the Vertical Transport of Turbulent Kinetic Energy in Convective Boundary Layers. *J. Atmos. Sci.*, **68**(10), 2385–2394.

Witek, M. L., J. Teixeira and G. Matheou (2011b). An Integrated TKE-Based Eddy Diffusivity/Mass Flux Boundary Layer Closure for the Dry Convective Boundary Layer. *J. Atmos. Sci.*, **68**(7), 1526–1540.

Wood, R. (2012). Stratocumulus Clouds. *Mon. Wea. Rev.*, **140**, 2373–2423.

Wulfmeyer, V., S. Pal, D. D. Turner and E. Wagner (2010). Can Water Vapour Raman Lidar Resolve Profiles of Turbulent Variables in the Convective Boundary Layer? *Bound.-Layer Meteor.*, **136**(2), 253–284.

Wyngaard, J. C. (2004). Toward Numerical Modeling in the Terra Incognita. *J. Atmos. Sci.*, **61**(14), 1816–1826.

Wyngaard, J. C., O. R. Coté and Y. Izumi (1971). Local free convection, similarity, and the budget of shear stress and heat flux. *J. Atmos. Sci.*, **28**, 1171–1182.

Xuequan, E. and E. Hopfinger (1986). On mixing across an interface in stably stratified fluid. *J. Fluid Mech.*, **166**, 227244.

Zeman, O. and H. Tennekes (1977). Parameterization of the Turbulent Energy Budget at the Top of the Daytime Atmospheric Boundary Layer. *J. Atmos. Sci.*, **34**(1), 111–123.

Zhao, Z., Z. Gao, D. Li, X. Bi, C. Liu and F. Liao (2013). Scalar Flux-Gradient Relationships Under Unstable Conditions over Water in Coastal Regions. *Bound.-Layer Meteor.*, **148**(3), 495–516.

Zilitinkevich, S. S. (1991). Turbulent Penetrative Convection. Avebury Technical.

Zilitinkevich, S. S., J. C. R. Hunt, I. N. Esau, A. A. Grachev, D. P. Lalas, E. Akylas, M. Tombrou, C. W. Fairall, H. J. S. Fernando, A. A. Baklanov and S. M. Joffre (2006). The influence of large convective eddies on the surface-layer turbulence. *Q. J. Roy. Meteorol. Soc.*, **132**(618), 1423–1456.

A The minimum convective boundary layer thickness

The length scale $L_0 = (B_0/N^3)^{1/2}$ can also be related to the minimum CBL thickness at which stratification affects the evolution and the morphology of the turbulent boundary layer, and at which the system changes regimes. We can identify three different regimes. First, there is an early regime in which the turbulent boundary layer is shallow enough to behave essentially as if it were developing in neutral conditions: the boundary layer height varies proportionally to $(B_0 t^3)^{1/2}$ and the kinetic energy profiles behave self-similarly when normalized by the convection scales (Mellado, 2012). Second, there is an intermediate regime in which N^2 becomes relevant, turbulence kinetic energy is increasingly transferred from the vertical to the horizontal direction, and the growth rate diminishes with respect to that of the early regime. Eventually, the equilibrium (quasi-steady) entrainment regime is achieved, in which the CBL thickness varies proportionally to $(B_0 t/N^2)^{1/2}$ and the kinetic energy profiles become again self-similar when normalized with the convection scales (see Chapter 3 sections 3.3 and 3.5). The physical interpretation of L_0 within this context of regime transition is explained as follows.

For the neutral case $N^2 = 0$, the mean buoyancy profile tends towards $\alpha_1 b_s$ as the distance to the surface increases (Fig. A.1), a constant fraction of the surface buoyancy $b_s = \alpha_2 (B_0^2/z_0)^{1/3}$, where z_0 indicates either the roughness length or the diffusion length, depending on the surface properties. The height at which this buoyancy level $\alpha_1 b_s$ becomes comparable with that of the background reference profile $b_{\mathrm{bg}} = N^2 z$ yields the crossover height $\alpha_1 b_s/N^2 = \alpha_1 \alpha_2 N^{-2} (B_0^2/z_0)^{1/3}$. When the depth of the turbulent boundary layer is much smaller than this crossover height, the turbulent boundary layer is not affected by the stratification above. Hence, this crossover height can be considered as the minimum CBL thickness introduced in the previous paragraph, and it can be expressed explicitly in terms of L_0 as $[\alpha_1 \alpha_2 (L_0/z_0)^{1/3}] L_0$.

For a smooth surface and in the case of $\mathrm{Pr} = \nu/\kappa = 1$, as considered in this work, the diffusion length is $z_0 = (\kappa^3/B_0)^{1/4}$ and thus $L_0/z_0 = \mathrm{Re}_0^{3/4}$, where $\mathrm{Re}_0 = B_0/(\nu N^2)$. Moreover, $\alpha_1 \simeq 0.1$ and $\alpha_2 \simeq 4$ (Mellado, 2012). Hence, in terms of the controlling parameters of the problem, the minimum CBL thickness is $\simeq 0.4 L_0 \mathrm{Re}_0^{1/4}$,

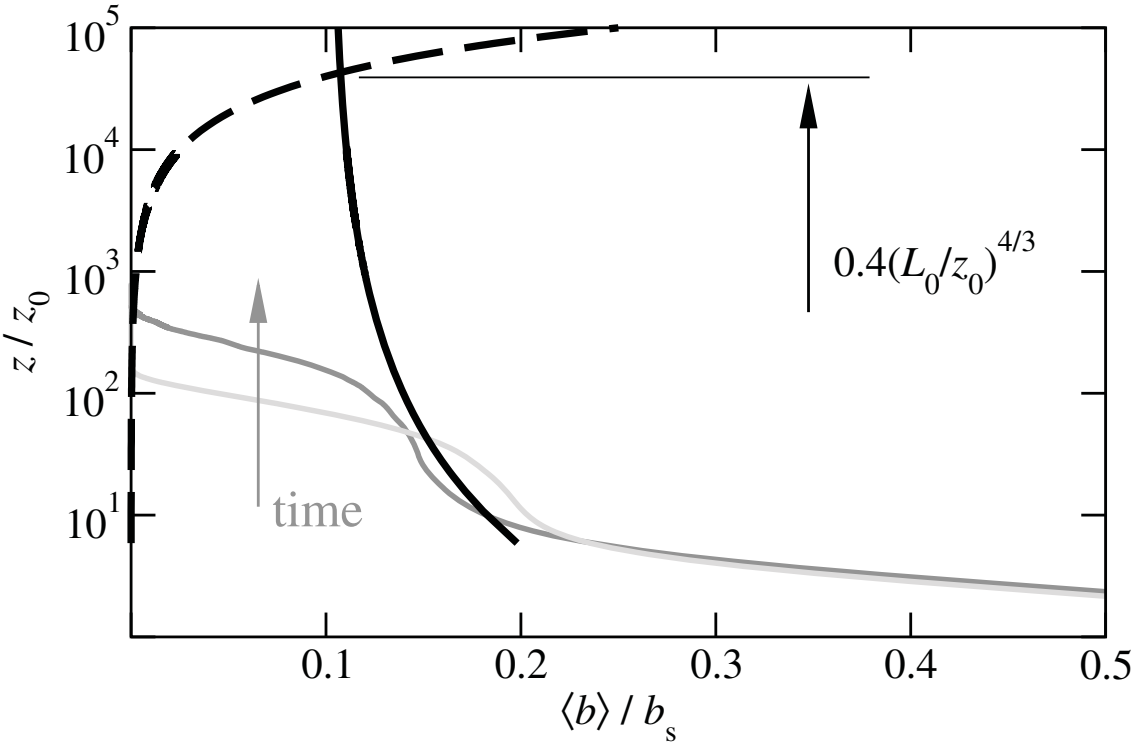

Figure A.1: Sketch illustrating the crossover height $[0.4(L_0/z_0)^{1/3}]L_0 = [0.4(L_0/z_0)^{4/3}]z_0$ at which the background buoyancy profile $b_{\rm bg} = N^2 z$ (dashed line) is felt by the growing boundary layer (solid lines). The solid black line is $\langle b \rangle / b_s \simeq 0.10 + 0.17(z/z_0)^{-1/3}$, as obtained from DNS of a neutral CBL (Mellado, 2012, gray profiles). b_s is the surface mean buoyancy. The background stratification shown in this figure corresponds to the case of a smooth wall, $\nu/\kappa = 1$ and $\mathrm{Re}_0 = 10^5$, z_0 being then equal to the diffusion length $(\kappa^3/B_0)^{1/4}$.

i.e., basically proportional to L_0 because of the weak dependence, $\mathrm{Re}_0^{1/4}$, on the Reynolds number.

B Grid resolution study

We have quantified the dependence of the statistics on the grid resolution by comparing simulations Re040.R1 and Re040.R2 (see Table B.1). The grid spacing in case Re040.R2 is half the size of the grid spacing in case Re040.R1, and the corresponding initial conditions have been obtained by interpolating the initial fields from case Re040.R1 into the grid from case Re040.R2. The rest of the parameters in both simulations are exactly the same. We have measured the resolution in Kolmogorov units, $\Delta z/\eta$, as it is customary in DNS (Moin and Mahesh, 1998; Pope, 2000).

For the resolution $(\Delta z/\eta)_{\max} \simeq 1$ considered in this work, the average difference in the relevant statistics between cases Re040.R1 and Re040.R2, both in the near-wall region and in the entrainment zone, remains less than 3% (Fig. B.1), which is comparable to the statistical convergence that we achieve with the domain size considered in this work. This result, along with the scalings of the diffusive layer next to the wall and the Kolmogorov scale in terms of the kinematic viscosity ν and surface buoyancy flux B_0, allows us to estimate, for a given grid size, the maximum reference Reynolds number Re_0 that still guarantees a good enough resolution of the small scales, when using the numerical scheme described in Chapter 2 section 2.3.3. Further discussion can be found in Mellado (2012).

Simulation	Re_0	Grid	$(\Delta z/\eta)_{\max}$
Re040.R1	42	$1280 \times 1280 \times 576$	0.82
Re040.R2	42	$2560 \times 2560 \times 1152$	0.41

Table B.1: Simulations used in the study of the sensitivity of the results to the finite domain size and the grid resolution. Case Re040.R1 is equal to Case Re040 in Table 2.1 but with half the horizontal extension, i.e., $107L_0 \times 107L_0 \times 56.6L_0$. Case Re040.R2 is equal to Case040.R1 but with twice the grid resolution (half the grid spacing in each of the three directions). The last column provides the resolution (in Kolmogorov units) at $z_{\mathrm{enc}}/L_0 \simeq 13$.

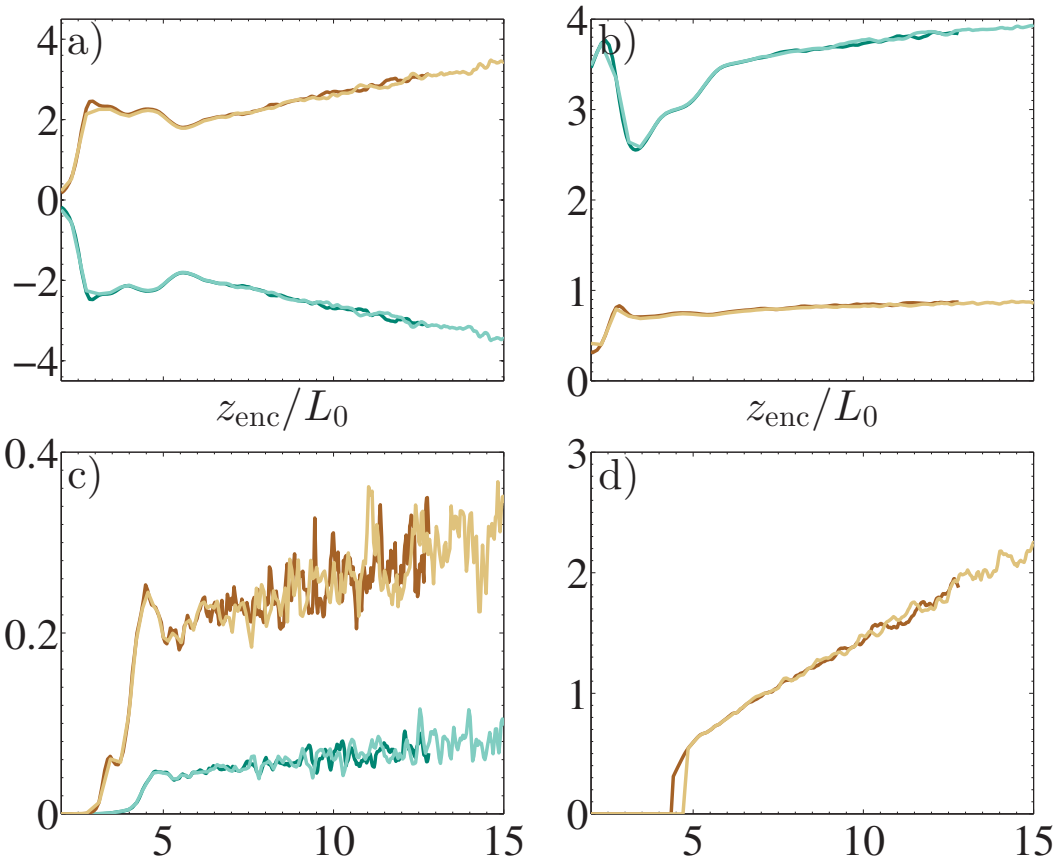

Figure B.1: Comparison between simulation Re040.R1 (light colors) and simulation Re040.R2 with double the spatial resolution (dark colors) used in the grid resolution study (Table B.1). Statistics at the wall are as follow: a) normalized TKE budget: dissipation term $-\varepsilon_{wall}/B_0$ (blue); transport term $(-\partial T/\partial z)_{wall}/B_0$ (brown) b) normalized mean buoyancy difference $(\langle b\rangle_{wall} - b_{enc})/(B_0^3/\kappa)^{1/4}$ (blue); normalized r.m.s. of the buoyancy fluctuation $b_{rms}/(B_0^3/\kappa)^{1/4}$ (brown), where $(B_0^3/\kappa)^{1/4}$ is the diffusion buoyancy scale (see Chapter 4 and Mellado, 2012). Within the entrainment zone are as follow: c) maximum of transport term $\max(-\partial T/\partial z)/B_0$ (brown); turbulent contribution to the entrainment ratio A_t (blue) d) maximum of the normalized r.m.s. of the buoyancy fluctuation b_{rms}/b_*.

I am forever grateful to the following:

Almighty Father, to God be the glory and honor for He helps me without fail and is the reason why I got to where I am now. Thank You for answering my daily devotional prayer and giving me not only a good PhD position but also a great mentor.

Juan Pedro Mellado, for believing in me when I even do not believe in myself and for being a great mentor in science and in life.

I acknowledge the scientific support of the following:

Bjorn Stevens, my second thesis adviser, for sharing his insights and knowledge on the problem and for giving feedback plus encouragement.
Alberto de Lozar, for being the person next to Juan Pedro that I was at ease to discuss with scientifically.
Evgeni Fedorovich, the big man with a big heart, thanks for the patience and all the helpful criticism that has made our entrainment zone paper much better.
Chiel van Heerwaarden, for his readiness to help, and willingness to share his knowledge.
Ritthik Bhattacharya, for the discussions on the dry CBL and on boundary layer schemes.
The rest of the Turbulent Mixing Processes (TMP) group: Dick Abma, Thomas Keitzl, Cedrick Ansorge, Lukas, and Malte – for all the group meetings together, especially for the feedback and patience during practice talks. Also, thanks guys for usually letting me choose where to go for lunch on Fridays.

I thank the following for the (moral) support they have given:
To my family: Nanay, Dad, Kuya Jay, Janvic and my cousin Ate Star – I dedicate this work to them.
Peter P., for being an integral part of my PhD life here in Hamburg.
Sister Gina Elizaga and her family, and the Iglesia ni Cristo (Church of Christ) Locale of Hamburg for being my family and my community in Hamburg. I also dedicate this work to Sis. Gina's daughter, my little sister Elisha. I hope that I could inspire her to strive for higher education and realize the great potential of women.
Cheska Siongco, for enduring my craziness, for all the funny times and meals together.
My high school best friend, Joanne Nepomuceno, for still being a listening ear.
Andriy Styahar, for the support and friendship.
Armelle Remedio, Seethala Chellappan, Dagmar Popke, Ania Jaruga, Yvonne Kuestermann – for some of the lovely times spent together in the institute.
Antje Weitz, Connie Kampmann, and the IMPRS office for being the backbone of the school.
Prof. Jens Struckmeier, for helping me transition into this PhD position. Also the Erasmus Mundus MathMods programme, if not for this programme, I might not be in Hamburg today.
Angela Gruber, for being so loving and helpful to the entire atmosphere department.
My former roommates in Z405: Matthias Bittner, Pierre Mohr-Durdez, Christina Klasa – thanks for making room 405 pleasant and conducive for work.
The entire Max Planck Institute for Meteorology, for sheltering me for almost four years, special mention to the microwave and fridge of the 4th floor kitchen.
The people whom I have met during my travels abroad that have made my PhD years more colorful, and the German tax payers that funded this scientific work.

Eidesstattliche Versicherung

Declaration on oath

Hiermit erkläre ich an Eides statt, dass ich die vorliegende Dissertationsschrift selbst verfasst und keine anderen als die angegebenen Quellen und Hilfsmittel benutzt habe.

I hereby declare, on oath, that I have written the present dissertation by my own and have not used other than the acknowledged resources and aids.

Hamburg, den

Hinweis / Reference

Die gesamten Veröffentlichungen in der Publikationsreihe des MPI-M
„Berichte zur Erdsystemforschung / Reports on Earth System Science“,
ISSN 1614-1199

sind über die Internetseiten des Max-Planck-Instituts für Meteorologie erhältlich:
http://www.mpimet.mpg.de/wissenschaft/publikationen.html

All the publications in the series of the MPI -M
„Berichte zur Erdsystemforschung / Reports on Earth System Science“,
ISSN 1614-1199

are available on the website of the Max Planck Institute for Meteorology:
http://www.mpimet.mpg.de/wissenschaft/publikationen.html